SkyDowser

An Electromagnetic Geophysical Survey Instrument for Groundwater Detection

Kiren Newadj

Master of Science Thesis

TU Delft Delft University of Technology

Delft Center for Systems and Control

SkyDowser

An Electromagnetic Geophysical Survey Instrument for Groundwater Detection

Master of Science Thesis

For the degree of Master of Science in Microelectronics at Delft University of Technology

Kiren Newadj

January 30, 2019

Faculty of Electrical Engineering, Mathematics and Computer Science · Delft University of Technology

Copyright © Electrical Engineering
All rights reserved.

Delft University of Technology
Department of
Electrical Engineering

The undersigned hereby certify that they have read and recommend to the Faculty of Electrical Engineering, Mathematics and Computer Science for acceptance a thesis entitled

SkyDowser

by

Kiren Newadj

in partial fulfillment of the requirements for the degree of

Master of Science in Microelectronics

Dated: January 30, 2019

Supervisor(s):

Dr.ir. Andre Bossche, TU Delft Supervisor

ing. Jeroen Bastemeijer, TU Delft Supervisor

ir. Erik van der Putte, SkyDowser Supervisor

Reader(s):

Prof. dr. ir.Evert Slob

Dr.ir. Arjan van Genderen

Abstract

Clean drinking water is still not widely available around the globe and therefore remains an unsolved issue. In fact, 1 in 9 people lack daily access to safe water and sanitation. Groundwater is a water supply source that needs minor treatment and thereby presents itself as a good solution to this global issue. Especially in development countries for example in East Africa this would be a viable solution. One interesting exploration method to detect groundwater in an area is airborne Frequency Domain Electromagnetic (FDEM) survey. However, most airborne EM survey instruments are expensive and bulky. Even though that this exploration technique has been around since the 50s, a commercial inexpensive airborne FDEM instrument has still not penetrated the market.
This thesis describes the investigation of a novel portable FDEM survey instrument that will be employed by an Unmanned Aerial Vehicle (UAV). The system architecture for the measurement instrument is presented and the functionality, design considerations and requirements of each system block is given. To check the feasibility of the proposed architecture, a handheld Proof-of-Concept is implemented, which can carry out measurements between 100 - 12.000 Hz. The experimental measurement results of the Proof-of-Concept at operating frequencies of 925, 2175, 5025 Hz are presented and compared against measurements of GEM-2A instrument, which is employed as a reference.

Table of Contents

List of Figures

List of Tables

Acknowledgements

This thesis is the closing chapter of my Electrical Engineering study at the Delft University of Technology. It has been a remarkable, but also extremely difficult road. There had been moments where I doubted myself a lot and questioned whether I would be able to make it towards the "finishing line" and even start working on a thesis. Through perseverance and the support of many people I was able to overcome and work on this interesting project. I would therefore like to take this opportunity to thank the people who helped me during this time, in work and life.

First of all, I would like to express my gratitude towards my supervisors Dr. ir. Andre Bossche and ing. Jeroen Bastemeijer for their expert guidance, continuous support and encouragement during this project from the very beginning, till the very end. Their experience, knowledge and insight into all aspects of this project have helped me immensely. Our discussions at the university, over a nice cup of coffee, always gave me new insights and helped me to approach this project from different angles. Moreover, I would like to thank Jeroen for building the Proof-of-Concept measurement instrument and all his practical advice about circuits, measurements and engineering in general.

I would like to thank the founders of SkyDowser (nowadays Watermappers), ir. Erik van der Putte and ir. Sjoerd Dijkstra for providing me the opportunity to work on this project. Erik and Sjoerd provided the information about how the measurement instrument will be employed and how to set up the right requirements for this project. In particular, I would also like to thank Erik for sharing his knowledge about electromagnetic survey systems and groundwater, which was a great help to kick-off this project.

Next, I would like to thank my whole family for their caring support. They have been the driving force behind me and supported me in every way they could. My father made me realize what a great opportunity it is to study at a prestigious university like the TU Delft, I am really grateful for that. Another big pillar of support in my life is my girlfriend Rose. Thanks for being with me and for your loving support through everything in life.

Further, I would like to thank all my friends and training partners at Brazilian Jiu Jitsu Academy Amsterdam. After a long day of working, the training at the end of the day was a great way to feel energized again and to clear my mind in order to get ready for the next day.

Lastly, I would like to dedicate this work to my idiosyncratic cat Isabel (2008 - 2018), who passed away unexpectedly and way too early. She was the greatest company during my working hours from home and made sure that I had some entertaining breaks.

Delft, University of Technology — Kiren Newadj
January 30, 2019

Chapter 1

Introduction

Clean drinking water is one of the primary human needs and a basic requirement for economic development. A lack of water to meet daily needs is a reality for 1 in 9 people around the world. Not only is this currently a significant problem, but also globally it is getting worse as cities and populations grow, leading to an ever increasing demand for fresh water. The safest kind of water supply is the use of ground water. Since groundwater has a natural protection against pollution by the covering layers, it requires only minor water treatment [1]. There are several geophysical methods of exploration in the search for hydrogeological data. In this thesis, the focus will be on the controlled source electromagnetic method to obtain information about the soil.

1-1 Electromagnetic Exploration

Electromagnetic (EM) exploration is a commonly used survey method to obtain information about the subsurface, specifically electrical ground conductivity. The basic principle behind controlled source EM exploration is a current-source driving a transmitter coil, which will generate an Eddy current in the subsurface. The current-voltage relationship will provide information about the electrical conductivity of the subsurface. Depending on its mode of operation, EM exploration can be subdivided into Frequency Domain Electromagnetic (FDEM) and Time Domain Electromagnetic (TDEM). The development of the EM exploration method started in the 1920s in Scandinavia, Canada and the United States. Until the 1960s, practically all EM survey systems operated in the frequency domain. It was in 1962 when the first successful application of TDEM appeared. Since the 1950's the technique of Airborne Electromagnetic (AEM) started to develop and has been applied successfully for geophysical exploration [4]. A great advantage of AEM is that it can cover a large survey area in a short period of time. Commercially available EM and AEM systems are time consuming, bulky and expensive. With existing AEM systems there is also the need of a pilot and an aircraft, which will increase the operation costs significantly. A conventional EM instrument that is inexpensive, portable and airborne is not available on the market. To meet this gap in the market,

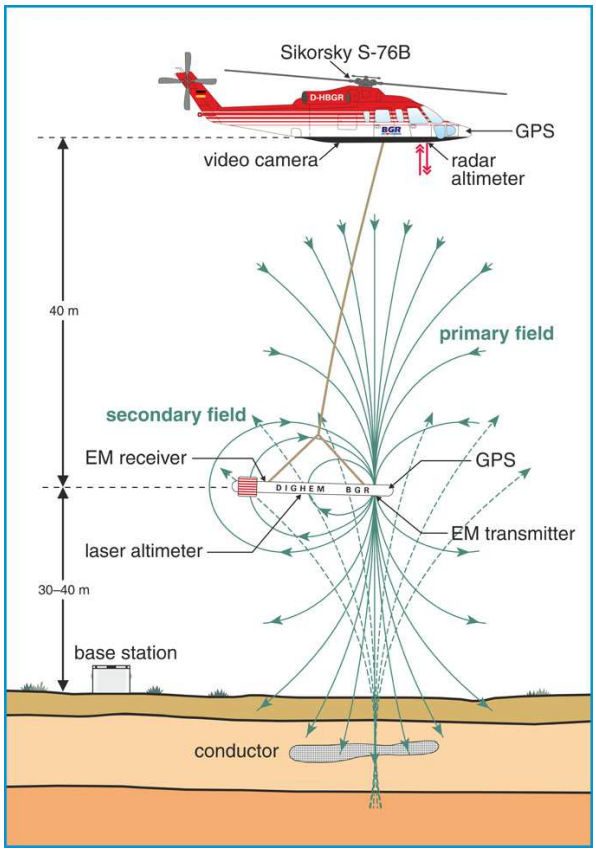

Figure 1-1: Helicopter geophysical EM survey system from BGR in operation [1]

the start-up company SkyDowser wants to develop an Unmanned Aerial Vehicle (UAV) that is equipped with a FDEM system.

1-2 Motivation

As stated in the previous section, the existing AEM systems require an aircraft to perform a geophysical survey. This is often a helicopter or fixed-wing system. The majority of airborne FDEM surveys is done by a helicopter, which use a towed rigid-boom that carries the set of sensor coils and the electronic circuit to process the signals. A rigid-boom can have a length of 6 meter long and the weight can vary between 120-240 kg. Fixed-wing systems typically have the sensor coils mounted directly at the wingtips, instead of in a rigid-boom. A typical flight altitude for these systems is around 80-350 meter. Figure 1-1 shows a sketch of the helicopter EM system from the German company BGR during operation.

SkyDowser wants to operate in countries and areas that are facing severe droughts. One targeted area of interest are development countries in East Africa, where the availability of trained pilots and aircrafts is limited and rather expensive. Therefore, their goal is to introduce a new airborne geophysical EM survey system on the market. To reduce the operation costs extensively, a portable UAV will be used. This will leave out the need for a pilot and

Table 1-1: Core specifications by SkyDowser

Flight altitude	30 m
Wing span	4 m
Maximum UAV payload	<10 kg
Maximum flight speed	30 m/s
Frequency range	30-100.000 Hz

expensive aircraft, while also improving the ease to perform the survey and reducing the set-up time drastically.

Before launching a final product, it is common to develop a prototype. In this thesis, the focus is on the Proof-of-Concept for the new prototype. Analog front-end circuits are needed to interface the sensor coils of the EM system. An attempt for of a proof-of-concept was made in the work of R.J. Tharian [5]. His work interfaces the receiver coils with a differential amplifier and the transmitter coil is driven by a K4003 Velleman amplifier. Furthermore, that work lacked an analog-to-digital conversion circuit and processing of the measured signals. This thesis presents an improved Proof-of-Concept that applies a different coil configuration, analog circuit design and interfaces with a Raspberry Pi 3 Model B single-board computer to process and store the measured signals as data.

1-3 Thesis Objective

The purpose of this thesis is to research the electromagnetic survey method for groundwater exploration and verify the results with a Proof-of-Concept. The core specifications for the final product as listed in Table 1-1 have been taken into account. These specifications put certain constraints on this research. It has been given that the UAV will fly at a fixed altitude of 30 meter with a maximum speed of 30 m/s. This will affect the penetration depth of the survey and determines the range of operating frequencies. The wing span of the UAV determines the maximum intercoil spacing, which in turn affects the depth of exploration. The FDEM survey method operates in the range of very-low to low-frequencies, thus the range of the Proof-of-Concept can be between 30-100.000 Hz. The UAV that SkyDowser will utilize has a maximum payload of 10 kg, thus the weight of the coils and on-board electronics cannot exceed this payload. The objectives of this thesis are the following:

1. **Electromagnetic survey research** Conduct a literature study of electromagnetic survey in the frequency domain for geophysical explorations.

2. **Coil configuration** The previous coil configuration has been redesigned. This part ensures the EM-signals that will be transmitted and received by the prototype.

3. **Analog circuit design** The transmitted and received EM-signals from the coils need to be amplified and filtered to be digitally processed. Thus, the design of the electronic system will inhere a new circuit level schematic to interface the coils with the Single-board Computer.

4. **Digital and embedded system design** After filtering and amplifying the signals in the analog domain, the signals will be processed by a Single-board Computer. At this stage the signals will be filtered by a digital Lock-in Amplifier, to further reduce the noise components and store the measured signals on a SD-card.

1-4 Thesis Organization

The remainder of this thesis is organized as follows. Chapter 2 begins with a brief review of electromagnetic theory that is needed to understand the physics behind EM survey. The topics that are covered in this chapter are: Basic fundamentals to describe an EM field, Maxwell's equation and EM survey methods.
In Chapter 3, the system architecture for an embedded FDEM survey instrument is introduced. The important definitions and theory of each system block are given. From this review, the system requirements of each block, which comply with the core specifications are also determined.
Chapter 4 describes the implementation details for a Proof-of-Concept of the system architecture that was given in the previous chapter.
Chapter 5 presents the measurements with the implemented Proof-of-Concept. A similar measurement is carried out with a GEM-2A instrument and used as a comparison to evaluate the performance of the Proof-of-Concept.
In Chapter 6, a conclusion is drawn from this work and the contributions made in this thesis are summarized. Lastly, recommendations for future work are presented.
Additional material is included in the appendix, where Appendix A gives the Python code that was used by the Raspberry Pi 3B.

Chapter 2

Electromagnetic Background

To grasp a basic understanding of the physics of electromagnetic survey, the fundamentals of EM theory with Maxwell's equations will be discussed first. It is followed by a brief overview of EM survey methods in the time domain and frequency domain, with an emphasis on FDEM. The basic fundamentals section in this chapter is based on [6]. The diffusion of EM-fields (2-1-1) and EM survey methods (2-2) follows the work of [4],[7] and [8].

2-1 Basic Fundamentals

An electromagnetic field can be described by the following components:

$\vec{E}$ = Electric field intensity in [Vm^{-1}]

$\vec{B}$ = Magnetic field density in [T]

$\vec{H}$ = Magnetic field strength in [Am^{-1}]

$\vec{J}$ = Electric current density in [Am^{-2}]

$\vec{D}$ = Electric displacement field in [Cm^{-2}]

$\vec{P}$ = Polarization in [Cm^{-2}]

Q = Electric charge density in either [Cm^{-1}], [Cm^{-2}], [Cm^{-3}], depending on the unit length, surface area or volume, respectively.

Earth's properties can be described by the following three quantities:

σ = Electrical conductivity

μ = Magnetic permeability

ε = Dielectric permittivity

The electromagnetic constitutive relations are representative for the EM properties of matter. In their general form, they constitute three vectorial relations between the vectors $\vec{E}, \vec{H}, \vec{B}, \vec{J}$ and $\vec{D}$. The standard form expresses $\vec{J}, \vec{D}$ and $\vec{B}$ in terms of $\vec{E}$ and $\vec{H}$.

linearity When the values of $\vec{J}, \vec{D}$ and $\vec{B}$ are linearly related to the values of $\vec{E}$ and $\vec{H}$, a medium is denoted as *linear*. If this is not the case, the medium is considered to be *non-linear*.

orientation If at a point in space the constitutive operators are orientation invariant, the medium is denoted as isotropic. If this property does not hold, the medium is denoted as anisotropic.

shift If the constitutive operators are shift invariant in a domain in space, the medium is denoted as homogeneous. If the shift invariance does not apply in a domain in space, the medium is denoted as heterogeneous.

Typical geophysical applications consider Earth's materials to be linear, homogeneous and isotropic. In this work, the same assumption will be made to simplify the study. Further, it is assumed that the dielectric permitivitty and magnetic permeability are that of free space, so that $\mu = \mu_0 = 4\pi \times 10^{-7}[Hm^{-1}]$ and $\varepsilon = \varepsilon_0 = \frac{1}{\mu_0 c_0^2} = 8.8541878176 \times 10^{-12}[Fm^{-2}]$. Where c_0 is the electromagnetic wave speed in vacuum, which equals the speed of light value of $299792458[ms^{-1}]$ Taking these assumptions into account, the constitutive equations between the three quantities are:

$$\vec{J} = \sigma \vec{E} \tag{2-1}$$

$$\vec{B} = \mu \vec{H} \tag{2-2}$$

$$\vec{D} = \varepsilon \vec{E} \tag{2-3}$$

Maxwell's equations One of the most influential equations in science are the Maxwell equations. James Clerk Maxwell unified electricity, magnetism and light for the first time to form the classical theory of electromagnetism, in which he described the relationship between various electric fields, magnetic fields and medium parameters. In differential form, the four modern equations can be written as:

$$\nabla \times \vec{E} = -\frac{\partial \vec{B}}{\partial t} \tag{2-4}$$

$$\nabla \times \vec{H} = \left(\vec{J} + \varepsilon \frac{\partial \vec{E}}{\partial t}\right) \tag{2-5}$$

$$\nabla \cdot \vec{E} = \frac{\rho}{\varepsilon_0} \tag{2-6}$$

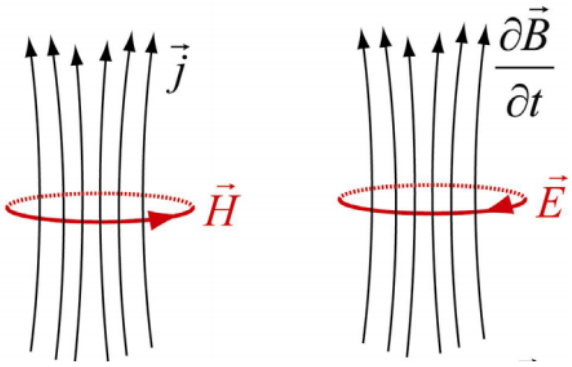

Figure 2-1: Ampere-Maxwell's law and Faraday's law [2]

$$\nabla \cdot \vec{B} = 0 \tag{2-7}$$

Equation (2-4) is known as Faraday's law, which states that a time-varying magnetic field produces a circulating electric field. The Ampere-Maxwell law describes that a spatially-varying magnetic field is produced by an electric current and a a time-varying electric field, which is given in (2-5). Figure 2-1 illustrates Faraday's law and the Ampere-Maxwell law. Equations (2-6) and (2-7) are Gauss's law for electric and magnetic fields. Gauss's law for magnetic fields state that the divergence of the magnetic field at any point in space is zero. The main idea behind Gauss's law for electric fields is that the electric field produced by electric charge, diverges from positive charge and converges upon negative charge. In (2-6) ρ is the electric charge per m^3. With the assumption that the medium is homogeneous (2-6) simplifies to:

$$\nabla \cdot \vec{E} = 0 \tag{2-8}$$

2-1-1 Diffusion of EM-fields

Time-varying EM-fields that travel through space are described by Maxwell's equations (2-5) and (2-4). By using the constitutive relations $\vec{J} = \sigma\vec{E}$ and $\vec{B} = \mu_0\vec{H}$, equation (2-5) can be rewritten as

$$\nabla \times \vec{B} = (\mu_0\sigma\vec{E} + \varepsilon\frac{\partial \vec{E}}{\partial t}) \tag{2-9}$$

The first term on the right hand side represents the conduction current, whereas the second term represents the displacement current. Taking the curl of both sides of Faraday's law (2-4) gives

$$\nabla \times \nabla \times \vec{E} = -\nabla \times \frac{\partial \vec{B}}{\partial t} \tag{2-10}$$

Inserting $\nabla \times \vec{B}$ from (2-9) in (2-10) results in:

$$\begin{aligned} \nabla \times \nabla \times \vec{E} &= -\frac{\partial \mu_0(\vec{J} + \mu_0 \varepsilon_0 \frac{\partial \vec{E}}{\partial t})}{\partial t} \\ &= -\mu_0 \sigma \frac{\partial \vec{E}}{\partial t} - \mu_0 \varepsilon_0 \frac{\partial^2 \vec{E}}{\partial t^2} \end{aligned} \tag{2-11}$$

Applying a similar process with $\nabla \times \vec{E}$ gives the magnetic fields

$$\nabla \times \nabla \times \vec{B} = -\mu_0 \sigma \frac{\partial \vec{B}}{\partial t} - \mu_0 \varepsilon_0 \frac{\partial^2 \vec{B}}{\partial t^2} \tag{2-12}$$

These are the electromagnetic equations for propagation of electric and magnetic vectors in an isotropic homogeneous medium.

Using the vector identity $\nabla \times (\nabla \times \mathbf{v}) = \nabla(\nabla \cdot \mathbf{v}) - \nabla^2 \mathbf{v}$ (2-10) resolves in:

$$\nabla(\nabla \cdot \vec{E}) - \nabla^2 \vec{E} = -\mu_0 \sigma \frac{\partial \vec{E}}{\partial t} - \mu_0 \varepsilon_0 \frac{\partial^2 \vec{E}}{\partial t^2} \tag{2-13}$$

From Maxwell's equations it is given that $\nabla \cdot \vec{E} = \frac{\rho}{\varepsilon_0}$ and $\nabla \cdot \vec{B} = 0$, assuming that the medium is homogeneous gives $\nabla \cdot \vec{E} = 0$. Applying both to the electromagnetic propogation equations from above gives:

$$\begin{aligned} -\nabla^2 \vec{E} &= -\mu_0 \sigma \frac{\partial \vec{E}}{\partial t} - \mu_0 \varepsilon_0 \frac{\partial^2 \vec{E}}{\partial t^2} \\ \nabla^2 \vec{E} &= \mu_0 \sigma \frac{\partial \vec{E}}{\partial t} + \mu_0 \varepsilon_0 \frac{\partial^2 \vec{E}}{\partial t^2} \end{aligned} \tag{2-14}$$

and performing an identical process for magnetic fields results in:

$$\nabla^2 \vec{B} = \mu_0 \sigma \frac{\partial \vec{B}}{\partial t} + \mu_0 \varepsilon_0 \frac{\partial^2 \vec{B}}{\partial t^2} \tag{2-15}$$

Equation (2-14) represents a second order differential equation for $\vec{E}$. If the conduction current in this equation exceeds the diffusion current by several orders of magnitude, then equation (2-14) results in a diffusion equation given by:

$$\nabla^2 \vec{E} = \mu_0 \varepsilon_0 \frac{\partial \vec{E}}{\partial t} \tag{2-16}$$

However, if the displacement current is much larger than the conduction current, the equation will result in a wave equation

$$\nabla^2 \vec{E} = \mu_0 \varepsilon_0 \frac{\partial^2 \vec{E}}{\partial t^2} \tag{2-17}$$

The analysis of the second order differential equation (2-14) can be simplified by transforming the equation to the frequency-domain. Assume that the electric and magnetic fields have a harmonic variation at an angular frequency $\omega = 2\pi f$, then the time variable can be separated

from the electric field vector $\vec{E}(x,y,z,t) = \vec{E}_0(x,y,z)e^{-j\omega t}$, where $j = \sqrt{-1}$. Equation (2-14) in the frequency-domain can be expressed as:

$$\nabla^2\vec{E}_0 = -j\omega\mu_0\sigma\vec{E}_0 + \mu_0\varepsilon_0\omega^2\vec{E}_0 \tag{2-18}$$

Where the first term on the right hand side of the equation represents the conduction current, whereas the second term represents the displacement current. By introducing the wavenumber $k = \sqrt{\mu_0\varepsilon_0\omega^2 - j\omega\mu_0\sigma}$, the equation can be rewritten to:

$$(\nabla^2 + k^2)\vec{E}_0 = 0 \tag{2-19}$$

This equation contains the information that can be determined from the subsurface. The conductivity range of Earth materials can vary between $10^{-2} - 10^3 Sm^{-1}$. Geophysical EM exploration systems operate in the low-frequency range of 30 Hz - 300 kHz, therefore the first term of the wavenumber will be considerably small and negligible. As a result:

$$k^2 = -j\omega\mu_0\sigma \tag{2-20}$$

Which is also known as the condition of low induction numbers. The electric field in the Earth can then be expressed as:

$$\nabla^2\vec{E}_0 - j\omega\mu_0\sigma\vec{E}_0 = 0 \tag{2-21}$$

Taking the complex root of the wavenumber k gives

$$k = \frac{1}{\delta} + j\frac{1}{\delta} \tag{2-22}$$

In this equation, δ represents the skin depth and determines the penetration depth of electromagnetic waves at which meaningful information can be obtained. The limit at which the skin depth still provides meaningful information is commonly at a distance where the amplitude of the propagating electromagnetic wave in the subsurface has been attenuated to $\frac{1}{e}$, that is about 37% of it's value at the surface. The skin depth can be described as :

$$\delta = \sqrt{\frac{2}{\omega\mu\sigma}} \tag{2-23}$$

By substituting $\mu = \mu_0$ the skin depth equals:

$$\delta = \sqrt{\frac{2}{\omega\mu_0\sigma}} \approx 503\sqrt{\frac{\rho}{f}} \tag{2-24}$$

where, ρ is the resistance in Ωm^-1. Equation (2-24) indicates that the skin depth depends mainly on the resistance of the material and the frequency.

2-2 Electromagnetic Survey Methods

This section will outline geophysical survey methods that utilize the electromagnetic principles discussed in the previous section. EM exploration involves the propagation of continuous-wave

or transient electromagnetic fields in the earth. In most cases, inductive coupling between the soil and the exploration system is used to obtain information about the subsurface. A key advantage of inductive coupling is that it does not require direct contact with the ground to perform a measurement. Hence, this method is applicable for Airborne Electromagnetic (AEM). Exemplary applications of EM geophysical survey are:

- Geological mapping
- Groundwater survey
- Detection of metallic objects
- Mapping of pollution
- Investigating landfills

2-2-1 Time Domain Electromagnetics

The time domain EM method is a relatively young EM survey method compared to FDEM. This method really began to develop intensively since the mid 1980s. The TDEM measures the amplitude of a signal as a function of time. Widely used configurations employ a square or circular coil. The transmitter coil of the system conducts pulses of direct current and by abruptly turning off the constant current yields a transient EM field. By Faraday's law, this rapid change induces decaying Eddy currents in horizontal circles in the ground below the transmitter coil. The decaying Eddy currents will generate secondary magnetic fields that diffuse downwards in the conductive ground. The secondary fields expand outward with time and dissipate due to the ohmic losses of the conductor, often described as "smoke rings" diffusing in the ground. The time-rate of change of the secondary signal is measured by the receiver coil of the system. This measurement is done in the absence of the primary field, which decays when the transmitter coil is turned off. Hence, it is desirable for a TDEM system that after switching off the transmitter, the current returns to zero as rapidly as possible. Several TDEM instruments are on the market for airborne and ground surveys [9],[10].

2-2-2 Frequency Domain Electromagnetics

Typical Frequency Domain Electromagnetic (FDEM) systems are a two-coil system, in which one coil acts as a transmitter coil and the other coil as a receiver. The basic concept behind FDEM is that a transmitter coil conducting a controlled time harmonic alternating current generates a primary magnetic field in the space surrounding the coil. If the primary magnetic field propagates through the soil, it will induce small circular currents inside the soil, also known as Eddy currents. By Ampere's law, the Eddy currents in turn generate a weak secondary magnetic field that has the same frequency, but a lower amplitude and is shifted in phase. This secondary magnetic field contains the information about the subsurface. The receiver coil of the system measures the secondary magnetic field, as well as the primary magnetic field. Therefore, it would be convenient to eliminate the primary field at the receiver as much as possible. In that case, only the secondary field will be measured which can then

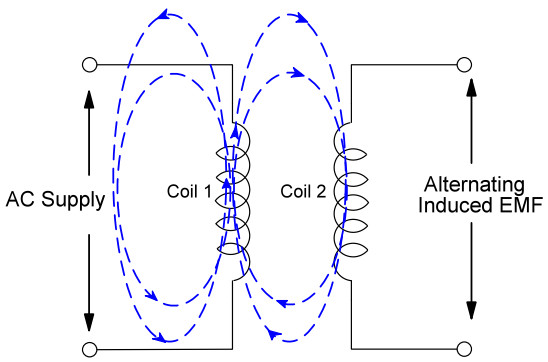

Figure 2-2: The principle of mutual induction.

provide the valuable information of the ground conductivities. The removal process of the primary field is typically realized through a compensation coil, commonly known as a bucking coil.

FDEM Principle of Operation

The principle of self-induction is that an Electromotive force (emf) is generated by a changing current in the same circuit, or the inductance L equals the induced voltage divided by the rate of change of electric current:

$$L = \frac{V}{\frac{di}{dt}} \tag{2-25}$$

with $\frac{di}{dt}$ being the current's rate of change in A/s. The voltage induced in the coil can be defined as:

$$V_L = -L\frac{di}{dt} \tag{2-26}$$

The negative sign in this equation comes from Lenz's law, which obey's Newton's third law of motion that says that for every force there is a reaction force, that is equal in magnitude but opposite in direction.

In a circuit model the FDEM method can be modeled as three separate inductors interacting with each other through mutual induction. A brief definition of mutual induction is the generation of a voltage in a coil, by a current flowing in an adjacent coil. Driving a current through a single coil will cause a magnetic flux due to that current. With mutual induction the magnetic flux in the first coil is linked with the second coil, which generates the emf as shown in Figure 2-2.

The magnetic flux through a coil k can be described as:

$$\phi = L_k I_k \tag{2-27}$$

where ϕ is the magnetic flux, L_k is the self-inductance of the coil and I_k is the current through the coil. Describing mutual induction mathematically gives:

$$M_{12} = -\frac{V_2}{\frac{di_1}{dt}} = -\frac{\phi_2}{i_1} \tag{2-28}$$

where, V_2 is the induced voltage in coil 2 by the change of current $\frac{di_1}{dt}$ in coil 1. Most conventional FDEM systems employ a horizontal co-planar configuration [11]. In this configuration there is maximum inductive coupling between the coils. With the Neumann formula the mutual induction for the horizontal co-planar system can be described as:

$$M_{12} = -\frac{\mu_0 \pi r_1 r_2}{4l^3} \tag{2-29}$$

in which M_{12} is the mutual induction, r_1 and r_2 are the radius of the respective coils and l is the spacing between the two coils. The basic principle behind co-planar EM methods is to measure the mutual induction between the transmitter loop and receiver loop. Changes in the mutual induction are interpreted as being due to the presence of subsurface conductors. During operation, the primary and secondary currents flow in the same direction hence, the mutual induction is negative due to Lenz's law. When sinusoidal signals are added together, the phase of the signal should be taken into account. A signal is regarded as in-phase when it has 0° difference and corresponds with a sine-wave signal. If a signal has a 90° phase difference and corresponds with a cosine-wave it is regarded as out-of-phase.

2-2-3 Amplitude and Phase Relation

As discussed in the previous section, the horizontal co-planar FDEM system can be modeled as three separate coils as shown in Figure 2-3. A sinusoidal time-varying current through the transmitter coil in the form of:

$$i_{IN(t)} = I_{IN} e^{j\omega t + \phi}, \tag{2-30}$$

will generate a primary alternating magnetic field in the conductor. Where, I_{IN} is the amplitude of the input current, ω its angular frequency and ϕ the phase. The primary magnetic field can then be defined as:

$$H_P^C = K_{TC} I_{IN} e^{j\omega t + \phi} \tag{2-31}$$

In here:

$$K_{TC} = \frac{M_{TC}}{\sqrt{L_T L_C}} \tag{2-32}$$

is the coupling coefficient between the transmitter coil and conductor and $0 \leq K_{TC} \leq 1$. The coupling coefficients depends on the geometry of the system, coil properties and electromagnetic wave attenuation. L_T and L_C are the self-inductances of the transmitter coil and conductor. Due to mutual induction between the transmitter coil and conductor (M_{TC}), a voltage typically referred to as secondary voltage $V_s(t)$ will be induced in the conductor, which is given by:

$$V_s(t) = -M_{TC} \frac{di_{IN}}{dt} \tag{2-33}$$

Using equation (2-30), $V_s(t)$ can be expressed as:

$$\begin{aligned} V_s(t) &= -(M_{TC})(j\omega)(I_{IN} e^{j\omega t + \phi}) \\ &= -j\omega \frac{M_{TC} H_P^C}{K_{TC}} \end{aligned} \tag{2-34}$$

Equation (2-34) shows that there is 90° phase shift between $V_s(t)$ and H_P^C due to $-j = e^{-\frac{j\pi}{2}} =$ 90° component. With the impedance of the conductor, the current flowing through the

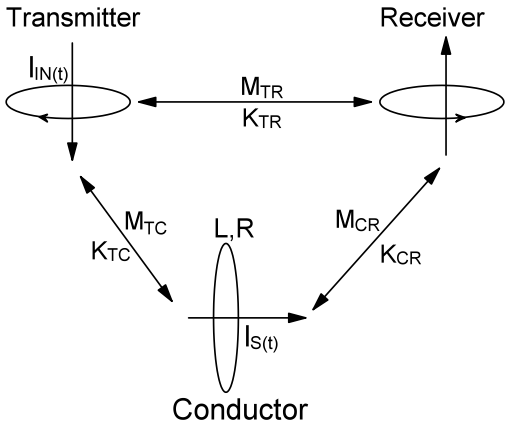

Figure 2-3: Horizontal co-planar loop system model.

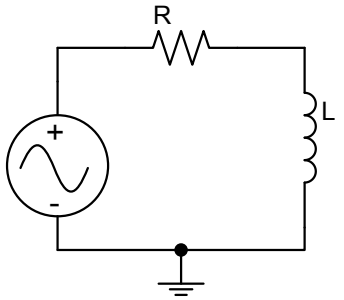

Figure 2-4: Circuit model of the conductor with series RL impedance.

conductor can be defined. The conductor impedance can be modeled as an LR series circuit as depicted in Figure 2-4. The voltage $V_s(t) = V_s e^{j}\omega t$ will produce a current $i_s(t) = I_s e^{j\omega t}$ that will flow through the circuit.

By Kirchoff's law, the applied voltage $V_s(t)$ to the circuit must equal the voltage drop across the impedance, thus:

$$\begin{aligned} V_s e^{j\omega t} &= I_s e^{j\omega t} R_c + L_c \frac{di_s}{dt} \\ &= I_s e^{j\omega t} R_c + j\omega t L_c I_s e^{j\omega t} \end{aligned} \tag{2-35}$$

which can be resolved to:

$$V_s e^{j\omega t} = I_s(R_c + j\omega L_c) = I_s Z_c \tag{2-36}$$

where, Z_c is the effective impedance of the conductor. The secondary magnetic field which corresponds with the receiver coil, is a result of the current flowing in the conductor and can be described as:

$$\begin{aligned} H_S^R &= K_{CR} i_s \\ &= -\frac{K_{CR} j\omega M_{TC} H_P^C}{K_{TC}(R_c + j\omega L_c)} \\ &= -\frac{K_{CR} j\omega M_{TC}(R_c - j\omega L_c)}{K_{TC}(R_c^2 + (\omega L_c)^2)} \end{aligned} \tag{2-37}$$

By introducing the response parameter $Q = \frac{\omega L_c}{R_c}$, which is a figure of merit that determines whether an inductive or galvanic response dominates the impedance, equation (2-37) can be written as:

$$H_S^R = -\frac{K_{CR} j\omega M_{TC}(Q^2 + jQ)}{K_{TC} L_c (1 + Q^2)} \tag{2-38}$$

The primary magnetic field that is generated due to the current $i_{IN}(t)$ flowing through the transmitter coil, is also coupled with the receiver coil of the system and is commonly referred to as the primary field at the receiver H_P^R. Using equation (2-30) for the current I_{IN}, the

primary field at the receiver yields:

$$H_P^R = K_{TR} I_{IN} = \frac{K_{TR}}{K_{TC}} H_P^C \tag{2-39}$$

Since there is also the secondary field (2-37) generated in the conductor that is coupled with the receiver coil, the total magnetic field at the receiver coil is the sum of the primary and secondary magnetic fields:

$$H_T^R = H_P^R + H_S^R \tag{2-40}$$

When adding the primary and secondary magnetic fields, the phases of the fields should be taken into account. The primary magnetic field has zero phase shift. The phase of the secondary magnetic field at the receiver coil can be found by:

$$\Big(\arctan(\phi) + \frac{\pi}{2}\Big) = \Big(\frac{R_c}{\omega L_c} + \frac{\pi}{2}\Big) \tag{2-41}$$

where, the $\frac{\pi}{2}$ component is due to the inductive coupling between the transmitter coil and the conductor as indicated in equation (2-34). In the case that the conductor has zero resistance $R_c = 0$, it is considered to be a "good conductor" and the secondary field H_S^R will be in phase with H_P^R, so that the phase shift will be $\phi = 0°$. A "bad conductor" is when the secondary field H_P^R will be in quadrature (out of phase) with the primary field, that will be the case when R_c has a large value. The total magnetic field at the receiver has a magnitude of H_T^R and a phase α. Typically, the secondary field at the receiver (H_S^R) will be 90° to 180° out of phase with the primary field (H_P^R). Since $H_S^R << H_P^R$, it is easier to measure the in-phase and out of phase components at the receiver to obtain information about the conductor. By dividing equation (2-38) with (2-39), the magnitude of the in-phase and out of phase components of the total magnetic field at the receiver coil can be expressed:

$$\frac{H_S^R}{H_P^R} = -\frac{K_{CR} M_{TC}}{K_{TR} L_C} \frac{(Q^2 + jQ)}{(1 + Q^2)} \tag{2-42}$$

where, the first ratio involves the coupling coefficients between the conductor and receiver coil (K_{CR}), transmitter and receiver coil (K_{TR}), mutual inductance and self-inductance of the conductor. Note that his ratio is relatively small, due to the coupling coefficient value of K_{TR} is much higher than the terms in the numerator. The in-phase and out of phase components can be derived by taking the real and imaginary part of equation (2-42):

$$A = Re\Big\{\frac{H_S^R}{H_P^R}\Big\} = -\frac{K_{CR} M_{TC}}{K_{TR} L_C} \frac{(Q^2)}{(1 + Q^2)} \tag{2-43}$$

and,

$$B = Im\Big\{\frac{H_S^R}{H_P^R}\Big\} = -\frac{K_{CR} M_{TC}}{K_{TR} L_C} \frac{(Q)}{(1 + Q^2)} \tag{2-44}$$

where, A is the in-phase component and B is the out of phase component. The second factor of both equations depends solely on the conductor. With a varying operating frequency, only the second factor in A and B will vary. Equations (2-43) and (2-44) can be used to express the response function:

$$f(Q) = A + jB = \frac{Q^2 + jQ}{1 + Q^2} \tag{2-45}$$

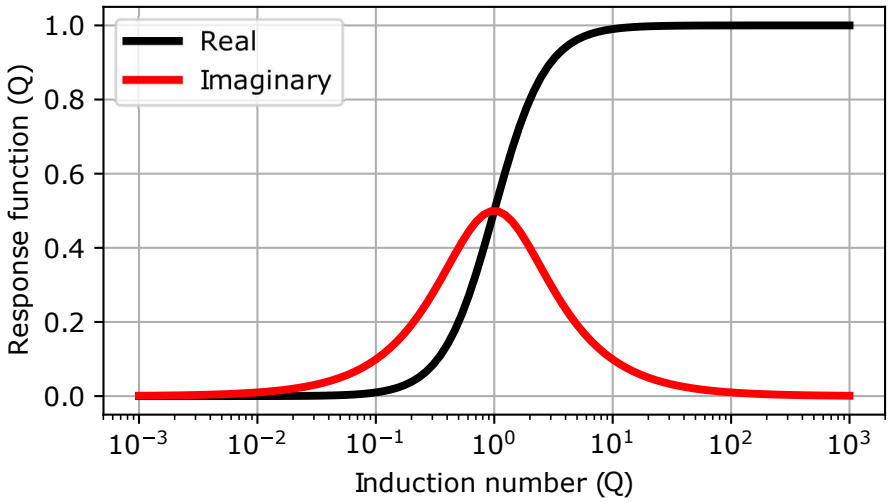

Figure 2-5: Response function f(Q) of a horizontal co-planar system

This function describes the electromagnetic response from conductive ground structures to an EM-field excitation. From equations (2-43), (2-44) and (2-45) it becomes clear that the parameters affecting the response function are the operating frequency, size and conductivity of the target, configuration and geometry of the coils. Figure 2-5 shows the response function for a homogeneous ground. For this figure the assumption has been made that the geometry of the conductor is fixed and that only the angular frequency ω varies. At very low frequencies the generation of secondary fields and currents in the conductor will be below the minimum, as a result the quadrature and in-phase component have no response. At intermediate frequencies the quadrature components rises to a peak value, with the maximum value at Q=1. At higher frequencies, the quadrature component goes to zero and the response will be in-phase.

2-3 Summary

This chapter started with the basic fundamentals of electromagnetic theory to provide an intuitive understanding of the physics behind the proposed Proof-of-Concept in this work. First, the EM field was described by its components and constitutive relations. Followed by a discussion of Maxwell's equations. By combining Maxwell's equations and the constitutive relations, the diffusion of EM fields were discussed. Finally, an overview of EM survey methods in the time domain and frequency domain has been given, where the latter was discussed in greater detail as it is the method of interest for this work.

Chapter 3

System Architecture

This chapter presents the proposed system architecture for an EM survey instrument based on FDEM principles discussed in section 2-2-2. The operating principle behind this architecture will be discussed first and an overview of the concept is given in a system block diagram. In the remainder of this chapter, each block of the system will be described.

A typical block diagram of a portable electronic measurement system is shown in Figure 3-1. The transducer interfaces the electronic system with real world analog variables and converts this into an electrical signal. Normally, the transducer output signal does not match the analog-to-digital (A/D) block's input range; consequently, amplification of the transducer signal is needed. A digital-to-analog (D/A) block drives the transducers to interface with its operating environment and additional bias circuits or amplifiers are needed for a proper signal propagation. In order to perform these tasks, the system needs to be powered by a power supply block. This relatively straight forward block diagram provides the framework for the Proof-of-Concept in this work and will be explained in greater detail in the next section.

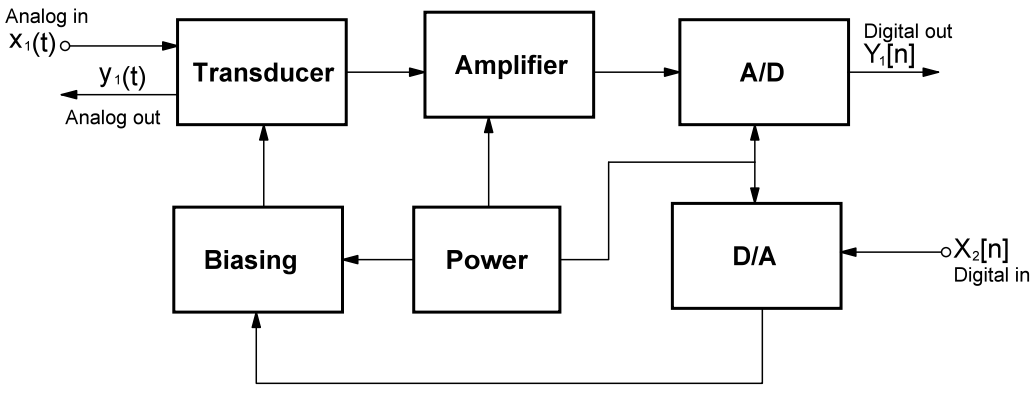

Figure 3-1: Typical block diagram of a portable electronic measurement system

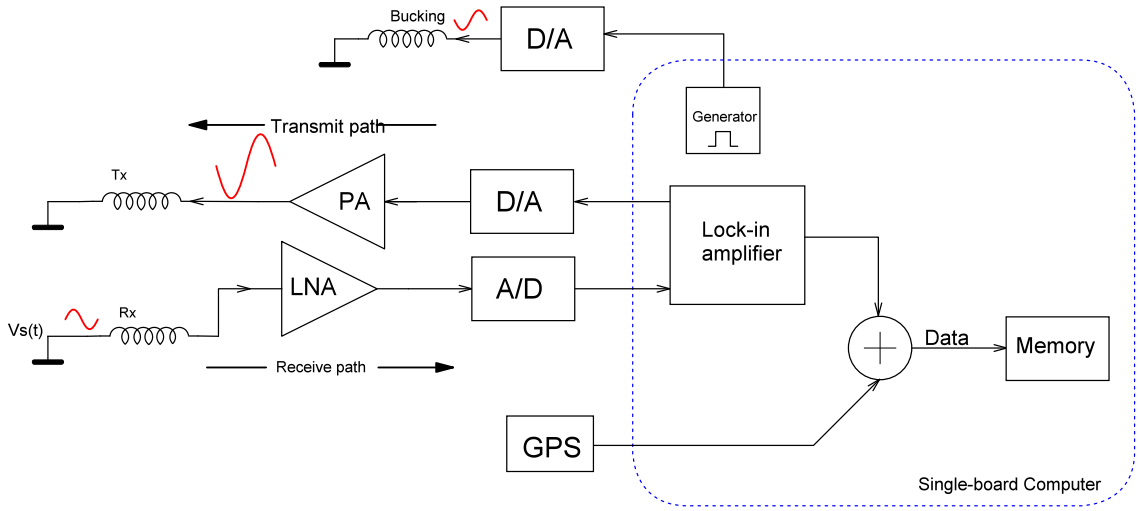

Figure 3-2: Functional block diagram of the system architecture

3-1 Overview of the Concept

Operating principle The block diagram of the proposed FDEM system is illustrated in Figure 3-2. The concept can be explained as follows: The Single-board Computer (SBC) operates the overall system. A time-varying signal that originates from the SBC, will drive the transmitter (Tx) coil. To drive a high current through the Tx coil, the signal needs to be amplified by a Power Amplifier (PA). Since the SBC generates a digital signal, a digital-to-analog signal conversion is needed. Similarly, the receiver coil (Rx) yields an analog time-varying signal that needs to be converted into a digital signal for further signal processing in the digital domain. The inductive coupling between the receiver coil and the subsurface of the Earth is rather small. As a result, it generates a very small voltage in the receiver coil that can be close to the noise level (nanovolt range), which lies outside the range of the A/D converter input. A Low-noise amplifier (LNA) can overcome this issue by providing enough gain without adding any further significant noise to the signal. The final signal processing will be done by a digital Lock-in Amplifier that runs on the SBC. The SBC also generates a reference signal that will be used to drive the bucking coil. A Global Positioning System (GPS) board is connected to the Raspberry Pi to provide location data and synchronize the system clock with the GPS clock.

The design considerations have been made such that the blocks comply with the core specifications of Table 1-1. The list below sums up the major blocks of the system as depicted in Figure 3-2:

- Coils
  - Transmitter coil
  - Receiver coil
  - Bucking coil

- Low-noise amplifier (LNA)
- Power Amplifier (PA)
- Digital-to-Analog converter
- Analog-to-Digital converter
- Single-board Computer
  - Lock-in Amplifier (LIA)
- Global Positioning System (GPS)

3-2 Coils

Function The coils are the transducers and actuators of the FDEM measurement system. They interface magnetic fields with the electronics of the system. Specifically, the receiver coil functions as the sensor of the system and the transmitter and bucking coil function as the actuators of the system. The transmitter generates a primary magnetic field that will propagate in the subsurface of the Earth. The receiver coil will detect the (weak) secondary magnetic field that is generated in the subsurface due to the primary field. From the bucking coil, it is expected to cancel out the primary magnetic field at the receiver coil.

Design consideration The magnetic flux density ($\vec{B}$) that is generated by each coil depends on several factors, mainly the coil geometry, total wire length and wire thickness. The parameters that are affected by the coil design are electrical resistance, noise and weight. Care has to be taken during the design of the coils that it will not negatively affect the mentioned parameters. The total weight of the coils should not exceed the maximum payload (<10 kg) of the UAV. Furthermore, the coils should not introduce excessive noise that will disturb the signals of interest.

3-2-1 Coil Model Analysis

The initial coils for the Proof-of-Concept were provided by SkyDowser and consisted out of three identical coils. Table 3-1 list their specifications. Modeling the coils helps with the design procedure of the coils and gives a clear insight in the trade-offs between various parameters like voltage, noise and weight. It also shows the relation between magnetic flux, coupling and mutual inductance. Figure 3-3 shows the coil model, where M_{12}, M_{23} and M_{13} are the mutual inductances of the coils. The intercoil distance is 4 m, which matches the wingspan of the UAV. The total distance from the center of the transmitter and receiver coils to the conductor coil is 40 m. This was determined by the flight altitude of 30 m and the conductor (groundwater) depth that is assumed to be at 10 m. Please note that the dimensions in this figure are not scaled to proportion. Further, it should be noted that this is a simplified analysis where several external factors (surrounding noise sources, layered earth, flight disturbances) have not been taken into account. From this model an estimation can be made of the generated voltages. The voltage generated in the receiver coil due to the mutual

inductance with the conductor will have the main interest, as this voltage will be processed by the electronic circuit block. The conductor is modeled as an ideal coil and its specifications are given in Table 3-2.

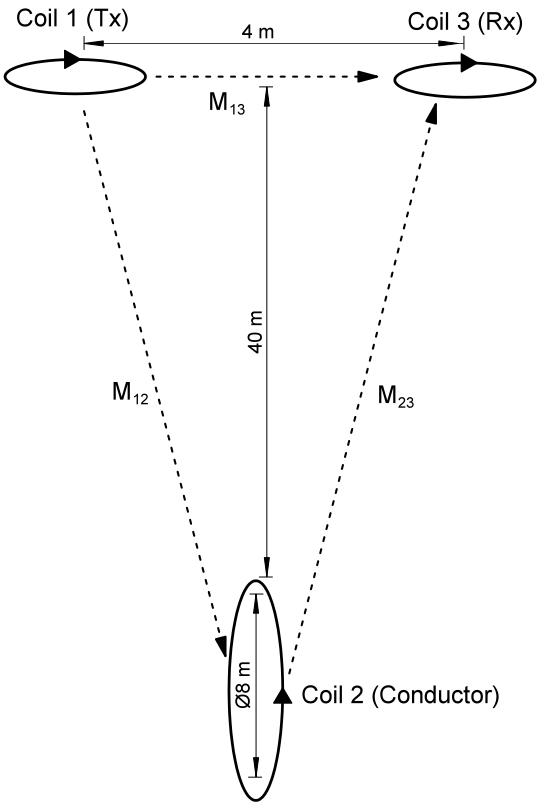

Figure 3-3: Three coil model of the proof-of concept.

Mutual inductances The mutual inductance relation between the transmitter and receiver coil can be expressed as:

$$M_{13} = -\frac{\pi \mu_0 r_1^2 r_3^2}{4l^3} \tag{3-1}$$

where, r_1 and r_2 are the radian of the transmitter and receiver coils, l is the intercoil distance. The mutual inductances between the conductor and transmitter, and conductor and receiver can be written with the following equation:

$$M_{12,23} = \frac{\mu_0 N_1 N_2 r_1^2 r_3^2}{\sqrt{(r_1 + r_3)^2 + h^2}(r_1 - r_3) + h^2} \tag{3-2}$$

where, h is the total distance from the transmitter or receiver coil to the conductor coil, r_1 is the transmitter radius (interchange with r_2 for receiver) and r_3 is the radius of the conductor coil [12].

Magnetic fields and voltage relation The magnetic field density from the transmitter coil at the conductor can be described as:

$$\vec{B}_{TC} = \frac{\mu_0 N I r_1 \pi^2}{2\pi h^3} \tag{3-3}$$

Magnetic flux is defined as the total number of magnetic field lines passing through a given area. Mathematically it can be described as:

$$\Phi = \vec{B} A \cos(\theta) \tag{3-4}$$

in which, A is the surface area and θ defines the angle between the magnetic field $\vec{B}$ and the normal to the surface area A. In case that the surface area is perpendicular to $\vec{B}$, then the angle is zero and the magnetic flux equals the product of $\vec{B}A$. It is evident from equation (3-4) that the flux is proportional to the area and the magnetic field intensity $\vec{B}$. Thus, to increase the flux it is desired to increase the surface area and $\vec{B}$. The flux in the receiver coil due to coupling with the transmitter coil can be written as:

$$\Phi_{TR} = \frac{M_{13}}{N_R} I_{transmitter} \tag{3-5}$$

This relates to the voltage generated in the receiver as:

$$V_{TR} = j\omega \Phi_{TR} N_R \tag{3-6}$$

The voltage generated in the conductor was given in equation (2-33), applying that equation to the model results in:

$$V_{conductor}(t) = -j\omega \frac{M_{12} B_{TC}}{K_{TC}} \tag{3-7}$$

The current that flows through the conductor generates a voltage in the receiver coil due to mutual inductance. By using the magnetic field intensity and mutual inductance this results in:

$$V_{CR} = -j\omega \frac{\Phi_{CR} N_R}{K_{TC}} \tag{3-8}$$

where, $\Phi_{CR} = M_{23} I_{conductor}$, which is the flux through the receiver coil. From these equation, it can be concluded that the generated voltage in the receiver coil relates directly to the number of turns of the receiver coil and the area of the coil, which in turn is related to the mutual inductance. With these equations and the given model of Figure 3-3 some hand-calculations were performed. The purpose of these hand-calculations is to obtain an insight in the magnitude of voltages at the receiver coil, rather than exact numerical values. Extensive electromagnetic modeling is discussed in the work of [13],[14]. Based on these hand-calculations and model, a new receiver coil was designed and the implementation of this coil is described in chapter 4.

Table 3-1: Parameters of Sky-Dowser's original coils

Parameter	Value
Windings	780
Inductance	27.1 mH
Inner diameter	30 mm
Outer diameter	83 mm
Max. current	2.0 A
DC Resistance	6-8 Ω
Weight	495 grams

Table 3-2: Conductor coil specifications

Parameter	Value
Windings	1
Inductance	21.1 μH
Diameter	8 m
Outer diameter	-
Length	3 m
Material	Groundwater
Resistivity	85 $\Omega \cdot m$
DC Resistance	5.1 Ω

3-3 Low Noise Amplifier

Function An ideal operational amplifier has no noise contribution to the signal of interest. However, a practical op-amp contains noise sources from the complex integrated circuit comprising transistors and capacitances. A Low-noise amplifier (LNA) is a type of amplifier that increases a very low-power input signal to the output, such that the output signal is not degraded significantly by the internal noise of the amplifier. Ideally, the LNA block will provide sufficient gain to the incoming signal from the receiver coil, hence it will exceed the noise floor and can be further processed by the digital acquisition block of the system. The LNA plays an important role in determining the performance of the overall system. Hence, it is worth reviewing some fundamental performance parameters of the op-amp to set up requirements for the amplifier of choice.

3-3-1 Performance Parameters

Gain An amplifier is an electronic device that generates an output signal that is proportional to the input signal. The proportionality constant is referred to as the *gain* of the amplifier. For a linear voltage amplifier, the open-loop gain is given as:

$$A = \frac{V_{\text{out}}}{V_{\text{in}}} \tag{3-9}$$

Connecting a negative feedback network to the amplifier is a widely used method to set the desired gain and is depicted in Figure 3-4. The feedback network is determined by the configuration of the amplifier circuit. From Figure 3-4 the closed-loop gain can be derived from the overall transfer function:

$$H(s) = \frac{V_{out}(s)}{V_{in}(s)} = \frac{1}{1 + A\beta} \tag{3-10}$$

where, the term β is the feedback network and A is the amplifier with an open-loop gain of A, the product of these two terms form the *loopgain(T)* of the system. If the loop gain T =

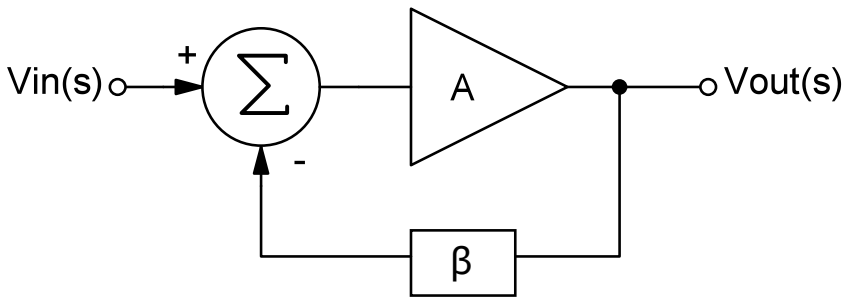

Figure 3-4: Canonical form of an ideal op-amp connected in negative feedback.

$A\beta$ is » 1, then equation (3-11) reduces to:

$$H(s) = \frac{V_{out}(s)}{V_{in}(s)} = \frac{1}{\beta} \tag{3-11}$$

and the closed-loop gain (A_{cl}) of the LNA will be completely determined by the feedback of the system. Connecting the LNA in this fashion has several benefits:

1. The integrated circuit of an amplifier consists mostly of transistors, which can suffer from parameter changes due to aging effects, temperature dependence and frequency effects. These parameter changes of the active devices affect the openloop gain. A negative feedback network stabilizes the gain of the amplifier and does not suffer significantly from these parameter changes.

2. Reduces distortion of the output signal.

3. It can manipulate the bandwidth of the system.

However, there are some drawbacks by connecting a negative feedback. First, the gain of the amplifier is attenuated, which is not a big issue since modern-day amplifiers have a high open-loop gain, but it needs to be taken into account during the design of the amplifier circuit. To make up for the gain loss, extra stages can be added to the circuit to increase the overall gain. A more severe issue is unwanted oscillation in the circuit, that can occur if there is an excessive phase shift of the feedback loop. Typically, this occurs at higher frequencies due to high frequency effects of active devices. Therefore, stability and frequency compensation techniques need to be employed to overcome these limitations [15].

Bandwidth Together with sufficient gain, the LNA needs to have a bandwidth that covers the operating frequencies of the FDEM measurement system. A LNA has a certain Gain-Bandwidth Product (GBWP), which is a fixed parameter and is determined by the integrated circuit. It can be defined as the product of open-loop gain and the frequency at which it is measured. Basically, the GBWP determines the trade-off between gain and bandwidth of the

amplifier. The point at which the GBWP is unity, is known as the unity-gain frequency. The bandwidth can be determined as:

$$\text{Closed-loop bandwidth} = \frac{\text{GBWP}}{A_{\text{cl}}} \tag{3-12}$$

Generally, the closed-loop gain is inversely proportional to the closed-loop bandwidth and is determined by the feedback factorβ. If β increases, the closed-loop bandwidth increases and the closed-loop gain decreases with the same factor. For a stable operation, the desired gain of the amplifier needs to be constant over the closed-loop bandwidth. The stability of the LNA is determined by how the loop gain (T) varies with frequency. Equation (3-10) showed the transfer function, where it can be seen that if the loop gain T = $A(s)\beta$ equals -1, the amplifier will become unstable and starts to oscillate at that particular frequency ω. This condition can also be expressed as:

$$|\beta A(j\omega)| = 1 \tag{3-13}$$
$$\angle\beta A(j\omega) = -180^\circ \tag{3-14}$$

These values are critical for the stability of the system and need to be avoided. A useful measure of stability is the *Gain Margin (GM)*:

$$\text{GM (dB)} = 20 \cdot log\frac{1}{|T(\omega_{-180^\circ})|} \tag{3-15}$$

where, ω_{-180° is the angular frequency at which the phase angle is -180°. It can be described as the absolute value of the difference in gain, at the point where the gain is unity and where the gain at the phase angle is -180°. This is measured in decibels (dB) and safe margin is around 14 dB [16]. The *Phase Margin* provides another way to determine the stability by looking at the phase shift at the frequency where the gain is unity. The Phase Margin is defined as:

$$\phi_m = 180^\circ + \angle A\beta_{(j\omega)} \tag{3-16}$$

For a sufficient margin, the phase of $A\beta$ should not be close to 180°. A safe value of phase margin is typically around 60°. The phase margin and GM are often plotted on a bode-plot, which ables to graphically determine the frequency response of the LNA. It becomes clear that there is a trade-off between the gain and bandwidth, both of these design parameters are configured by the feedback network. Hence, a careful study of the frequency response is critical, when designing the feedback network for the LNA [17].

Noise The unwanted disturbance that interferes with a signal of interest is considered as noise. Due to its stochastic nature, the instantaneous value of noise cannot be predicted. Therefore, the noise parameter needs to be determined on a statistical basis. This makes noise an important design parameter for the LNA circuit. In an op-amp circuit there are *intrinsic* and *extrinsic* noise sources, where the intrinsic noise is contributed by the internal circuit of the op-amp which can consist of transistors, diodes, capacitors and resistors. Internal generated noise sources are referred to the amplifier's input as: input-referred voltage noise and input-referred current noise. Another intrinsic noise source is *flicker noise*, commonly referred as 1/f noise and is often caused by defects in the crystalline structure of the

active device. The 1/f noise source is inversely proportional to the frequency and for a LNA calculated as:

$$i_n^2 = K\frac{I^a}{f} \tag{3-17}$$

where, K is a device constant, I is the DC-current and a is another device constant. Extrinsic noise sources are the noise contributions from the components that are part of the amplifier circuit, often from the feedback network comprising of passive elements. The random thermal motions of electrons in a conductor generates a noise voltage across the conductor, which is an unwanted effect known as *thermal noise*. The thermal noise for a resistor is defined as:

$$e_r = \sqrt{4kTR} \tag{3-18}$$

where, k is Boltzmann's constant ($1.38\times10^{-23}J/K$), T the absolute temperature in Kelvin(K) and R the resistance in ohm. Noise is a frequency dependent signal, where the 1/f noise dominates in the lower region of the bandwidth of the LNA. Beyond the 1/f corner frequency, a phenomena known as *white noise* starts to dominate. Unlike 1/f noise, white noise has a flat spectral density and does not vary with frequency. The white noise floor is proportional to the frequency band and often comprises thermal noise from the feedback network. To minimize the contribution of white noise, the bandwidth should be limited to the required minimum and is also referred to as the *Noise Equivalent Bandwidth* [18]. This is illustrated in Figure 3-5.

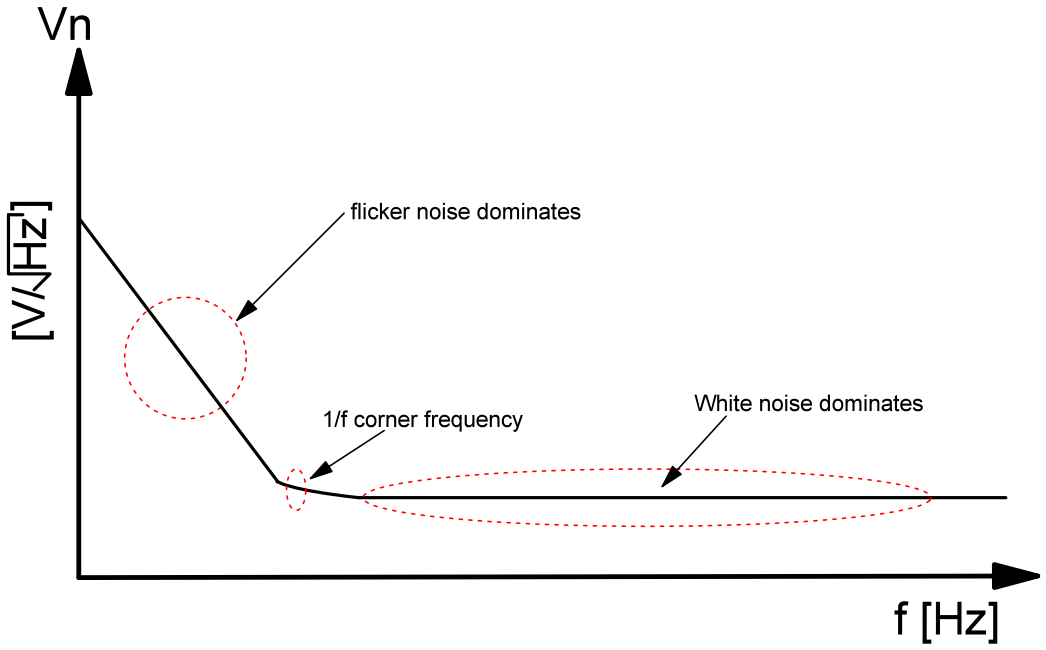

Figure 3-5: Input noise voltage plot vs. frequency of a LNA. At the 1/f corner frequency point, the white noise floor equals that of the 1/f noise.

The *voltage noise spectral density* is an important characteristic of noise, which is the measurement of RMS-noise per unit of bandwidth. With multiple uncorrelated noise sources in an amplifier circuit, the noise signals can be added together by the "root-sum-of-squares". However, to determine the total noise of an amplifier circuit, the density function is often converted into RMS-noise, which in turn is converted into a peak-to-peak value. Since noise has a Gaussian probability function its value cannot be predicted with 100% accuracy, thus the RMS-value needs to be multiplied with a proper standard deviation for an estimation accuracy of the noise signal. Table 3-3 lists the number of standard deviations and the estimation accuracy for which the amplitude of the peak-to-peak value is accurate and does not exceed the amplitude. It is clear to see that with an increasing number of standard deviations, the accuracy of the peak-to-peak value increases. Typically a value of 6σ or 6.6σ is used to estimate an accurate peak-to-peak value of the LNA RMS-noise [19].

Number of Standard deviations	**Estimation accuracy (%)**
2σ	68.3
3σ	86.6
4σ	95.4
5σ	98.8
6σ	99.7
6.6σ	99.9

Table 3-3: Number of standard deviations and estimation accuracies.

Design requirements and consideration Similar to the design of the coils, the noise parameter plays a crucial role at this block. The incoming signals from the receiver coil can be close to the level of the intrinsic noise sources of the LNA. Hence, it is critical that the receiving signal does not get buried within the noise of the LNA. Therefore, a Low-noise amplifier (LNA) with low input noise current and input noise voltage source should be chosen. The bandwidth of the LNA should support the requirement of operating between the range for FDEM(30 - 100.000 Hz). Thus, the feedback network should be designed such that it rejects high-frequency noise, DC and low-frequency noise, and power-line harmonics. Power consumption is an important design parameter in most applications, however for this first concept it has not been taken into account. The focus is mainly on the noise performance of the LNA. From the discussed LNA parameters it becomes evident that the feedback network needs to be designed carefully in order to ensure sufficient GM and phase margin (ϕ_m), which will lead to low noise and a stable gain over the desired bandwidth. The specifications for the LNA are partially dependent on the selected A/D converter, hence a full specification can not be given without taking the parameters of the A/D converter and receiver coil into account. Although, from the discussed paragraphs certain specifications can be derived and these are listed in Table 3-4. The gain of the amplifier should be such that the generated receiver output voltage matches the input voltage range of the A/D converter. In the next chapter, the analog circuit design and analysis of the LNA will be discussed thoroughly.

Design specification	Value
Bandwidth	30 - 100.000 Hz
Gain	$\frac{V_{in,ADC}}{V_{out,receivercoil}}$
Phase margin	$45 - 60°$
Gain margin	≈14 dB
Power consumption	-
Noise	$< V_{out,receivercoil}$

Table 3-4: Design specifications of the LNA.

3-4 Data Conversion

Funtion This block provides the conversion of analog signals from the Low-Noise Amplifier block into digital codes that will be processed by the Single-board Computer (SBC). In the opposite direction, the digital-to-analog (D/A) conversion generates a time-varying signal from the digital codes from the SBC. This signal will first be amplified by a Power Amplifier (PA), to then drive the transmitter and bucking coil. To select a proper A/D converter and D/A converter for the proposed system, an overview will be given of important performance parameters used for characterizing data converters [20],[21].

Sampling rate The sampling rate (f_s) of an A/D converter is the rate at which samples are taken from the analog time-continuous signal and transformed into time-discrete signals, where in general a higher sampling rate results in a more accurate digital representation of the sampled signal. If a time-continuous signal is sampled below a certain rate, then critical information about the original signal will be lost and a correct replica of the signal is not possible. To perform a correct A/D conversion, the sampling rate f_s should be chosen twice as large as the highest frequency component of the sampled signal, else a phenomena known as *aliasing* will occur. Aliasing is an unwanted effect that causes signals to become indistinguishable . The limitation of the sample rate to prevent aliasing is given by the Nyquist criterion and mathematically it can be expressed as:

$$f_s = 2BW \tag{3-19}$$

where, BW is the bandwidth in the time-continuous domain. A low-pass filter, also referred as an *anti-alias filter* in this case, is often employed to limit the bandwidth of the analog signal to $f_s/2$, which is known as the Nyquist frequency.

Resolution and accuracy The resolution of an A/D converter is defined as the theoretical number of discrete values that the analog input can be divided into and is given in bits. From the resolution of the ADC, the number of maximum step sizes can be determined:

$$\text{ADC} = 2^N \tag{3-20}$$

The least-significant bit (LSB) value can be calculated as:

$$\text{LSB} = \frac{V_{fs}}{2^N} \tag{3-21}$$

where, V_{fs} is the full scale voltage range and is the maximum voltage that the A/D can convert. The LSB is the lowest voltage value that the ADC can represent. The theoretical resolution of an A/D converter is often not achieved, due to quantization noise and several sources of errors like *Differential non-linearity*, *Integral non-linearity*, gain and offset error. The DNL error is the deviation of a step size of an actual data converter from the ideal step size. Where the INL is defined as the deviation of the actual transfer function from the straight line through the endpoints of the ideal transfer function. A more common way to measure the INL, is by looking at the deviation of a best-fit line, which corrects for gain and offset errors. These non-linearity errors are displayed in Figure 3-6.

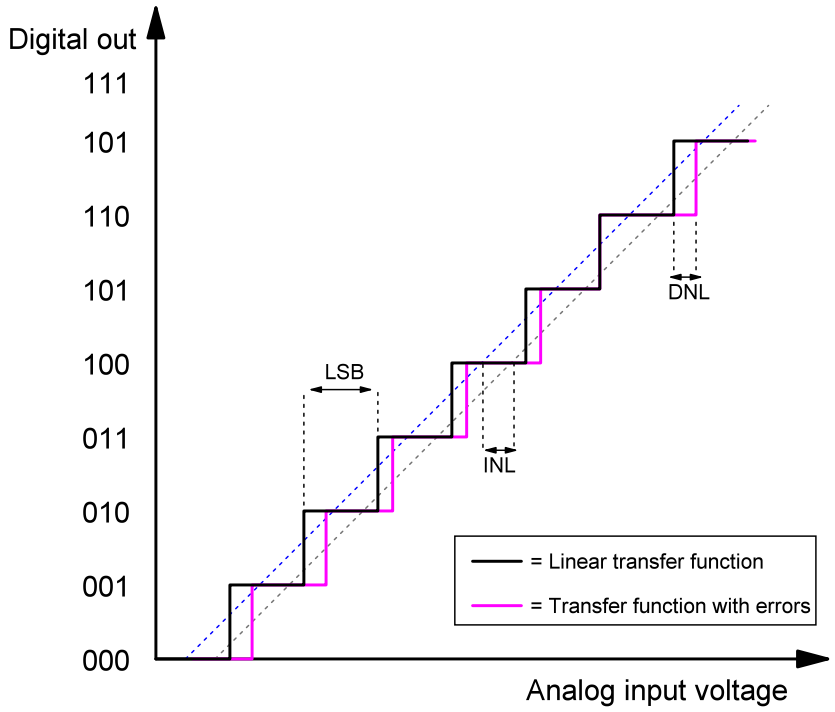

Figure 3-6: Transfer function of a 3-bit A/D converter.

The signal-to-noise ratio (SNR) of an ADC is defined as the power of the signal and the total noise of the ADC circuit. This is given as:

$$\text{SNR (dB)} = 1.76 + 6.02N \tag{3-22}$$

where, N is the resolution of the ADC and the SNR is defined for the noise in the bandwidth of the Nyquist frequency. The SNR defines how much the input signal is corrupted by noise. If the non-linear distortion terms, generated by the input signal, are also taken into account, then the parameter Signal-to-Noise-and-Distortion-Ratio (SNDR) is defined. Mathematically described as:

$$\text{SNDR} = 10\log\left(\frac{\text{Signal power}}{\text{Power of total noise + distortion}}\right) \tag{3-23}$$

The SNDR gives a good indication of the overall dynamic performance of the A/D converter, because it includes all components which make up distortion and noise. The real performance of a data converter is given by the Effective number of bits (ENOB). For an ideal 'n' bit A/D converter with a sinusoidal input signal, the ENOB is expressed as:

$$\text{ENOB} = \frac{\text{SNDR} - 1.76}{6.02} \tag{3-24}$$

The ENOB measures the SNDR using bits.

3-4-1 ADC Architecture

The architecture of an A/D converter determines the performance in terms of power, speed, resolution and accuracy. The most popular ADC architectures available on the market are Successive approximation register (SAR), Sigma-delta ($\Sigma\Delta$), Pipelined and Flash architecture. In Figure 3-7 a plot is given of these architectures with the trade-off between resolution and bandwidth [22]. A Dual-slope ADC is also a popular architecture, however the slow speed of this architecture makes it irrelevant for the proposed system. The sampling rate needs to adhere to Nyquist's criterion to avoid aliasing, therefore the bandwidth of the time-continuous analog signal is limited to maximum FDEM bandwidth of 100.000 kHz. This rules out flash and pipelined architectures, as these are employed for high speed and large bandwidth applications. A quick overview limited to SAR and delta-sigma converters will be given to determine which architecture will suit the task of A/D conversion in the proposed system.

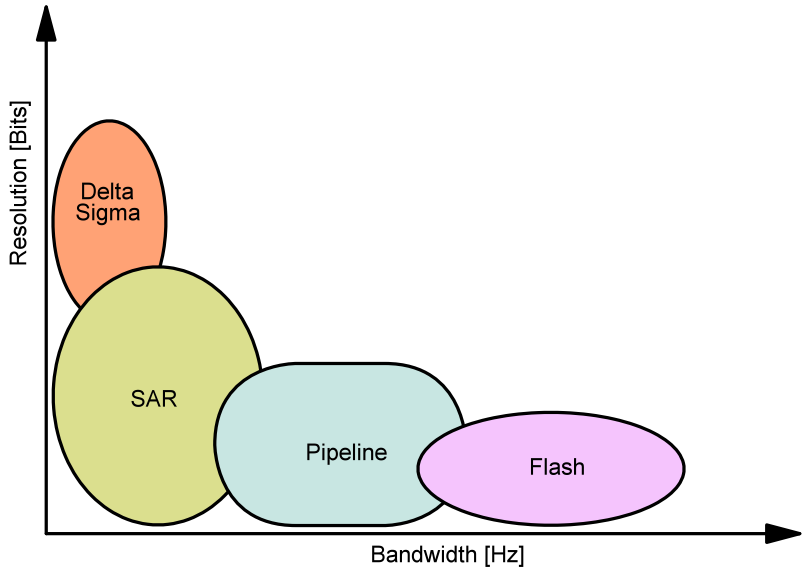

Figure 3-7: Resolution vs. bandwidth of most popular ADC architectures.

Successive Approximation Register architecture The SAR ADC is one of todays most widely utilized architectures for general purpose applications with medium resolution and low-to-medium sampling speed. The resolution of SAR ADCs typically is in the range of 8 to 18 bits, with a sample rate up to 5 MHz. A SAR architecture comprises modest circuit complexity, which in its most basic scheme employs a single comparator, a switched-capacitor network and some digital control logic as shown in Figure 3-8. This leads to the benefit of low power consumption for the conversion process. The basic operation of SAR is based on a binary search algorithm through all possible quantization levels before merging to a final digital code. The search algorithm operates by setting the N-bit register to midscale with the most-significant bit (MSB) set to a logic '1', which forces the DAC output voltage to be $\frac{V_{ref}}{2}$. The comparator checks if the DAC output value is greater then or less then the input voltage (V_{in}). In the case that $V_{in} > V_{DAC} = \frac{V_{ref}}{2}$, the comparator output will be '1' and the MSB holds the value '1'. If $V_{in} < V_{DAC} = \frac{V_{ref}}{2}$, then the comparator output will be '0' and the MSB of the N-bit register clears the '1' and becomes a '0'. The algorithm continues to the next bit down, forces that bit to a '1' and performs another comparison. This process continues till the last bit of the N-bit register. Once that LSB is reached, the conversion process is completed and the N-bit digital word is available in the register of the SAR logic [21].

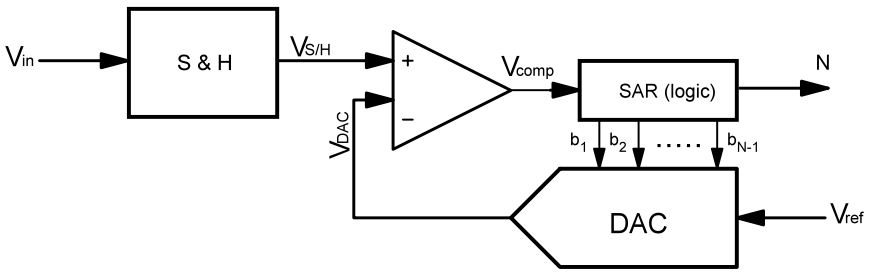

Figure 3-8: SAR ADC topology

Sigma-delta architecture In recent years, sigma-delta converters have gained a lot of popularity and are used for many applications that require a low-power, low bandwidth and high resolution. The big difference in the operating principle of ΣΔ A/D converters compared to SAR, is that ΣΔ converters rely on the oversampling principle. By extending the sample rate significantly beyond the Nyquist rate, the quantization noise power is spread over a larger frequency range and results in a lower amplitude over that range. This is defined by the Oversampling Ratio (OSR):

$$\text{OSR} = \frac{F_s}{2BW} \tag{3-25}$$

and is illustrated in Figure 3-9. With a technique called *noise-shaping*, the quantization noise

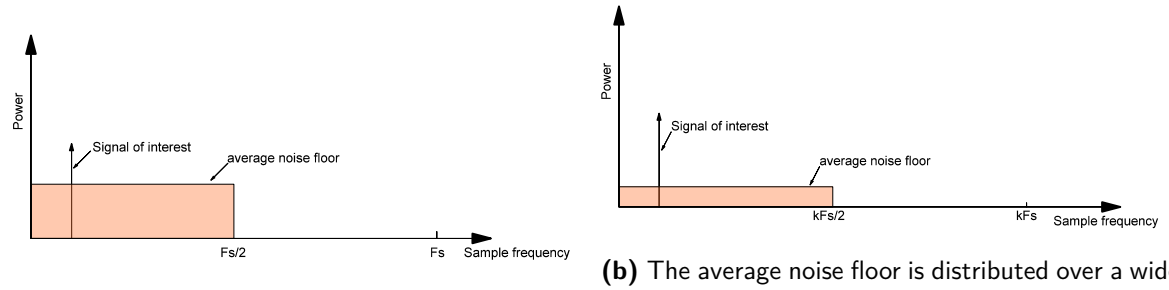

(a) Signal spectrum of a Nyquist A/D converter

(b) The average noise floor is distributed over a wider range of frequencies.

Figure 3-9: Signal spectrum of a A/D converter without oversampling (a) and with oversampling (b).

is placed in the high frequency range and this further reduces the noise inside the Nyquist rate. The noise shape is determined by the ΣΔ modulator order, a higher order results in lower in-band noise. A digital LPF is employed to filter out the high-frequency quantization noise and reduces the bandwidth to the Nyquist rate. The topology of a 1-bit ΣΔ is shown in Figure 3-10 [20].

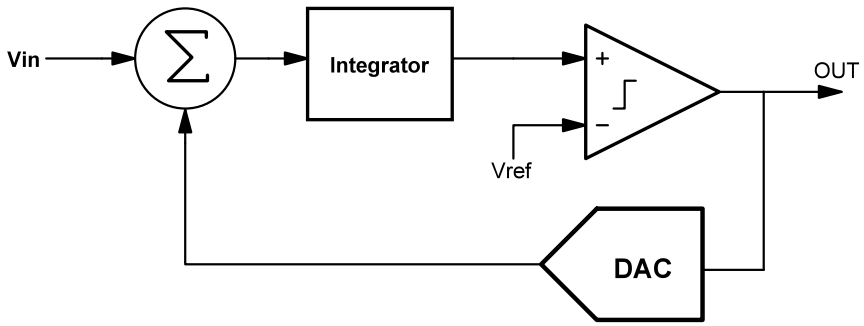

Figure 3-10: 1-bit ΣΔ ADC architecture.

Design consideration The previous two paragraphs discussed the SAR and sigma-delta ADC architecture. Regarding the choice for a suitable ADC, both have their advantages and drawbacks and these are given in Table 3-5. The A/D conversion block plays an important

	SAR	**Sigma delta**
Resolution (bits)	8-18	8-32
Max. Speed (Samples per second)	10M	1M
Advantages:	• Low power consumption	• High resolution
	• Easy to implement	• Inherently linear
	• High sampling speed	• Low cost
Drawbacks:	• Greater noise contribution	• Low sampling speed
	• Limited resolution	

Table 3-5: Comparison of SAR and Sigma-delta ADC.

role in the overall system and will be used to interface the receiver coil with the Lock-in Amplifier (LIA). The work of [23],[24],[25],[26] use A/D converters with resolution of 12-24 bit for a similar task. From Table 3-5 it can be observed that the SAR architecture can be used up to a resolution of 18 bit; higher resolutions can only be achieved with the sigma-delta architecture. In terms of sampling speed, SAR architecture has an advantage over sigma-delta architecture, but since the FDEM operating bandwidth is below the megahertz range both architectures can provide the required sampling speed. The power consumption of SAR architecture scales with the sampling speed, thus at a lower sampling speed the power consumption of SAR architectures is typically less than the sigma-delta architecture, where the power consumption mostly remains fixed. Since this work is still a Proof-of-Concept, less emphasis is placed on low-power design. Therefore, in this case both SAR and sigma-delta can be used up to 18 bits. For a more accurate representation of the analog signals, high resolutions in the range of 20 - 24 bits can only be achieved with a sigma-delta architecture, which requires a complex digital circuit to decimate and filter the oversampled signals. Hence, there is a trade-off between resolution and implementation. For a simpler implementation, a SAR architecture up to 18 bits can be used; for higher resolutions, a sigma-delta architecture with a more complex design process can be used. The minimum design specifications for the A/D converter are listed in Table 3-6.

Specification	**Value**
Architecture	Sigma-delta or SAR
Resolution	18 - 24 bits
Sample rate	$\geq 2 \times$ FDEM BW
Max. power consumption	-
Supply voltage	5 V

Table 3-6: Specifications for A/D block of the system.

3-5 Power Amplifier

Function To properly drive the transmitter coil, the signal from the D/A block needs to be amplified. A power amplifier increases the power of the input signal to the desired power level needed for the load that is connected to the output. There are several different Power Amplifier (PA) types available. To differentiate between the characteristics and performances of a PA, the term *class* is used. There are multiple ways and several architectures available to implement a PA class. A general survey limited to the classes A, B, AB, C and D will be presented [27],[28],[29],[30],[31],[32]. The purpose of this survey is to provide a basic understanding and not an in depth analysis of the circuit and architecture. Based on this survey, a PA will be chosen for implementation for the Proof-of-Concept.

3-5-1 Class A Amplifier

The class A power amplifier is the most basic power amplifier. In its simplest form, the architecture comprises one active device connected to a load. Figure 3-11 shows an example of a basic class A amplifier topology. In here, the transistor is biased such that it is always conducting current, which is at a 360° conduction angle, or a full duty cycle of the output waveform. The current flowing through the transistor needs to be at least as high as the maximum drive current needed for the output load. As a result, the class A amplifier has high linearity and low distortion, but it comes at cost of power dissipation.

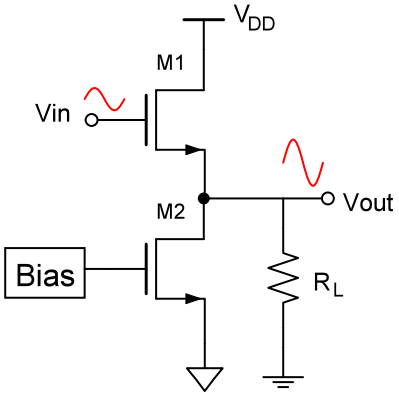

Figure 3-11: Basic circuit topology of an NMOS class A amplifier

The efficiency of a power amplifier is defined as how well the PA is able to transfer the power from the power source to the output stage and is given by:

$$\eta = \frac{P_L}{P_S} \times 100\% \tag{3-26}$$

where, P_S is the power drawn from the supply source:

$$P_S = V_{\text{supply}} I_{\text{supply}} = \frac{V_{\text{supply}}^2}{R_L} \tag{3-27}$$

and P_L is the average output power delivered to the load and given by:

$$P_L = \frac{V_{RMS}^2}{R_L} \tag{3-28}$$

For the Class A amplifier example of Figure 3-11, the maximum conversion efficiency is:

$$\eta = \frac{P_L}{P_S} \times 100\% = \frac{V_{DD}^2/2R_L}{V_{DD}^2/R_L} \times 100\% = 50\% \tag{3-29}$$

It should be noted that this is a theoretical value (assuming that $V_{RMS}(max) = \frac{V_{\text{supply}}}{\sqrt{2}}$), the practical efficiency is much lower and more around 30% due to power dissipation in other components and load.

3-5-2 Class B Amplifier

The most practical class B amplifiers employ a configuration with two complementary transistors. The transistors are biased such that each device conducts current 50% of the time, also known as a *push-pull* configuration. Since the amplifier is biased at a conduction angle of 180° it only draws current for a limited time, hence improving the power efficiency of the amplifier. Figure 3-12 shows a simplified class B amplifier circuit. The circuit behavior is such, that when the output stage is sourcing current to the load, the top transistor is on. When the output stage is sinking current from the load, the bottom transistor is on. Thus, there is an abrupt transition from the top transistor to the bottom transistor as the output current goes to zero. However, in practice the transition does not happen instantly. In the cross-over region, neither device is in a conducting state, which leads to crossover distortion in the output signal. Hence a trade-off is made between better efficiency in exchange of distortion. By using the same equation from equation (3-26), the maximum theoretical conversion

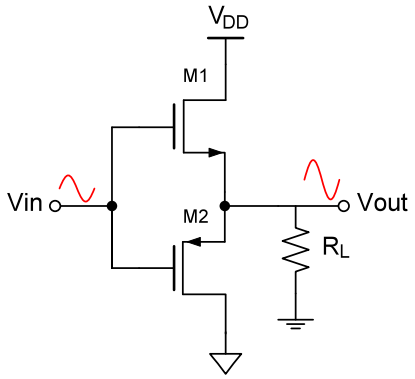

Figure 3-12: Basic circuit topology of a CMOS class B amplifier in a push-pull configuration

efficiency for the class B amplifier can be determined as:

$$\eta = \frac{P_L}{P_S} \times 100\% = \left(\frac{V_{DD}^2}{2R_L}\right) \Big/ \left(\frac{2V_{DD}^2}{\pi R_L}\right) = \frac{\pi}{4} \times 100\% = 78.5\% \tag{3-30}$$

which shows a significant improvement in efficiency compared to the class A amplifier. The practical efficiency though, is closer around 50%.

3-5-3 Class AB Amplifier

As the name suggests, the class AB amplifier is a combination of a class A and class B amplifier. Hence, the conduction angle of this type of amplifier is between 180° and 360°, depending on the operating point of the transistors. The circuit of a class AB amplifier can be seen as a variation of a class B push-pull configuration and is illustrated in Figure 3-13. In a class AB amplifier, both active devices are allowed to conduct at the same time. This overcomes the cross-over distortion issue from the class B amplifier and with a better efficiency than that of the class A amplifier. Thus, the class AB amplifier is a good compromise of the linearity of a class A and efficiency of a class B amplifier. Its efficiency depends on the

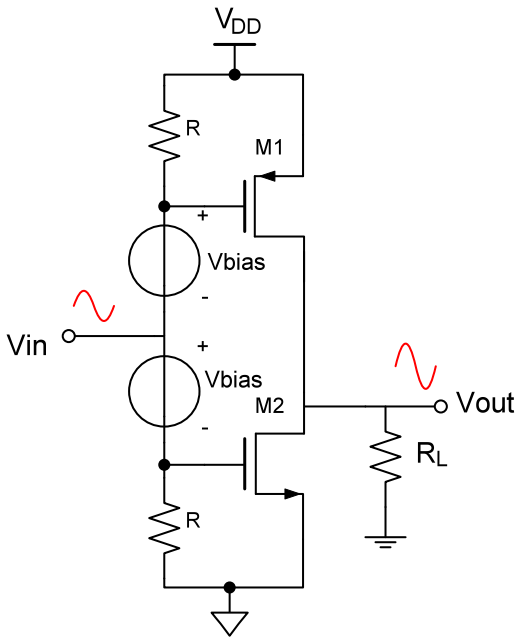

Figure 3-13: A CMOS class AB amplifier in a push-pull configuration. The diodes and resistors reduce cross-over distortion.

conduction angle and is between 50-78.5%. Practical class AB amplifier implementations have an efficiency around 40-60% .

3-5-4 Class C Amplifier

From the study of class A and class B amplifiers it becomes clear that reducing the conduction angle results in higher efficiency, but at the price of poor linearity. The circuit topology of a class C amplifier is essentially similar to that of a class A amplifier, comprising one transistor. By biasing the transistor such that its conduction angle is less than 180°, the transistor will operate as a class C amplifier. If the transistor is biased to reduce the conduction angle even further, the efficiency of a class C amplifier can approach 100%. Another trade-off that needs to be taken into account is the output power of the amplifier, which falls to zero since

there is no current flowing. To make up for this, the input driving power has to be increased significantly. In fact, class C amplifiers require the largest input driving power. Similar to the previous mentioned amplifiers, reducing the conduction angle significantly also introduces unwanted distortion at the output signal. Typically, the class C amplifier is configured as a tuned amplifier and finds its application in the RF field e.g. RF oscillator, FM transmitter. The maximum efficiency of a class C PA is given as:

$$\eta = \frac{\theta - \sin(\theta)}{4\sin(\frac{\theta}{2}) - \frac{\theta}{2}\cos(\frac{\theta}{2})} \times 100\% \tag{3-31}$$

from this relation it becomes clear, that as the conduction angle θ approaches zero, the efficiency increases to 100%. Figure 3-14 shows a class C RF PA. The LC-tank circuit is designed to resonate at the frequency of interest and additional filtering/matching is provided by the block connected at the load.

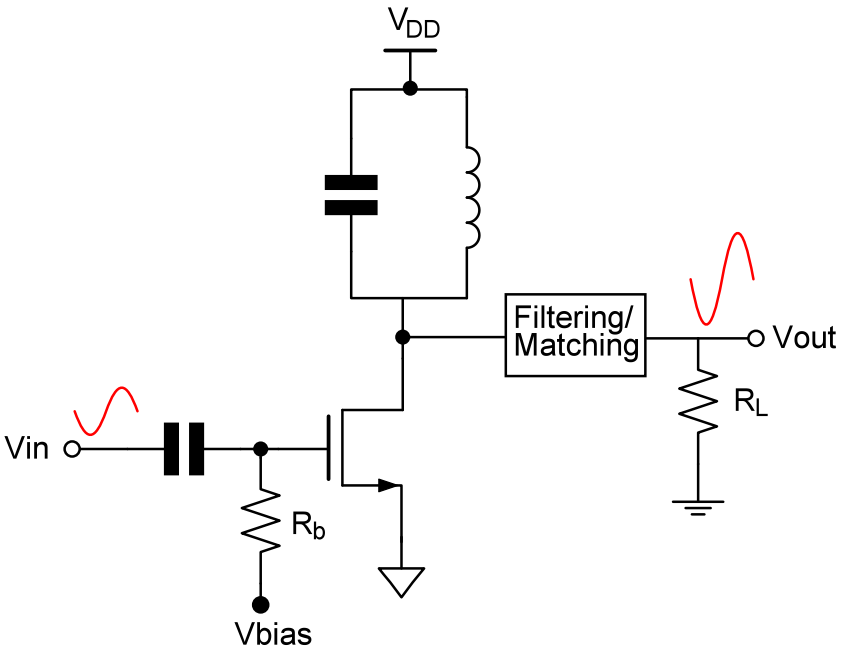

Figure 3-14: NMOS biased class C RF Power Amplifier circuit.

3-5-5 Class D Amplifier

The previous discussed power amplifiers comprises active devices biased such that their behavior acts as a controlled current source. This configuration provides linearity, but the efficiency of the amplifiers is limited to the biasing conditions. By operating the transistors as switches instead of current sources, the amplifier can achieve a theoretical efficiency of up to 100%. The reason behind this, is that an ideal switch has either zero current flowing through it or zero voltage across it. Therefore, the current-voltage product of an ideal switch is always zero,

as a result the transistor dissipates no power. The class D amplifier is based on this principle and a typical circuit topology is shown in Figure 3-15. The circuit comprises two MOSFET devices that are driven by a high frequency switching Pulse Width Modulator (PWM). The pair of transistors are never in a conducting state at the same time, as this would cause a short circuit between the power rails. One transistor takes care of the positive half-cycles and the other of the negative half-cycles of the input signal. This operation looks similar to the class B amplifier push-pull configuration, but the difference occurs that the transistors are driven as switches instead as current sources. Theoretically, the power conversion efficiency of class D amplifier is given as:

$$\eta = \frac{P_L}{P_S} \times 100\% = \left(\frac{V_{DD,max} I_{D,max}}{\frac{\pi V_{DD,max} I_{D,max}}{\pi}} \right) \times 100\% = 100\% \tag{3-32}$$

where, $I_{D,max} = \frac{VDD}{R}$. In reality the switching action of the MOSFET occurs by charging and discharging the drain capacitance, which dissipates power. The power dissipation is proportional to the switching frequency, hence a class D amplifier is generally limited to operation in low frequencies. Practical efficiencies of class D amplifiers are around 85-90%. A big advantage of the class D amplifier is its efficiency which outperforms the linear amplifier classes significantly. However, it is more susceptible to Electromagnetic interference (EMI) due to the rapid switching topology. Hence, proper care has to be taken to reduce EMI during the design of a class D amplifier.

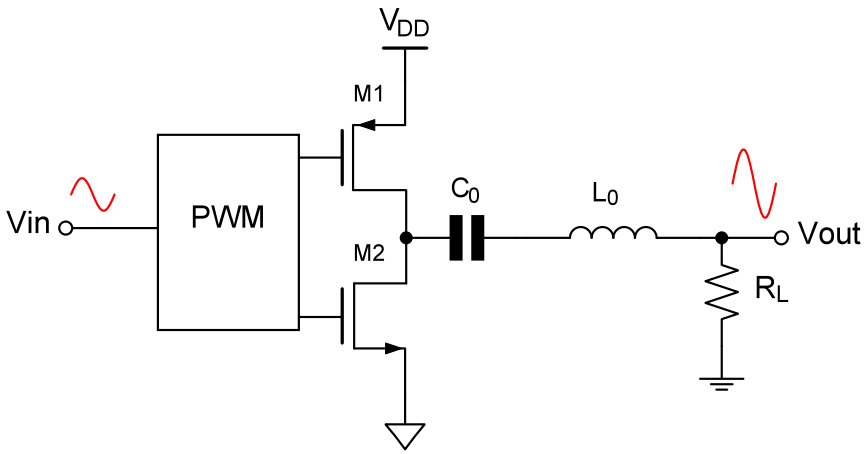

Figure 3-15: Class D amplifier circuit driven by by a PWM. The load network connected to the output is tuned to the fundamental frequency to select the wanted components.

3-5-6 Comparison of PAs

The previous subsections presented the basic topology and operation of some popular PAs. Each PA class presented, differ in their properties of conduction angle, power efficiency and linearity. In Table 3-7 an overview of the discussed PAs is given. From the table it can be observed that either class AB or class D would present itself as a suitable candidate in terms of efficiency and linearity. For this work a class D amplifier has been chosen as it provides the best efficiency with good linearity.

Class	Conduction angle	Theoretical efficiency	Practical efficiency	Linearity
A	2π	50 %	25%	+++
B	π	78.5%	50%	++
AB	$\pi - 2\pi$	50-78.5%	40-60%	+++
C	$0 - \pi$	100%	55%	+
D	π (on-off switching)	100%	85-90%	+++

Table 3-7: Comparison of the different PA classes. [+++ = good, ++ = moderate, + = poor]

3-6 Single-board Computer

Function The Single-board Computer (SBC) can be seen as the heart of the system and it has multiple important functions. Firstly, it generates and process the signals from the A/D and D/A block. This is done in the digital domain by utilizing a Lock-in Amplifier (LIA) which runs on the SBC. The second function is to interface and control a GPS module. Lastly, the SBC takes care of the user interface and how the system will operate. These functions could be implemented with a Microcontroller unit or FPGA, however a SBC provides several benefits over these options. One of the benefits of using a SBC is that it allows multiple functions to be implemented with one SBC unit, which aids in the development time. A Microcontroller is simple to use for basic functions, but for complex functions intensive development and programming is needed. Another big advantage of the SBC is that it has the most convenient I/O interfaces already equipped e.g. USB, ethernet, Wi-Fi without the need of installing drivers, which is the case with Microcontrollers. An FPGA is also capable of the signal processing tasks and interfacing with a GPS, however it requires experience with a *hardware description language* like VHDL or Verilog. Moreover, an FPGA development board costs significantly more than a SBC. Table 3-8 shows a comparison of a SBC, microcontroller and FPGA. In this work a SBC has been chosen due to its ability of performing complex processing task, design flexibility and its cost effectiveness.

	Single-board computer	Microcontroller unit	FPGA
Benefits	Ready-to-use board	Easy to employ for simple tasks	High speed and parallel processing
	Cost-effective	Low-cost option	Reconfigurable hardware
	Generally, no drivers needed for I/O interface		Many development and simulation tools
Drawbacks	More expensive than MCU	Limited functionality	Expensive development boards
	Consumes more power	Limited processing power and data storage	Requires experience with Hardware Description Language.
		Drivers are needed for I/O interface	Drivers are needed for I/O interface

Table 3-8: Single-board Computer vs Microcontroller unit vs FPGA.

3-7 Lock-in Amplifier

Function The Lock-in Amplifier (LIA) will further process the (weak) signals from the receiver coil in the digital domain. It does so by extracting the amplitude and phase of the signal of interest at a specific frequency, while suppressing noise levels at other frequencies. To be able to understand how the lock-in amplifier fulfills this function, its theory and operation will be discussed in the following subsection.

3-7-1 Principle of Operation

The Lock-in Amplifier is a type of amplifier employed to detect and measure very small AC signals in the presence of noise sources. It can measure signals in the range of a few nanovolts, thus making it a suitable application for recovering the signals from the receiver coil. The operation of a LIA is based on the demodulation of a modulated signal, also known as synchronous detection or phase sensitive detection. This technique singles out the component of interest at a specific reference frequency and phase. As a result, unwanted noise signal sources with a different frequency and phase relationship are rejected [33]. To further explain the operation, a typical block diagram of a LIA is illustrated in Figure 3-16. In here, a Phase Sensitive Detector (PSD) scheme is utilized where two signals with identical frequencies are multiplied with each other. V_{in} is the input signal and V_{ref} the reference signal. The product of these signals produces an output signal at the sum and at the difference of the frequency, which can also be seen as a DC-component and a sinusoidal component. This is the demodulation process and can be written as:

$$V_{in} = V_{in}\sin(\omega_{in}t + \theta_{in}) \tag{3-33}$$

$$V_{ref} = V_{ref}\sin(\omega_{ref}t + \theta_{ref}) \tag{3-34}$$

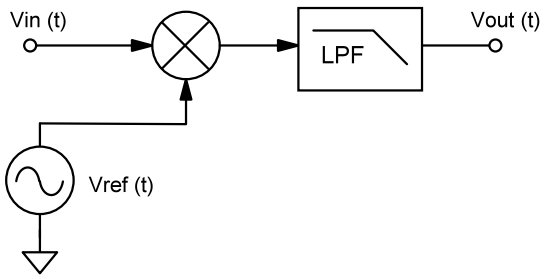

Figure 3-16: Simplified block diagram of a Lock-in Amplifier

taking the product of V_{in} and V_{ref} yields:

$$V_{out} = V_{sig}V_{ref}\sin(\omega_{in}t+\theta_{in})\sin(\omega_{ref}t+\theta_{ref}) \tag{3-35}$$

$$= \frac{V_{in}V_{ref}}{2}\cos[(\underbrace{\omega_{in}-\omega_{ref}}_{\text{difference frequency}})t+\theta] - \frac{V_{in}V_{ref}}{2}\cos[(\underbrace{\omega_{in}+\omega_{ref}}_{\text{sum frequency}})t+\theta] \tag{3-36}$$

where, $\theta = \theta_{in} - \theta_{ref}$. Assume $\omega = \omega_{in} = \omega_{ref}$, then equation (3-35) can be written as:

$$V_{out} = \underbrace{\frac{A_{in}A_{ref}}{2}\cos(\theta)}_{\text{DC-component}} - \underbrace{\frac{A_{in}A_{ref}}{2}\cos(2\omega t+\theta)}_{\text{sinusoidal component}} \tag{3-37}$$

Equation (3-35) makes use of the trig identity:

$$\sin(x)\sin(y) = \frac{1}{2}[\cos(x+y)-\cos(x-y)] \tag{3-38}$$

By passing the output signal through a low-pass filter with a narrow bandwidth, the sinusoidal component will be removed and only the DC-component will remain [34].

Dual Phase LIA In a dual phase architecture a second PSD is incorporated and fed with the same input signal as the first PSD, but multiplied with a reference signal that is $\frac{\pi}{2}(90°)$ shifted in phase. The output signal of the second PSD is again passed through a narrow bandwidth low-pass filter. The two reference signals are always orthogonal in phase to each other. The output of each PSD after low-pass filtering is given by:

$$X = V_{in}\cos(\theta) \tag{3-39}$$

$$Y = V_{in}\sin(\theta) \tag{3-40}$$

where, X is the output signal of the first PSD which operates on a cosine reference and is referred to as the in-phase signal. Y is the output signal of the second PSD, which operates on a sine wave reference and is referred as the quadrature signal. A dual phase architecture can greatly improve the detection accuracy of a LIA and determine the amplitude and phase difference of the input signal, independently of the reference signal. This avoids the error

by phase shift mismatch in a single phase LIA [24]. The magnitude $|A|$ and phase θ can be derived with the following equations:

$$|A| = \sqrt{X^2 + Y^2} \tag{3-41}$$

$$\theta = \arctan\left(\frac{Y}{X}\right) \tag{3-42}$$

The block diagram of a dual phase LIA architecture is given in Figure 3-17 .

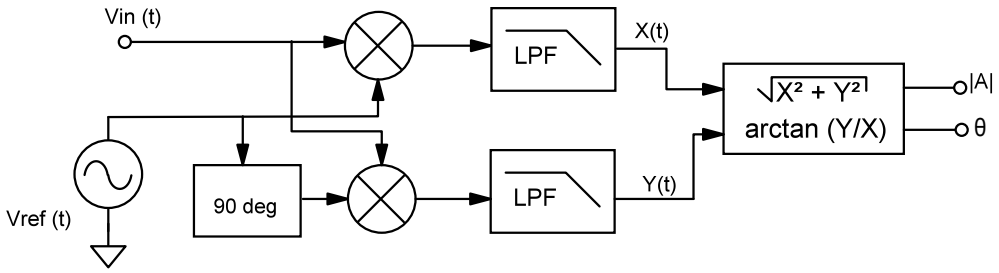

Figure 3-17: Block diagram of a dual Lock-in Amplifier

Design consideration There are multiple approaches to implement a Lock-in Amplifier (LIA), this is mainly determined by its application and filter requirements. The implementation can be done in the analog domain, digital domain or in a mixed-signal domain, where the implementation is done in both analog and the digital domain. In the analog domain the LIA comprises op-amps, analog filters and passive components. In the digital domain most of the processing is done using software and dedicated Digital Signal Processing hardware like a microcontrollor or FPGA. To read in the input signal, an A/D conversion is needed. In the mixed-signal domain, the LIA scheme is made up of an analog stage which can consist out of low-noise amplifiers, high-precision instrument amplifiers or programmable-gain amplifiers. Their purpose is to ensure proper signal conditioning for A/D conversion. Once the signal is digitized by the ADC, further signal processing takes place in the digital domain by the DSP and software. The signal recovery performance of a LIA is described by its *Dynamic Reserve*, which measures how large an interfering signal can be, before the LIA starts to measure the signal of interest incorrectly. The dynamic reserve is given by:

$$\text{Dynamic Reserve (dB)} = 20 \times \log\left(\frac{\text{Noise signal}}{\text{Input signal}}\right) \tag{3-43}$$

The Dynamic Reserve, is restricted to the range of linear operation of the input amplifier. Meaning, that the maximum Dynamic Reserve is not available at all sensitivity settings e.g. 60 dB Dynamic Range is not available at 1 V full-scale sensitivity settings, as this would imply a 1 kV input capability. Although the name implies similarities, the Dynamic Reserve should not be confused with *Dynamic Range*, which is the ratio of maximum peak signal and minimum detectable signal. It has been reported that a typical analog LIA has a Dynamic Reserve of 60 dB, while a digital LIA achieves a Dynamic Reserve of ∼80-100 dB. In recent years, digital LIA have become more popular than analog LIA. Table 3-9 summarizes a comparison between digital LIA and analog LIA [23],[34],[24].

Digital LIA	Analog LIA
• Flexible development and configuration	• Complex analog circuits are required for the same performance
• Requires less components for implementation, making it more compact	• In general takes up more area due to complex circuit
• No distortion issues due to low-harmonic content (-120 dB)	• Suffers from distortion issues, if the reference is not low-harmonic
• No deviations in phase and gain, as the PSD takes place in the digital domain	• Can exhibit non-linearity due to temperature and off-set drifts
• Higher Dynamic Reserve (∼100 dB)	• Limited Dynamic Reserve (∼60 dB)
• Better price/performance ratio	• Needs expensive high-precision components, which increases the cost of design

Table 3-9: Digital LIA vs. Analog LIA

From the comparison of Table 3-9 it becomes clear that the digital LIA outperforms its analog counterpart in many aspects (cost, area, linearity, Dynamic Reserve). Mainly due to its flexible development and configuration properties, a digital LIA has been chosen for the proposed concept in this work. This provides a high speed-to-development and testing time and the option to develop multiple LIA in the digital domain. In the next chapter the implementation of the digital Lock-in Amplifier is elaborated in detail.

3-8 GPS

Function The Lock-in Amplifier is the final block that processes the measured signals before it will be stored as data. However, the data set lacks geolocation information that is important if an area proves to be interesting for further exploration and needs to be back traced. The GPS block fulfills this gap in the data and logs location information and a time stamp. The data will be merged with the measurement data once a survey is finished. Another function of the GPS block is to provide the date and time for the RPi by synchronizing the system clock with the GPS clock. The measured signals have a time stamp from the system clock and by synchronizing the system clock with the GPS clock, the corresponding location can be linked with its measured signal by their time stamp.

3-9 Summary

In this chapter the system architecture for the FDEM survey instrument has been proposed. The architecture is presented in a block diagram in Figure 3-2 and the functionality of each block has been discussed. A simple model for the coil configuration was given and it was concluded that by increasing the number of turns and diameter of the coil, the generated voltage in the receiver coil will be increased.

This was followed by a discussion of the Low-noise amplifier block, which plays an important role of amplifying the generated receiver coil voltage to the desired voltage level of the A/D

converter input. The key parameter of the LNA is the noise parameter that cannot exceed the voltage level of the receiver coil.

For digital data acquisition, the A/D converter block translates the time-continuous signal from the LNA, to a digital code that will be further processed by the digital Lock-in Amplifier. It was concluded that an ADC with a SAR or $\Sigma\Delta$ architecture, a resolution of 18-24 bits and a sample rate of at least twice the FDEM bandwidth is a good fit for the A/D conversion block. To properly drive the transmitter coil, a Power Amplifier is employed.

A basic study of the architectures of class A, B, AB, C and D PA has been given and from the comparison of Table 3-7 it was concluded that a class D amplifier can be employed to properly drive the transmitter coil.

The principle of operation of a LIA has been explained and an overview of a digital and analog LIA was given. Due to its flexible development and configuration options, a digital LIA has been chosen in this work. The digitized signals from the A/D converter are processed by the LIA block and will be implemented on a Single-board Computer (SBC). In addition to operating a digital LIA application, the SBC is utilized for the user interface of the FDEM system, data storage and GPS interface.

From the discussion of the system architecture and its individual blocks it was shown that the proposed Proof-of-Concept concedes with the minimum requirements and proves to be feasible for further development. The implementation of the proposed architecture will be discussed in detail in the next chapter.

Chapter 4

Implementation

In the previous chapter a system architecture was proposed to develop a FDEM measurement system. The most important design decisions and implementation details are discussed in this chapter. The first section outlines the design and implementation order. Which is followed by the implementation of the various blocks of the architecture shown in Figure 3-2. The chapter concludes with a summary of the implemented architecture and important achieved specifications.

4-1 Design and Implementation Procedure

The proposed architecture of chapter 3 comprises several blocks of different disciplines. A complete custom design of this architecture would expand the design time significantly. Hence, to speed up the development time several blocks were implemented by off the shelf circuit boards, as will be explained in the following sections and subsections of this chapter. The system design and implementation was done in the following order:

1. Single-board computer
2. A/D and D/A converters
3. Digital LIA
4. Coil redesign
5. LNA
6. Power amplifier
7. GPS

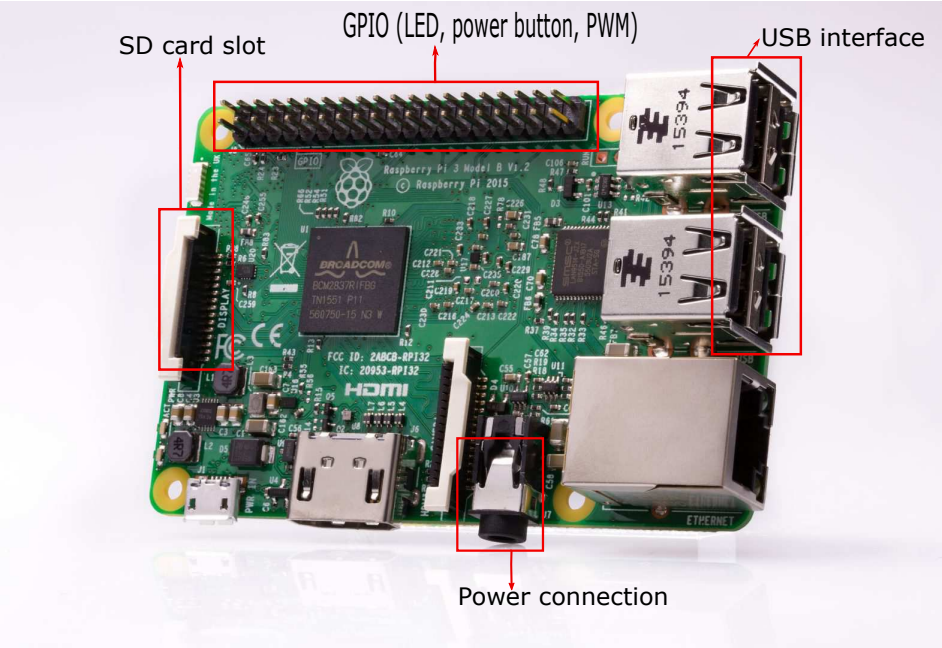

Figure 4-1: Raspberry Pi 3B circuit board. The interfaces that are used for the prototype are indicated in red.[3]

The SBC was implemented first, as it operates the complete system and the digital Lock-in Amplifier will be implemented on the SBC. The A/D and D/A converter blocks are an integral part of the digital LIA, so these were chosen as the second step in the implementation procedure. The design and implementation of the LIA was realized as the next step. The initial coils were provided by SkyDowser and were used in the work of [5]. However, it was found that these coils did not generate the desired voltage levels, hence a redesign of the coils was done before starting with the analog circuit design of the LNA. This was followed by the implementation of the GPS and lastly, the Power amplifier. The following sections details the design of this procedure.

4-2 Raspberry Pi 3B

The SBC was implemented by a Raspberry Pi 3B. The RPi is a widely utilized SBC and was selected primarily for its compatibility with the MATLAB Simulink design tool, which was used to design and implement the digital LIA. Additional benefits of employing a RPi 3B were - its RAM of 1 GB, central processing unit of 1.2 GHz, enough customizable GPIO ports, four USB ports and wireless network support -, which meets all the requirements of the SBC given in section 3-6. Figure 4-1 shows the Raspberry Pi 3B circuit board.

4-3 Coil Redesign

For the implementation of the transmitter, receiver and bucking coil there were already coils provided by SkyDowser. The properties of these coils were given in Table 3-1. It was found

that the voltage generated in the receiver coil would be hard to detect with the current receiver coil. Thus, the receiver coil was redesigned to generate a higher voltage. As discussed in section 3-2 of the previous chapter, the generated voltage is related to the number of turns and the area of the coil. Moreover, the mutual inductance with the conductor and the conductor parameters also determine the voltage that can be generated. Another important aspect that had to be kept in mind during the redesign of the coil, was the wire thickness of the coil. There is a trade-off between the weight and resistance of the coil, which is displayed in Figure 4-2. By reducing the wire thickness, the weight of the coil decreases, but the DC resistance of the wire increases. An increasing resistance leads to an increasing thermal noise contribution, which is highly undesired. Hence a proper selection of the wire diameter is necessary for the implementation of the receiver coil. The diameter of the coil was increased to 20 cm and the number of windings to 1000, which would require a total wire length of 628 m. Table 4-1 summarizes the receiver coil trade-offs between the resistance, thermal noise contribution and weight. The final parameters for the receiver coil are given in Table 4-2.

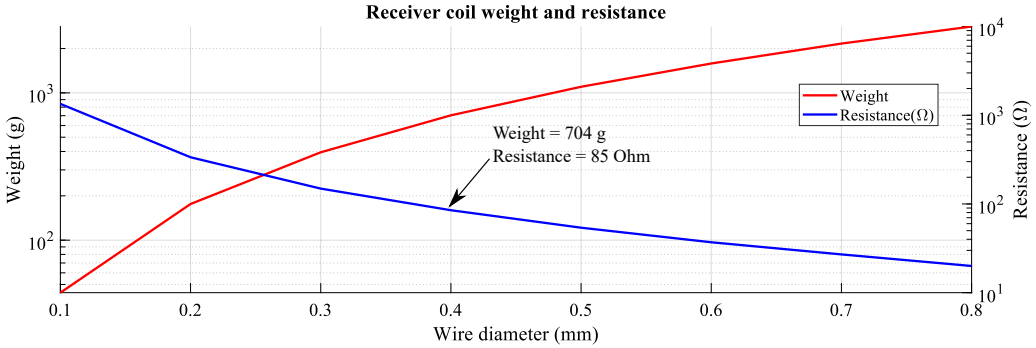

Figure 4-2: Resistance vs. weight trade-off for the wire diameter of the receiver coil for a wire length of 628 m.

Wire diameter (mm)	Weight (gram)	Resistance (Ω)	Thermal noise($nV/\sqrt{Hz}$)
0.1	43	1343	5.46
0.2	176	336	3.52
0.3	395	149	3.04
0.4	704	85	2.86
0.5	1100	54	2.75
0.6	1583	37	2.70

Table 4-1: Trade-off between wire diameter, weight, resistance and thermal noise contribution for a wire length of 628 m.

The constraint by the specifications of Table 1-1 that applies to the receiver coil is primarily the weight, which increases with an increasing wire diameter. As can be seen from Table 4-1, a wire diameter of 0.4 mm was found to be an acceptable choice to balance the trade-off between the weight and thermal noise contribution of the receiver coil. The receiver coil was realized by manually winding 628 meter of copper wire around a plastic coil body; the coil body was fabricated by a 3D printer. The winding setup and the coil body are shown in Figure 4-3. It is expected with the model of section 3-2, that a voltage of around 25 μV will be generated in the receiver coil and this value was used as a reference for the input signal of

the LNA.

(a) Set-up utilized for manually winding the coil with the use of a power drill

(b) The plastic body around which the receiver coil was wound.

Figure 4-3: Winding of the receiver coil

Parameters	Value
Windings	1000
Inductance	27.1 mH
Diameter	20 cm
DC Resistance	85 Ω
Wire diameter	0.4 mm
Weight	704 grams

Table 4-2: Parameters of the receiver coil utilized in this work.

4-4 Digital Lock-in Amplifier

As proposed in Section 3-7, a digital LIA was utilized in this work. The A/D and D/A converter were an integral part of the design of the LIA, hence the implementation of the data converters was done in parallel to the LIA.

4-4-1 USB Sound Card

A specific designed A/D and D/A converter would provide optimum values for the design parameters discussed in section 3-4, however this would extend the development time of the measurement instrument. As the focus of this thesis was on the Proof-of-Concept for the

complete FDEM measurement system, the design trade-off was made to employ an external sound card for both the A/D and D/A conversion tasks with good enough results that meet the key specifications of Table 1-1. Another advantage of employing a sound card is that it could be connected directly with the RPi through its USB port. In this work two USB sounds cards were tested for the implementation of the data conversion blocks of Figure 3-2:

(a) Plugable USB audio adapter

(b) Sweex SC016 USB sound card

Plugable USB audio adapter This USB sound card was chosen on account of its 16-bit resolution, sample rate of 48.000 Hz and compact design dimensions [35]. The sample rate does not cover the full bandwidth as specified in Table 1-1, however it can still be utilized for the Proof-of-Concept. Further, the resolution satisfies the specification as given in Table 3-6. Figure 4-4 shows the compact design of the Plugable USB audio adapter, which is beneficial for the dimensions and weight of the prototype. In spite of meeting the specifications and being advertised as a good fit for development boards, this sound card proved not to be suitable for this work. The problem arose with the microphone input port that was not able to convert the signal into a digital code that could be used by the digital Lock-in Amplifier. During the test of the digital LIA, the signal into the microphone port was was fed through a TRS cable. The signal from the LIA was coming in on the tip of the connector, whereas the Plugable audio sound adapter was reading the signal from the Ring of the connector, thus this sound card could not be utilized in this work. The tip, ring and sleeve are can be seen in Figure 4-4b.

Sweex SC016 USB sound card This USB sound card was immediately available to be employed during the design and implementation of the digital LIA, hence it was chosen as the successor of the Plugable USB audio adapter. The Sweex SC016 utilizes the CM6206 chip from C-media. This chip has a 16-bit audio resolution and a maximum sample frequency of 48.000 kHz. This sample rate was found to be good enough to cover a subrange of the FDEM bandwidth. The power rating of the device is 5V, with a maximum current of 0.5A. This device is powered by the RPi USB port and connected with a USB A-B cable. There are multiple input and output connections to the device, however in this application the *headphones* and the left-channel of the *microphone* port are used as shown in Figure 4-5. A complete overview of the connections can be found in the manual [36]. The microphone port functions as the input port and does the A/D conversion to bring the signal in the digital domain for further signal processing. The headphones port will do the D/A conversion task to drive the class D amplifier. As no specific input voltage levels are provided by the datasheet of the Sweex SC016, it has been assumed that the microphone input has a typical microphone input voltage level, which is between 10 mV - 500 mV. The headphone connection provides enough voltage output to control the class D amplifier. Table 4-3 lists the specifications of the Sweex SC016.

(a) Front view of Plugable USB audio adapter.

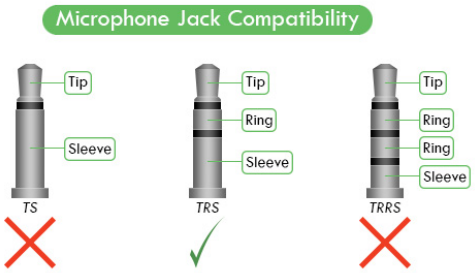

(b) Microphone Jack compatibility [35].

Figure 4-4: Plugable USB audio adapter

Figure 4-5: Front view of the Sweex SC016 16-bit sound card. The headphones connection (indicated by the red rectangle) is the output port that will be connected with the class D amplifier. The side of the sound card (not visible in this picture) contains the microphone port.

4-4-2 Dual phase digital LIA implementation

The implementation and digital circuit design of the dual-phase LIA was done in Simulink tool. By configuring the hardware target board in Simulink for a Raspberry Pi 3B, a customized version of the Raspbian operating system, which is generated by Simulink could be deployed to the RPi 3B. This enabled various design blocks in Simulink that could be utilized for the development of the LIA for the RPi 3B. The complete digital circuitry that is designed in

Table 4-3: Sweex SC016 specifications

Parameter	Value	Remark
Power	5V	The sound card will be powered directly by the USB port of the RPi
Max. current	0.5 A	-
Sample frequency	0 - 48.000 Hz	-
Audio resolution	16 bit	-
Headphones output	0 - 3V	The output voltage is tunable by the volume control. It provides sufficient voltage to drive the Class D amplifier
Microphone input	10 - 100 mV	No specific values are given. These are typical values.

Simulink is shown in Figure 4-6.

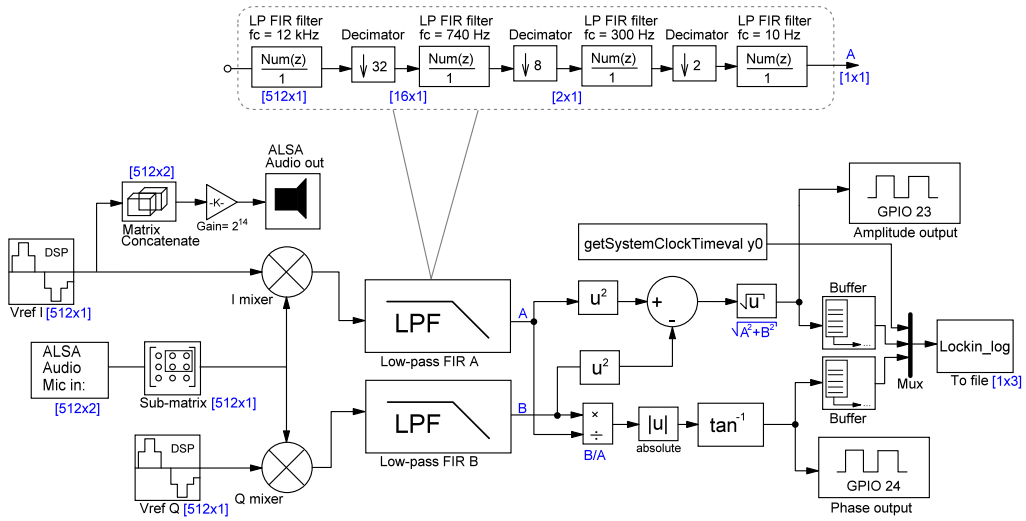

Figure 4-6: Schematic of the digital dual phase LIA

Signal generation and multiplication The input signal of the LIA is coming from the ALSA audio capture block. This block reads audio data from the Sweex SC016 usb sound card and outputs a [512x2] data block. The first value of the block is the number of samples per frame and the second value is the number of channels of the audio device. The audio sampling frequency of this block equals the sampling frequency of the Sweex SC016, which is 48.000 Hz. The DSP sinewave blocks were used to generate the reference signals and need to be specified for frequency, phase offset, sample time and samples per frame. For this application the sample time was limited to the sample rate of the Sweex SC016, thus the sample time was chosen as 1/48.000 with 512 samples per frame. Vref I was set as the in-phase reference signal and Vref Q as the quadrature reference signal (sinewave with a $\frac{\pi}{2}$ phase shift). Since the

signal generation is done in the digital domain the reference signals are discrete and described as:

$$V_{ref}\ I[n] = sin[\omega nT + \theta_r] \quad (4\text{-}1)$$

$$V_{ref}\ Q[n] = sin[\omega nT + \frac{\pi}{2}] \quad (4\text{-}2)$$

The reference signals are generated by a [512x1] block, this data block needs to be of the same dimension in order to mix the reference signal with the measured signal. Hence, the sub-matrix block is employed to select only one column of the data block, which results in a [512x1] data block. The Vref I signal is fed to the ALSA audio out block, which sends the audio data to the headphones output port of the Sweex SC016. However, this output port requires a 2-channel audio signal. Hence, the matrix concatenate block first replicates the audio signal so that a datablock of [512x2] can be send towards the headphones port. The signal is amplified with $2^{14} = 16384$ to increase the dynamic range and drive a proper signal to the headphone port. The multiplication of the measured signal with the reference signal is done by the I mixer and Q mixer blocks.

Filtering and decimation In order to retrieve the DC-components from the demodulated signals, two Low-pass filter (LPF) are employed in the circuit of Figure 4-6. The LPF connected with the I mixer filters the in-phase signal A, whereas the LPF connected with the Q mixer retrieves the quadrature signal B. As described earlier in section 3-7, the LPF needs a narrow bandwidth to reduce noise. Both LPF are identical in their design and comprises of four cascaded FIR-filters and three decimators to achieve a bandwidth of 10 Hz. A narrow bandwidth filter has a long impulse response, which results in high amount of RAM required for the implementation. Hence, in order to reduce the computational load and amount of required RAM, the LPF is implemented with a multistage decimator approach. The idea behind this DSP technique is to reduce the overall number of computations, by distributing the LPF requirements over multiple filters. The decimation factor is given as:

$$D = \frac{F_s}{F_{sK}} = \prod_{i=1}^{K} D_i \quad (4\text{-}3)$$

To avoid aliasing, a LPF is needed before the decimator with a stop-band frequency of:

$$\omega_{max} = \frac{\pi}{D} \quad (4\text{-}4)$$

where, D is the decimation factor and ω_{max} is the maximum frequency after decimating. This can also be stated as:

$$F_{max} = \frac{F_s}{2D} \quad (4\text{-}5)$$

where, F_s is the sample rate before decimating and F_{max} the sample rate after decimating [37]. In this design the overall decimation factor D = 512 is divided over three stages. The first stage has a decimation factor D = 32 and the LPF stopband frequency is chosen as $F_s/4 = 12.000$ Hz. After the first stage there are $\frac{512}{32} = 16$ samples left and the sample rate is reduced to $\frac{48.000}{32} = 1500$ Hz. The second stage decimates with a factor D = 2 and the LPF has a stopband frequency of 740 Hz to prevent aliasing. The final decimator stage down samples with D = 8 and is preceded by a LPF with a stopband frequency of 80 Hz. This

signal can now be passed to the final LPF, which has a stopband frequency of 10 Hz and a sample rate of 93.75 Hz. The FIR low-pass filters were designed with the *FDAdesign* block in Simulink and the design parameters of the FIR filters are given in Table 4-4.

	LPF 1	LPF 2	LPF 3	LPF 4
Decimation factor D	-	32	2	8
Sample rate (Hz)	48.000	$\frac{48.000}{D} = 1500$	$\frac{1500}{D} = 750$	$\frac{750}{D} = 93.75$
Stopband frequency (Hz)	12.000	740	300	10
Stopband attenuation (dB)	80	80	80	80
Passband ripple (dB)	0.001	0.001	0.001	0.001
Filter order	22	14	11	51
Window method	Kaiser	Kaiser	Kaiser	Kaiser

Table 4-4: Design parameters of the FIR filters

If the signal of interest would be filtered directly by a FIR LPF with the same design parameters and a stopband frequency of 10 Hz, a filter with a order of 25693 would be required. This would increase the computational load significantly and is much higher than the order of the filters of Table 4-4. The FIR filter method has been chosen over the IIR filter method, as they are inherently more stable. The Kaiser window method obtains a smoother gain characteristic with less ripple and is a widely used method in practice [38]. After the signal is decimating and filtered, only the DC-component of the modulated signals remains and are given as A[1x1] and B [1x1].

Final signal processing The low-pass filters yield the signals A and B. These signals are further processed to determine the amplitude and the phase of the measured signal. The amplitude equation (3-41) is implemented by the blocks u^2 and square root block. The phase of the signal, which was given by equation (3-42) is implemented by the divider block that gives the fraction $\frac{B}{A}$. The block |u| then takes the absolute value of the fraction and the block $tan^{-}1$ yield the phase of the signal. The GPIO Amplitude and GPIO phase block sends out the signal to GPIO pin 23 and 24. These pins then output the amplitude and phase signal, which can be used to measure the value by an external device or to drive the bucking coil. **(discuss)**.

Simulink limitations It was desired to save the amplitude and phase of the measured signal directly in a .CSV file, which can be analyzed after an EM survey is completed. However, due to the limitations of Simulink that option was not available. Another limitation of Simulink, was that it had no direct support for the GPS module that is connected to the RPi. As a result the GPS coordinates could not be included as data in the lock-in amplifier application.

To address the first issue, the data is stored as a .MAT file. This type of file can only be read and processed within the MATLAB environment. From there it is possible to copy the data in a spreadsheet program and save it as a .CSV file. This is realized by the *lockin_log* to file block. To make use of this block, the *unbuffer* blocks are needed. The Mux collects the data samples in one file. To address the second issue, the getSystemClockTimeval block is used. This block reads the RPi 3B system clock, thus a time stamp can be added to the

data. Since the system clock will be synchronized with the GPS clock, the GPS coordinate will correspond with a measured data point by its time stamp. The time stamp format is UNIX EPOCH, which is an approximation of the number of seconds passed since 00:00:00 GMT, January 1 1970 or the value 0 of the UNIX date and time stamp. This is a rather unconventional format to read the time and date, but could easily be converted by an online EPOCH converter [39] to conventional date and time stamps.

Furthermore, it was not possible to perform a multi-frequency measurement. This limits the application to measure with a single operating frequency at a time. This feature is not beneficial for the time duration of an EM survey, as an area needs to be measured multiple times in order to measure at different operating frequencies. The operating frequencies are limited to the first LPF stopband frequency of 12.000 Hz.

Lastly, the LIA could only save one measurement after a survey was stopped. If a new survey would be started again, the LIA would overwrite the previous measurement with the same file name. This required the presence of laptop during a survey, so that the MAT-file can be transferred to the laptop before a new survey would commence.

Part number	Manufacturer	GBWP	e_n	i_n	RMS noise
OPA228 [40]	Texas Instruments	33 MHz	3.3 nV/$\sqrt{\text{Hz}}$	400 fA/$\sqrt{\text{Hz}}$	594 nV_{RMS}
OPA827 [41]	Texas Instruments	22 MHz	4.0 nV/$\sqrt{\text{Hz}}$	2.2 fA/$\sqrt{\text{Hz}}$	705 nV_{RMS}
OPA209 [42]	Texas Instruments	18 MHz	2.2 nV/$\sqrt{\text{Hz}}$	500 fA/$\sqrt{\text{Hz}}$	426 nV_{RMS}
OPA2300 [43]	Texas Instruments	150 MHz	3.0 nV/$\sqrt{\text{Hz}}$	1 fA/$\sqrt{\text{Hz}}$	547 nV_{RMS}

Table 4-5: Comparison of commercial op-amp ICs

4-5 LNA Circuit

This section details the design and implementation of the LNA. The noise parameter was the key design parameter, during the design of the LNA. As described earlier in section 3-3, the intrinsic noise contribution of the amplifier should not deteriorate the receiver coil signal, which is about 25 μV. The gain of the amplifier should be at least $\sim$74 dB in order to drive the Sweex SC016 microphone input port. The bandwidth was limited to 100 - 18 kHz, because the LIA can only process signals up to 12 kHz and frequencies below 100 Hz are not of interest. Limiting the bandwidth to 18 kHz has a positive effect on the power consumption and broadband noise contribution of the amplifier, as both are proportional to the bandwidth. To select a proper LNA that can meet these specifications, a quick comparison of available commercial op-amps with low-noise input sources was made. The op-amps that were reviewed are listed in Table 4-5.

It is evident from Table 4-5 that the Texas Instruments OPA0209 IC has the lowest input referred noise contribution, hence this IC was selected for the implementation of the LNA. The OPA209 was implemented as a three-stage cascaded circuit topology that is depicted in Figure 4-7. The three-stage topology was chosen because that allowed the gain and noise requirements to be met separately. The first stage was optimized for high gain and low noise, because the noise of this stage ultimately dominates the total noise contribution of the circuit. The second and third stage provide the additional necessary gain to drive the Sweex SC016 microphone input.

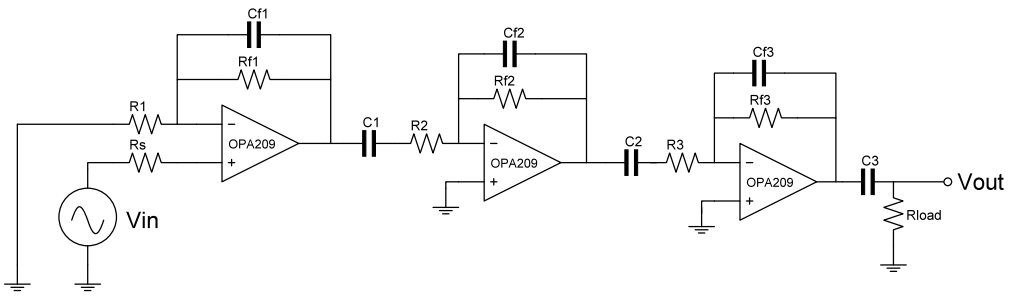

Figure 4-7: Schematic of the three-stage OPA209 in cascaded configuration

Implementation The circuit of Figure 4-7 was implemented on a perfboard, as this allowed a rapid implementation of the circuit. A preventive measure was taken to protect the circuit from potential electromagnetic interference by shielding the perfboard by a metal enclosure.

4-5-1 Gain Derivation

The OPA209 amplifier of the first stage was connected in a non-inverting configuration. The closed-loop gain of this stage is determined by the resistor feedback network of R1 and Rf1 and is given as:

$$A_{\text{cl1}} = 1 + \frac{\text{Rf1}}{\text{R1}} \tag{4-6}$$

The second and third stage employ an inverting configuration, where the closed-loop gain for the second stage is determined by the feedback resistor network of R_{f2} and R2. For the third stage the closed-loop gain is determined by resistors R_{f3} and R3. The closed-loop gain of the second and third stage can be described as:

$$A_{\text{cl2}} = -\frac{R_{\text{f2}}}{R_2} \tag{4-7}$$

$$A_{\text{cl3}} = -\frac{R_{\text{f3}}}{R_3} \tag{4-8}$$

As given by equation (3-12), there is a trade-off between the closed-loop gain and the bandwidth that needs to be considered. By carefully analyzing and selecting the components for the feedback network an optimum was found between gain, bandwidth and noise contribution. Table 4-6 presents the values of the implemented resistors, derived closed-loop gain and GBWP of each stage. From Table 4-6 it becomes clear that the required gain for each stage can be provided over the specified bandwidth of 100 - 18.000 Hz.

First stage	**Second stage**	**Third stage**
$R_1 = 100\ \Omega$	$R_1 = 5.1\ \text{k}\Omega$	$R_3 = 5.1\ \text{k}\Omega$
$R_{f1} = 3.3\ \text{k}\Omega$	$R_{\text{f2}} = 82\ \text{k}\Omega$	$R_{\text{f3}} = 51\ \text{k}\Omega$
A_{cl1}= 30 dB	$A_{\text{cl2}} = 24$ dB	$A_{\text{cl3}} = 20$ dB
$\text{BW}_{\text{cl1}} = 562.5$ kHz	$\text{BW}_{\text{cl2}} = 1.125$ MHz	$\text{BW}_{\text{cl3}} = 1.8$ MHz

Table 4-6: Closed-loop gain and GBWP design parameters.

4-5-2 Bandwidth

In order to achieve the specified bandwidth, feedback capacitors and coupling capacitors are utilized. The feedback capacitor is connected in parallel with the feedback resistor and determines the upper limit of the bandwidth, which is at the cut-off frequency of 18 kHz. The coupling capacitors are connected in series with the resistor (R2,R3) that is connected to the inverting input terminal of the OPA209, to implement the high-pass cut-off frequency of 100 Hz. The capacitor value is determined by:

$$\text{C} = \frac{1}{2\pi R \text{f}_{\text{c}}} \tag{4-9}$$

To obtain the same cut-off frequency for the second and third stage, the coefficient α_n [44] is needed. This coefficient is expressed as:

$$\alpha_n = \sqrt{2^{\frac{1}{n}} - 1} \tag{4-10}$$

van The partial low-pass cut-off frequency for each stage needs to be $1/\alpha_n$ higher than the low-pass cut-off frequency of the overall circuit. The coefficient for the first stage remains the same. The coefficients for the second and third stage are:

$$\begin{aligned} \alpha_2 &= \sqrt{2^{\frac{1}{2}} - 1} \\ &= 0.64 \end{aligned} \tag{4-11}$$

$$\begin{aligned} \alpha_3 &= \sqrt{2^{\frac{1}{3}} - 1} \\ &= 0.51 \end{aligned} \tag{4-12}$$

The partial low-pass cut-off frequencies can then be determined as:

$$\begin{aligned} \text{LP } f_{c1} &= 18\text{kHz} \cdot \frac{1}{\alpha_1} \\ &= 18\text{kHz} \end{aligned} \qquad \begin{aligned} \text{LP } f_{c2} &= 18\text{kHz} \cdot \frac{1}{\alpha_2} \\ &= 28.1\text{kHz} \end{aligned} \qquad \begin{aligned} \text{LP } f_{c3} &= 100\text{Hz} \cdot \frac{1}{\alpha_3} \\ &= 35.3\text{kHz} \end{aligned} \tag{4-13}$$

A similar process is done for the coupling capacitors of the second and third stage. Except in this case, the partial cut-off frequencies are determined by multiplying the overall cut-off frequency with α_n. This results in the following cut-off frequencies:

$$\begin{aligned} \text{HP } f_{c1} &= 100\text{Hz} \cdot \alpha_1 \\ &= 100\text{Hz} \end{aligned} \qquad \begin{aligned} \text{HP } f_{c2} &= 100\text{Hz} \cdot \alpha_2 \\ &= 64\text{Hz} \end{aligned} \qquad \begin{aligned} \text{HP } f_{c3} &= 100\text{Hz} \cdot \alpha_3 \\ &= 51\text{Hz} \end{aligned} \tag{4-14}$$

The capacitors summarized in Table 4-7 were employed to implement the filters that define the specified bandwidth.

First stage	**Second stage**	**Third stage**
$C_{\text{f1}} = 2.7$ nF	$C_{\text{f2}} = 68$ pF	$C_{\text{f3}} = 91$ pF
$C_1 = 330$ nF	$C_2 = 470$ nF	$C_3 = 33$ nF
HP f_{c1}= 100 Hz	HP $f_{c2} = 64$ Hz	HP $f_{c3} = 51$ Hz
LP $f_{c1} = 18$ kHz	LP $f_{c2} = 28.1$ kHz	LP $f_{c3} = 35.3$ kHz

Table 4-7: Summary of the capacitors employed at each stage to partial cut-off.

Stability A frequency response plot of the third stage is given in Figure 4-8, where A_{ol} is the open-loop gain, $\frac{1}{\beta}$ the closed-loop gain and $A_{ol}\beta$ is the loop gain (T). From this plot it can be seen that the Phase Margin (PM) for the third stage is 83°, which satisfies the minimum specified PM of 45 degrees. Simulations of the first and second stage resulted in a similar PM of 83°. To check the stability of the complete circuit, a transient simulation was made with a step input, which is shown in Figure 4-9. The output response shows no oscillations or ringing in the signal, therefore the LNA circuit was found to be stable.

The magnitude and phase plot of the entire LNA circuit is shown in Figure 4-10, where it can be seen that the gain is maintained over the specified bandwidth. Below the high-pass corner frequency of 100 Hz, the gain is significantly less and starts to drop again as the frequency approaches the low-pass corner frequency of 18.000 Hz.

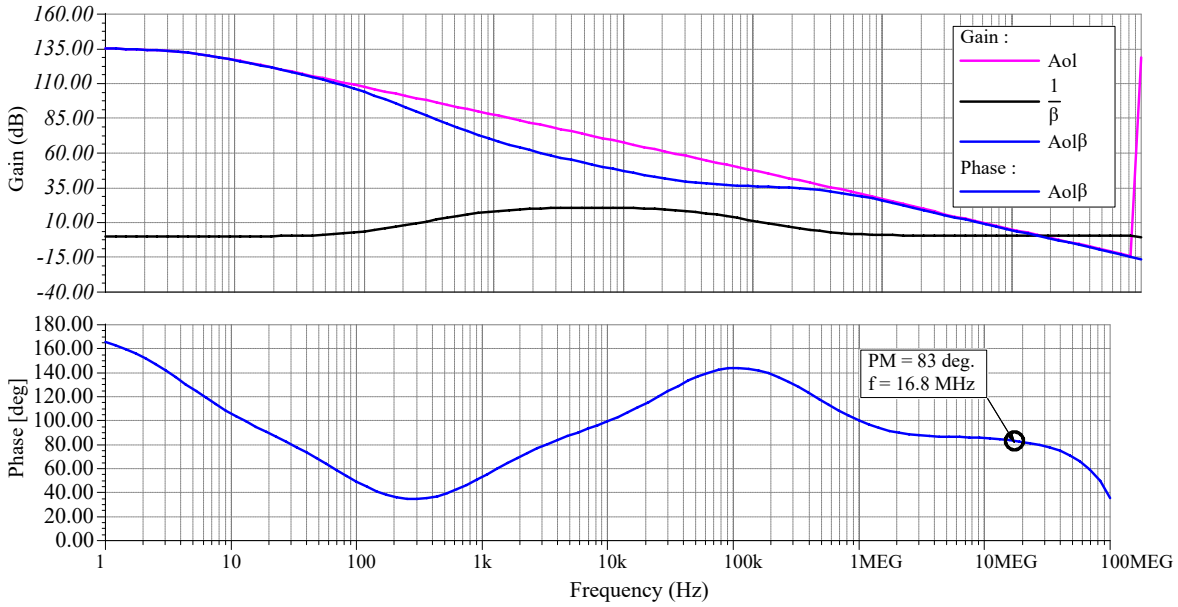

Figure 4-8: Frequency response of the last stage of the LNA circuit. At the unity-frequency of 16.8 MHz the gain is 0 and the PM = 83 degrees.

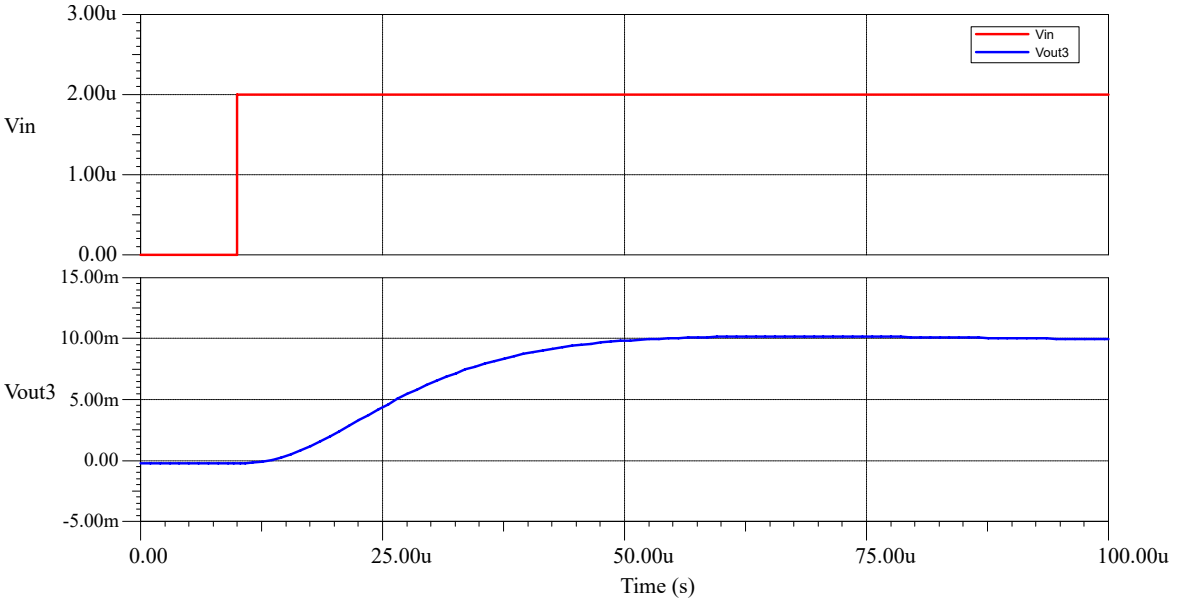

Figure 4-9: Response of the output with an applied step function input.

4-5-3 Noise

The total noise contribution at the input of the OPA209 comprises input current and voltage noise, thermal resistor noise and 1/f noise. The noise voltage density of the OPA209 was given as $e_n = 2.2\text{nV}/\sqrt{\text{Hz}}$. The current noise density is $i_n = 500\text{fA}/\sqrt{\text{Hz}}$ and with the resistor feedback network this equals $i_n = 500\text{fA}/\sqrt{\text{Hz}} \times R_{\text{eq}} = 0.048\text{nV}/\sqrt{\text{Hz}}$. The signal

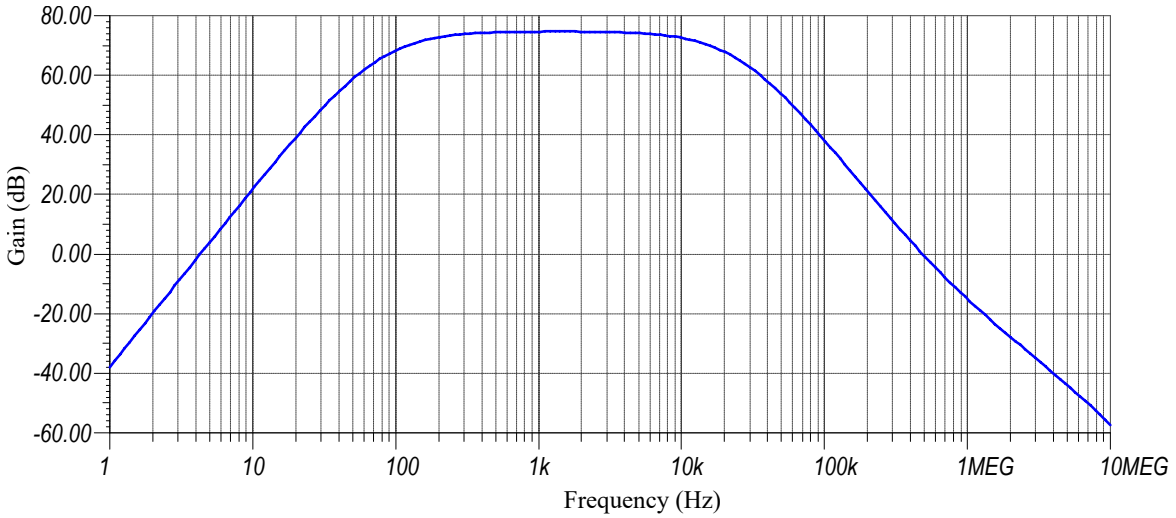

(a) Magnitude plot of the LNA circuit.

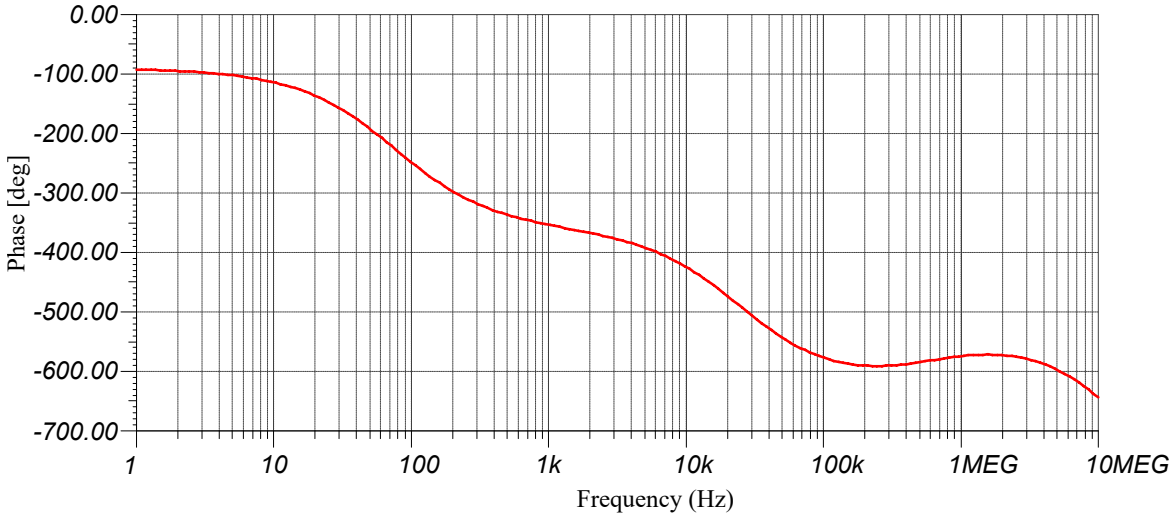

(b) Phase plot of the LNA circuit.

Figure 4-10: Bodeplot of the LNA circuit

bandwidth is given as: $\Delta\text{BW} = 18.000 - 100 = 17.900$ Hz. A correction factor K_n, also known as a "Brickwall correction factor" is used to account for the noise in the region beyond the cut-off region. For a first-order filter $K_n = 1.57$, the noise equivalent bandwidth (BW_n) then becomes $\Delta\text{BW} \times K_n = 26.690$ Hz. The thermal noise of a resistor was given by (3-18). The 1/f noise normalized to 1 Hz is given by looking at the noise contribution at 0.1 Hz, to ensure that the 1/f noise source is dominant. This gives 1/f noise as:

$$\begin{aligned} e_{nf} &= 22\frac{\text{nV}}{\sqrt{Hz}} \cdot \sqrt{1\text{ Hz}} \\ &= 22\text{ nV} \end{aligned} \tag{4-15}$$

The RMS noise contribution for each noise sources was determined with the following equa-

tions:

$$R_{\mathrm{eq,n}} = \sqrt{4kTR_{\mathrm{eq1}} \cdot \mathrm{BW_n}} \tag{4-16}$$

$$e_{n1} = 2.2\ \frac{\mathrm{nV}}{\sqrt{\mathrm{Hz}}} \cdot \mathrm{BW_n} \tag{4-17}$$

$$i_{n1} = 0.048\ \frac{\mathrm{nV}}{\sqrt{\mathrm{Hz}}} \cdot \mathrm{BW_n} \tag{4-18}$$

$$E_{nf} = e_{nf}\sqrt{\ln\left(\frac{f_H}{f_L}\right)} \tag{4-19}$$

$$\tag{4-20}$$

The total RMS noise contribution referred to the input can then be found by adding these uncorrelated sources together as:

$$E_{\mathrm{n,in}} = \sqrt{R_{\mathrm{eq,n}}^2 + e_{n1}^2 + i_{n1}^2 + E_{nf}^2} \tag{4-21}$$

The total RMS noise referred to the output of the first stage is equation (4-21) multiplied by the feedback gain:

$$E_{\mathrm{n,out}} = E_{\mathrm{n,in}}\left(1 + \frac{R_1}{j2\pi f_{c1} R_1 R_{f1} \mathrm{C_{f1}}}\right) \tag{4-22}$$

The values of the RMS noise contributions are summarized in Table 4-8.

Noise source	**RMS noise**
Total resistor ($R_{\mathrm{eq,n}}$)	206 $\mathrm{nV_{RMS}}$
Voltage noise (e_{n1})	360 $\mathrm{nV_{RMS}}$
Current noise (i_{n1})	7.9$\mathrm{nV_{RMS}}$
1/f noise	77.9 $\mathrm{nV_{RMS}}$
Total input referred noise	433 $\mathrm{nV_{RMS}}$
Total output referred noise	13.6 $\mu\mathrm{V_{RMS}}$

Table 4-8: Noise components and values of the first stage

From Table 4-8 it becomes clear that the resistor and voltage noise contributions are the dominant noise sources of the first stage and determine the total output noise. The noise sources of the second and third stage were found with a similar procedure and are given in Table 4-9. The 1/f noise source has been excluded, as the noise contribution of that source is negligible. Instead, the output noise of the first and second stage are given. The output noise of the first stage contributes noise to the input of the second stage and is the dominating noise source. In turn, the total output referred noise of the second stage dominates the noise contribution at the third stage. As expected, both of these noise sources are determined directly by the total input referred noise of the first stage. The total output noise of the LNA circuit could also be found by multiplying the input referred noise of the first stage with the total gain of the circuit: 433 $\mathrm{nV_{RMS}} \times 10^{(\frac{74\ \mathrm{dB}}{20})} = 2.17\ \mathrm{mV_{RMS}}$.

This confirms the importance of having the first stage optimized for low-noise. The total peak-to-peak output noise of the LNA circuit is found by multiplying the total output referred noise

Second stage	Third stage
Total resistor ($R_{\text{eq,n}}$) = 1.45 μV_{RMS}	Total resistor ($R_{\text{eq,n}}$) = 1.42 μV_{RMS}
Voltage noise (e_{n1}) = 360 nV_{RMS}	Voltage noise (e_{n1}) = 360 nV_{RMS}
Current noise (i_{n1}) = 390 nV_{RMS}	Current noise (i_{n1}) = 378 nV_{RMS}
Output noise first stage = 13.1 μV_{RMS}	Output noise second stage = 211.2 nV_{RMS}
Total input referred noise = 13.2 μV_{RMS}	Total input referred noise = 211.2 μV_{RMS}
Total output referred noise = 211.2 μV_{RMS}	Total output referred noise = 2.11 mV_{RMS}

Table 4-9: Noise components and values of the second and third stage

of the third stage with the standard deviation 6.6σ that was given from Table 3-3:

$$V_{\text{outPP}} = 2.11\ \text{mV}_{\text{RMS}} \times 6.6 = 13.93\ \text{mV}_{\text{PP}} \tag{4-23}$$

Figure 4-11 shows the noise analysis plots of the LNA circuit. The plots show that there are minor deviations between the calculated noise values and the values obtained from noise simulations. Thus, the noise simulations verifies the low-noise optimization at the input of the first stage and the overall noise contribution of the LNA circuit.

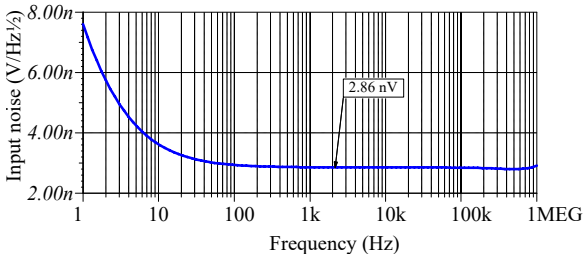

(a) Input referred noise of the first stage.

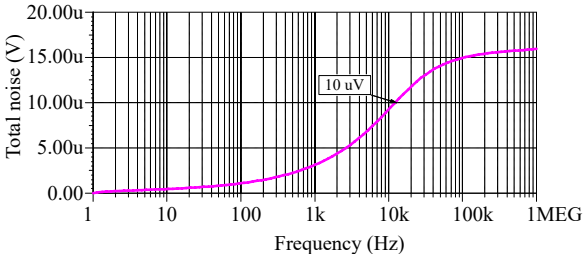

(b) Total output noise of the first stage.

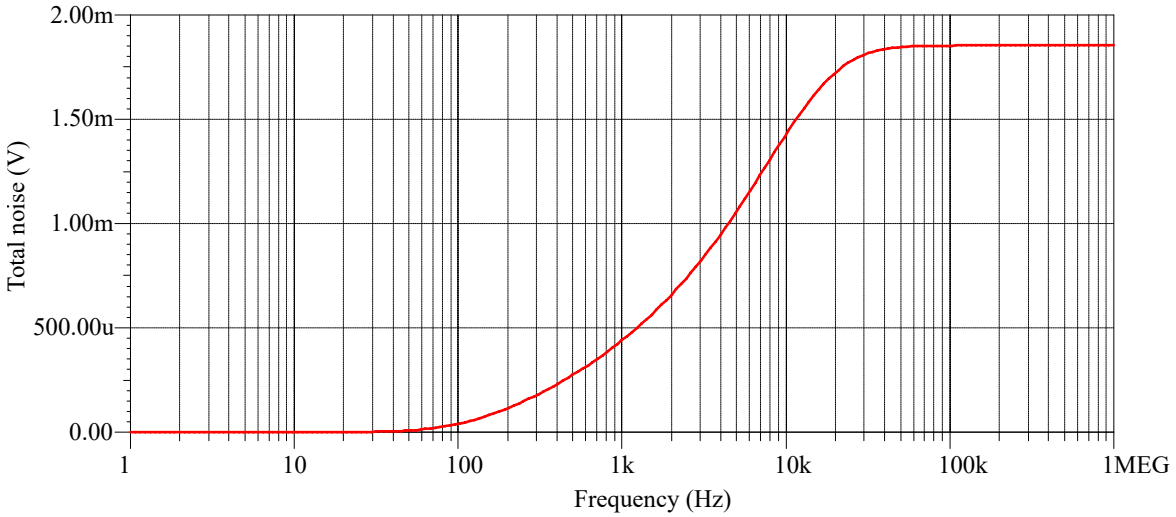

(c) Total output noise of the third stage.

Figure 4-11: Noise analysis plots of LNA circuit.

4-5-4 LNA Design Overview

The design requirements of the LNA were given in Table 3-4 of the previous chapter. The present LNA circuit design meets these requirements and the specifications of the LNA circuit are summarized in the table below:

Parameter	Value
Bandwidth	100 - 18.000 Hz
Closed-loop gain (A_{cl})	74 dB
Phase Margin	83°
Total output noise	13.93 mV_{PP}

Table 4-10: Achieved specifications by the LNA circuit.

4-6 Class D amplifier

For the implementation of the PA block, the trade-off has been made to opt for a class D amplifier development board rather than a specific designed circuit. A great advantage of the development board is that it simplifies the process of configuring the class D amplifier to drive the transmitter coil. In addition, it also provides options to control the input signal and gain. For the present Proof-of-Concept, the MAX98400A Evaluation Kit by Maxim Integrated [45] is employed and is shown in Figure 4-12. This development board comprises two MAX98400A class D amplifiers [46]. The evaluation kit is powered by a 12V battery and configured in mono-mode with a filtered output, as described in the datasheet.

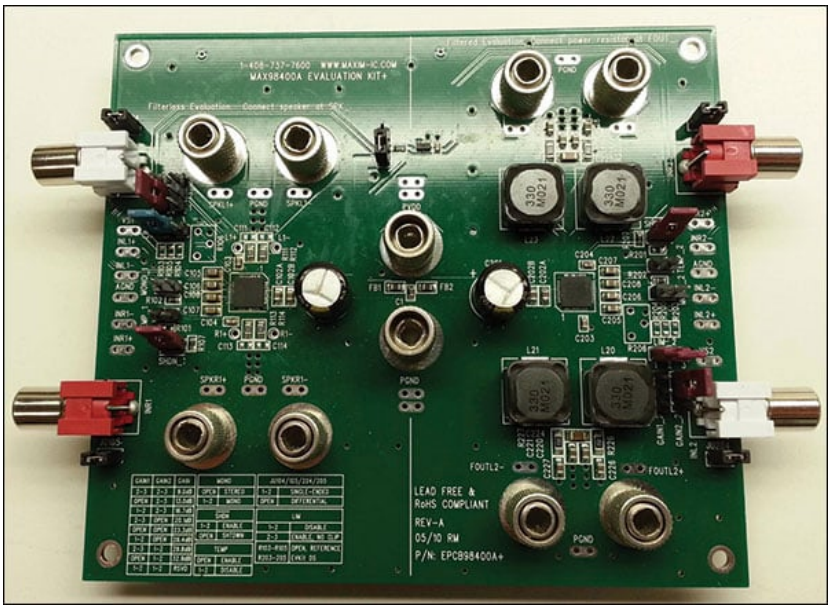

Figure 4-12: The Maxim Integrated MAX98400A Evalution kit utilized for the Proof-of-Concept

4-7 GPS

The GPS block was implemented by the Adafruit ultimate GPS breakout board [47], which is a GPS module that was ready to be used with the RPi. This board was operated by installing *GPSd* [48], which is a service daemon that handles GPS sensors attached to a USB or serial port. The GPS data was logged by using *gpspipe*, which is part of GPSd and retrieves NMEA sentences. An NMEA sentence contains information regarding the position, velocity and time of the GPS receiver. However, NMEA sentences are not in a readable text format. Therefore the .nmea files are converted into a plain text table with an online converter [49], which can be stored as a text file and merged with data files from the LIA. The text table contains the relevant parameters: date and time, latitude, longitude, altitude (m) and speed (km/h).

The interface with the designated pins of the RPi 3B is illustrated in Figure 4-13. In this schematic data is communicated with 9600 baud over the Tx and Rx pins. V_{in} is the supply voltage of 5V and is supplied by the RPi 3B. The Pulse-per-second (PPS) receives its signal from the PWM0 pin and serves to synchronize the RPi system clock with the GPS clock. This was accomplished by configuring the RPi to run Network Time Protocol (NTP) and synchronize an NTP server with the GPS clock. This server was used as the primary source to retrieve the date and time. It should be noted that there was an offset of 10 seconds between the time stamp of the measured signals and the GPS time stamp. However, for this Proof-of-Concept it was considered not to be problematic. An external LED was connected to the fix pin of the GPS board to indicate whether the GPS received a signal from the satellites. In case of a fix, the LED will blink once for a duration of 200 ms and repeats this process every 15 seconds. If the GPS does not have a fix, the LED blinks once per second while looking for GPS satellites. For the GPS fix indication, a typical LED is chosen with a 1 kΩ resistor connected in series to limit the current through the LED.

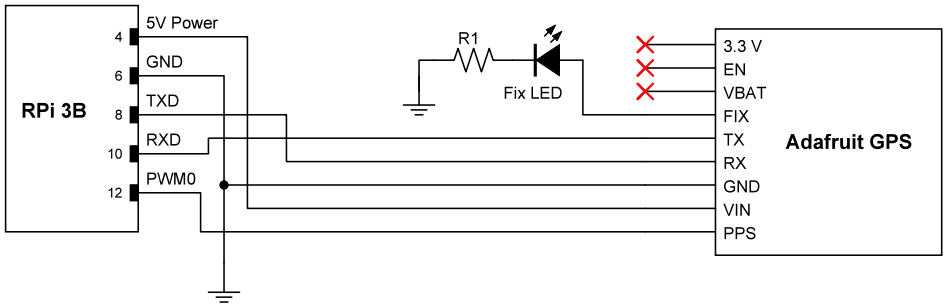

Figure 4-13: GPS interface schematic with a simplified RPi 3B block.

4-8 User Interface

Figure 4-14 shows the user interface circuit that was utilized to operate the measurement set-up. A Python script on the RPi operates the measurement set-up. The *power button* is used to control the power state of the RPi (see Appendix A-1). With the survey button, the lock-in amplifier application can be operated to start and stop a survey, while simultaneously the GPS data will be logged (see Appendix A-2). To indicate that a survey is in progress, a LED connected to pin 29 will blink with a 5 Hz frequency. Naturally, it will be off if no EM survey is in progress.

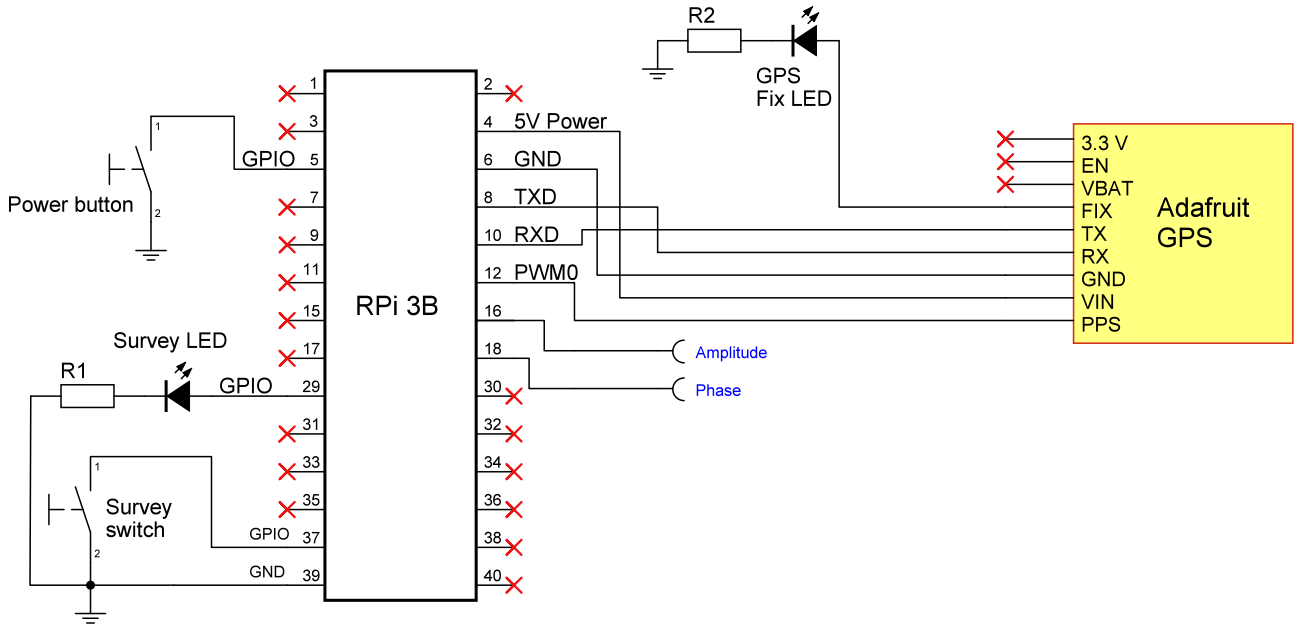

Figure 4-14: User interface circuit of the measurement set-up.

4-9 Summary

This chapter presented the design and implementation of the proposed system architecture of Chapter 3. The implementation of the Single-board Computer was realized by a Raspberry Pi 3B, which served as the main operator of the complete system and interfaces multiple blocks of Figure 3-2, namely the LIA, data conversion and GPS blocks.

The receiver coil has been redesigned to have a diameter of 20 cm and 1000 windings. A wire thickness of 0.4 mm was chosen in order to comply with the requirements for payload and noise contribution.

Next, the design of a dual-phase digital LIA in Simulink was described. The implementation of the LIA was done on the Raspberry Pi 3B. The Sweex SC016 USB sound card was utilized for the data conversion of signals from the analog domain to digital domain and vice-versa. The sample rate of the LIA was limited to the Sweex SC016 sample rate of 48.000 Hz. To avoid aliasing and reduce RAM usage, decimation and low-pass filtering was applied which limited the operating bandwidth to 12.000 Hz. The measured data is stored as a MAT-file on a SD-card that is connected to the RPi 3B. The MAT-file can be viewed and processed in MATLAB for further data analysis.

A three-stage cascaded OPA209 amplifier circuit was designed to increase the generated receiver coil voltage. The first stage of the circuit was optimized for low-noise and high gain, 32 dB. The second and third stage provided the additional gain of 24 dB and 20 dB, so that the total circuit has a gain of $\sim$74 dB. Hand calculations and noise simulations were performed and indicated that the total input referred noise of the first stage was around 2.86 nV/$\sqrt{\text{Hz}}$. The total output noise at third stage was found to be 13.93 mV$_{PP}$. The LNA circuit was implemented on a perfboard and enclosed by a metal case, to reduce potential EM interference. The Power Amplifier was implemented by the MAX98400A Evalution kit from Maxim Integrated and was used to drive the transmitter coil.

Lastly, A GPS circuit was implemented by the Adafruit ultimate GPS breakout board and connected with various GPIO pins of the RPi 3B. A Python script that runs on the RPi, logs the GPS data and saves it as an .nmea file. The GPS also synchronizes the system clock of the RPi 3B with the GPS clock through an NTP server. With the implementation of the proposed system architure completed, the Proof-of-Concept could be tested in the field. The following chapter will describe the measurements and results of the field test.

Chapter 5

Measurements

The proposed Proof-of-Concept was implemented in the previous chapter. To evaluate the feasibility of the concept, a field test was conducted with the implemented Proof-of-Concept. The results and measurements are described in this final chapter. In order to have measurement and result reference, a similar measurement was performed with a GEM-2A FDEM sensing instrument.

5-1 Measurement Setup

The measurement set-up that was used to test the Proof-of-Concept is shown in Figure 5-1. As can be seen in the picture, the measurement setup is made in a portable set-up. With a shoulder strap the measurement setup could be carried and tested in the field. A PVC tube with a length of 4 meter was used to emulate the wingspan of the intended UAV; the receiver, bucking and transmitter coil were attached to each end of the PVC tube, as indicated in the picture.

Transmitter Coil Adjustments It was advised by the project supervisor to employ a different transmitter coil, then the transmitter coil from Table 3-1 that was provided by SkyDowser. There was not enough time to explore which transmitter coil would be best, hence two different coils were employed, one with 8 windings and one with 45 windings, both were wound around a PVC tube. A switch attached to the transmitter coils made it possible to select one transmitter coil at a time.

Measurement Site The measurements were performed in Hoek van Holland. This measurement site was selected by the SkyDowser team on the basis of the properties of groundwater in that area, which should have an observable transition from salt water to fresh water. Aside from seawater and groundwater, the area is also rich in sand and dunes.

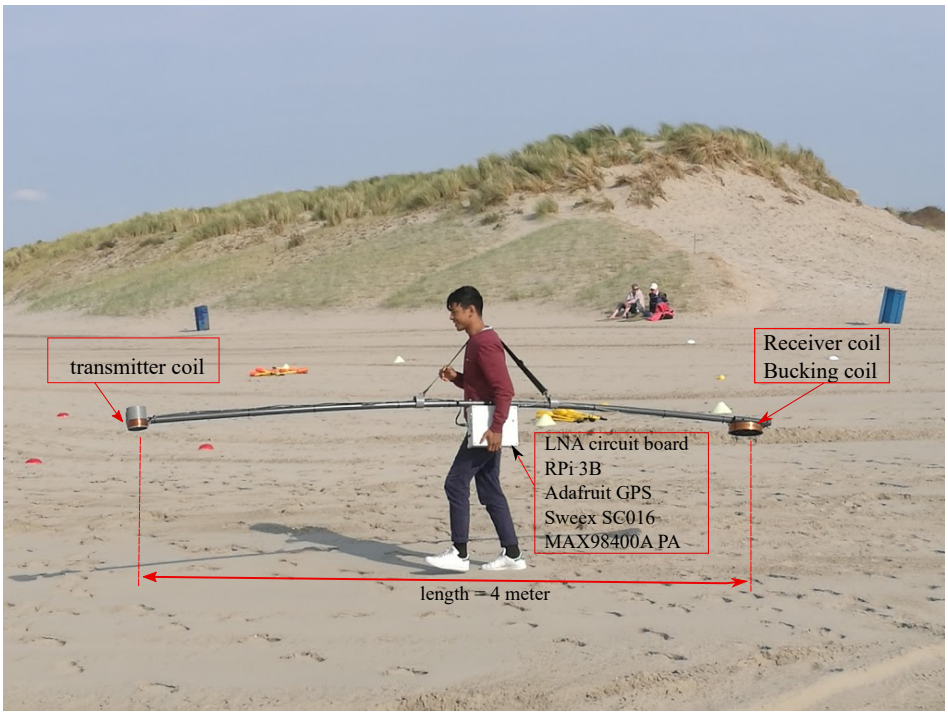

Figure 5-1: Measurement setup used to test the Proof-of-Concept. The implemented blocks from chapter 3 and 4 are indicated in red.

Measurement Instruments Two different measurement instruments were employed during the field test:

1. **GEM2-A FDEM instrument:** This measurement instrument was able to perform a multi-frequency measurement during one survey. The measurements were done with frequencies at 925, 2175, 5025, 9825 and 20.025 Hz. Which are multiples of the *base period* 1/25 seconds in a 50 Hz area and chosen to minimize powerline noise interference. The measurement route followed a line pattern as shown in Figure 5-2a.

2. **SkyDowser Proof-of-Concept measurement instrument:** This measurement instrument was not able to perform a multi-frequency measurement during a survey. As a result, multiple surveys had to be performed to cover the same frequencies as the GEM-2A, with the exception of measurements at 9825 and 20.025 Hz, which were not possible due to the sample rate limitation of the Sweex SC016 and the LPF of the digital LIA. As replacement, a measurement at 400 Hz was done. At each frequency a measurement was done twice, where one measurement was carried out with the transmitter coil of 8 windings and the second measurement with the transmitter coil of 45 windings. Thus, in total 8 measurements were carried out. It was physically more challenging to carry out measurements with the SkyDowser instrument than with the GEM-2A, this was mainly caused by the length of the PVC pipe, which had a leverage effect that needed to be balanced by the operator. Hence, the measurement route had a rectangular pattern instead of a line pattern.

(a) Measurement route with GEM-2A instrument. **(b)** Measurement route with SkyDowser instrument.

Figure 5-2: Measurement routes with the FDEM instruments.

5-2 Measurement Data

The measurement data of the GEM-2A was used as a reference to verify the measurement data of the Proof-of-Concept. However, a direct comparison between the measurement data was not possible, because the GEM-2A yields electrical conductivity and magnetic fields, which are normalized with the reference signal and expressed as a dimensionless unit of parts-per-million (PPM), whereas the Proof-of-Concepts yields a voltage in terms of magnitude and phase. Furthermore, the measurement route differ from each other. Therefore the data was analyzed as follows:

1. From the GEM-2A data from line 1 and 4 was analyzed. From the Proof-of-Concept, data from the longer path towards the sea and away from the sea was analyzed. Both these pathways are similar to each other.
2. From the GEM-2A the magnitude ($\sqrt{I^2 + Q^2}$) and phase ($\tan^{-1}(\frac{Q}{I})$) of the I and Q components were calculated.
3. A moving average filter is applied to indicate the trend and smooth out spikes in the curve of the plots.

In order to find a correlation between the data of both instruments, the trend in the curve of the plots was analyzed. The data plots are given below:

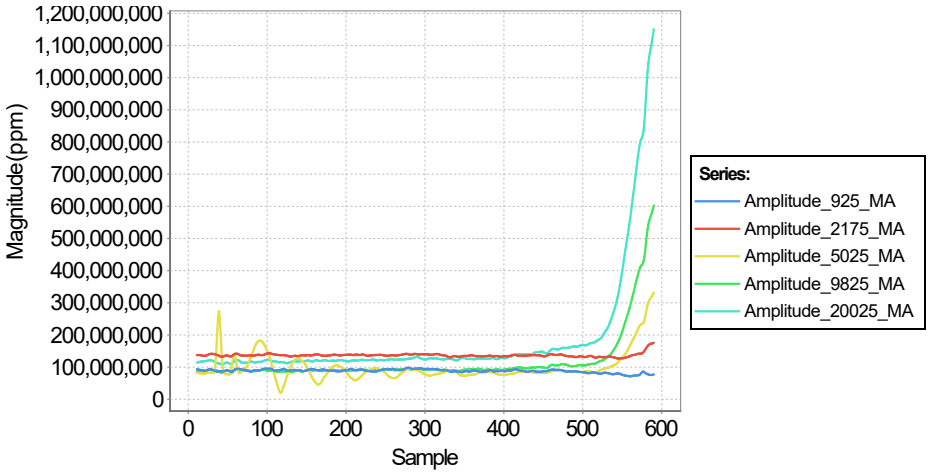

(a) Line 1 magnitude values.

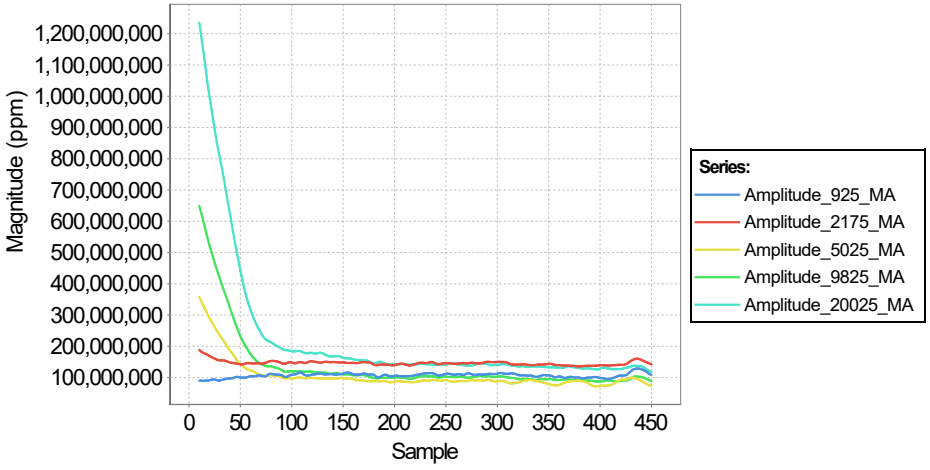

(b) Line 4 magnitude values.

Figure 5-3: Magnitude plot of the GEM-2A measured I and Q components of line 1 and line 4 with a moving average filter.

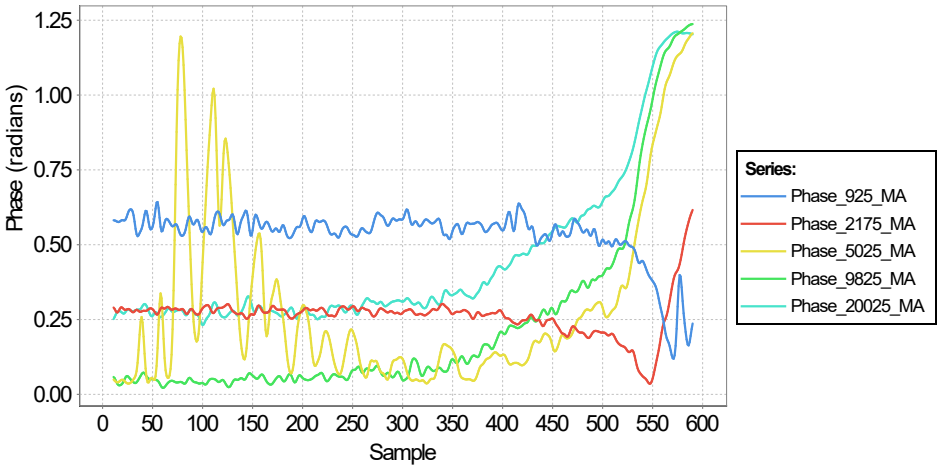

(a) Line 1 phase .

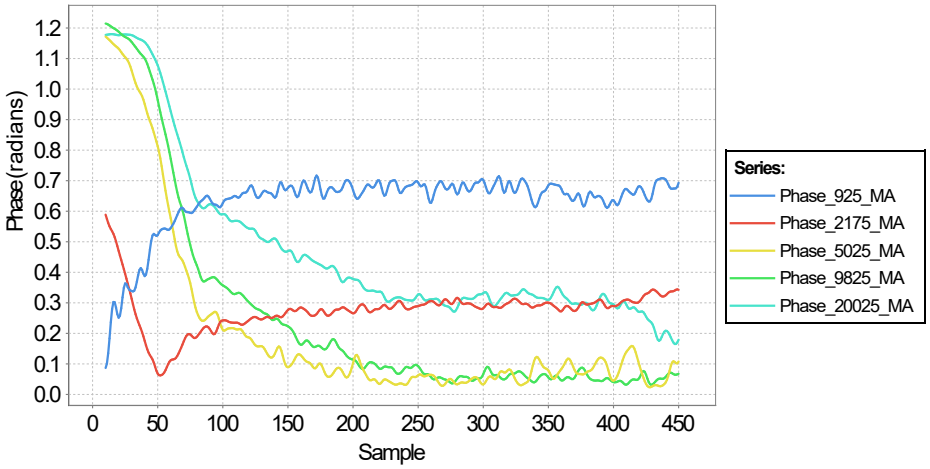

(b) Line 4 Phase.

Figure 5-4: Phase plot of the GEM-2A, between the measured I and Q components of line 1 and line 4 with a moving average filter.

(a) Amplitude plot of line 1.

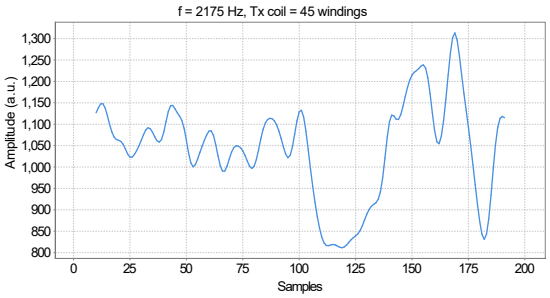

(b) Amplitude plot of line 4.

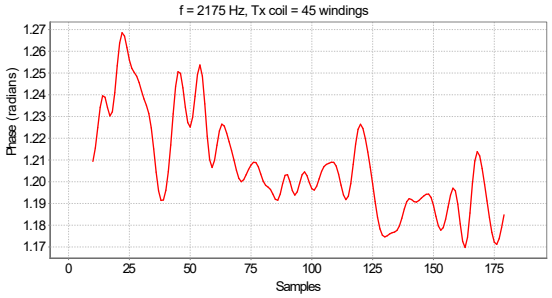

(c) Phase plot of line 1.

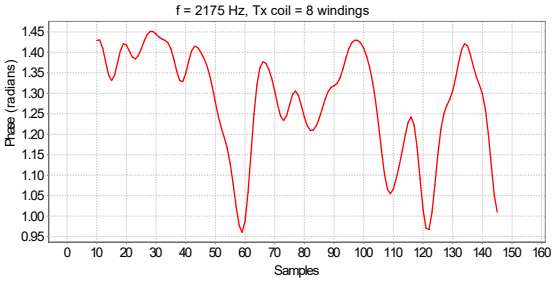

(d) Phase plot of line 4.

Figure 5-5: Amplitude and Phase measurement plots of the SkyDowser POC at f = 2175 Hz and Tx coil of 45 windings.

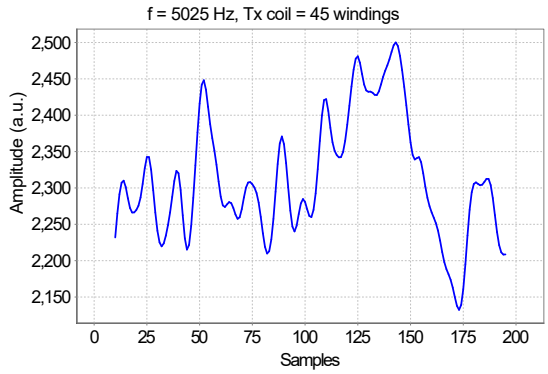

(a) Amplitude plot of line 1.

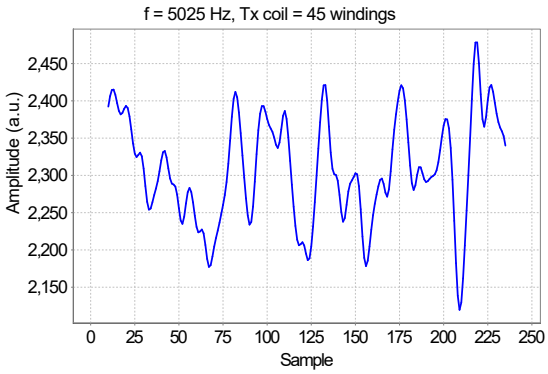

(b) Amplitude plot of line 4.

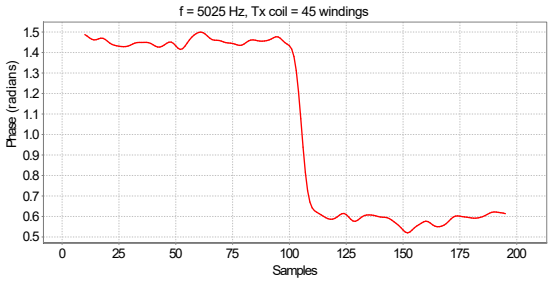

(c) Phase plot of line 1.

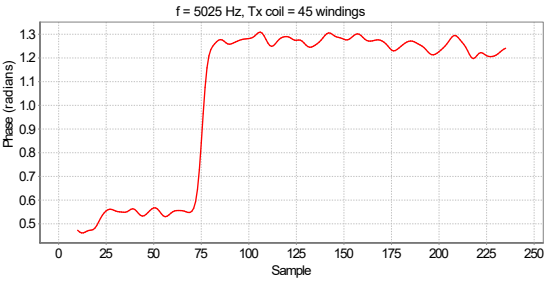

(d) Phase plot of line 4.

Figure 5-6: Amplitude and Phase measurement plots of the SkyDowser POC at f = 5025 Hz and Tx coil of 45 windings.

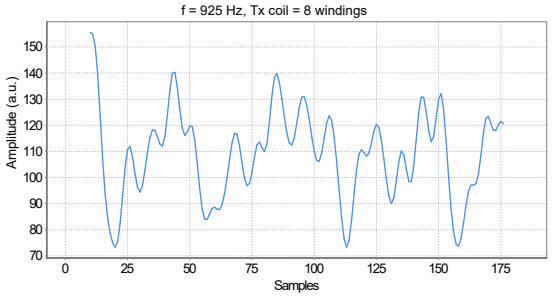

(a) Amplitude plot of line 1.

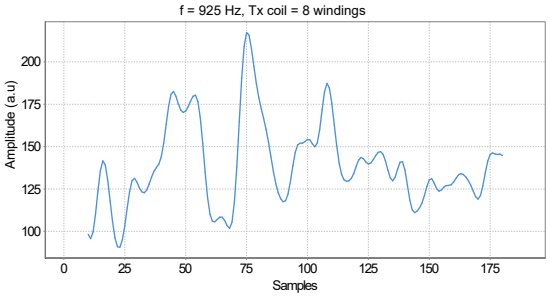

(b) Amplitude plot of line 4.

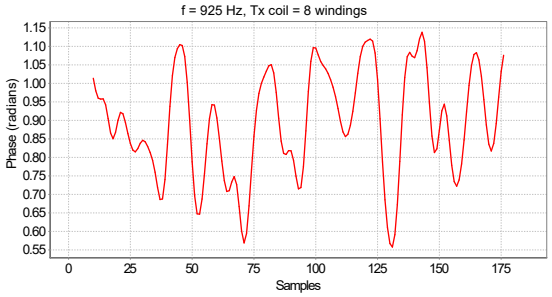

(c) Phase plot of line 1.

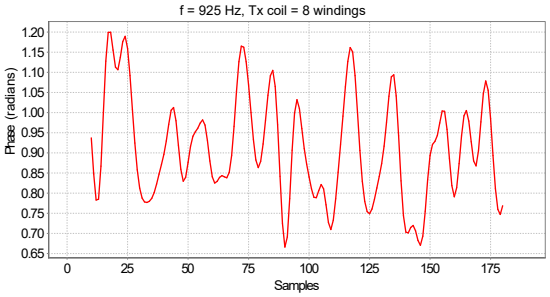

(d) Phase plot of line 4.

Figure 5-7: Amplitude and Phase measurement plots of the SkyDowser POC at f = 925 Hz and Tx coil of 8 windings.

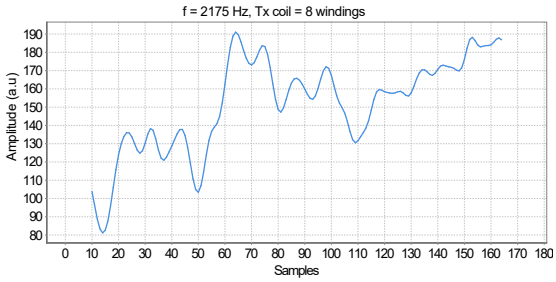

(a) Amplitude plot of line 1.

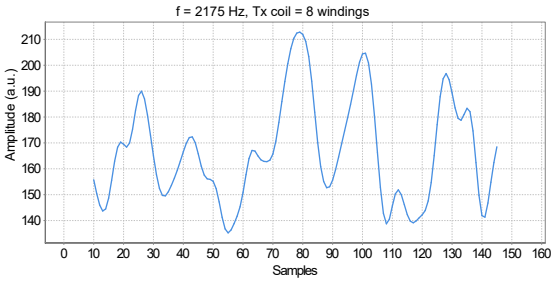

(b) Amplitude plot of line 4.

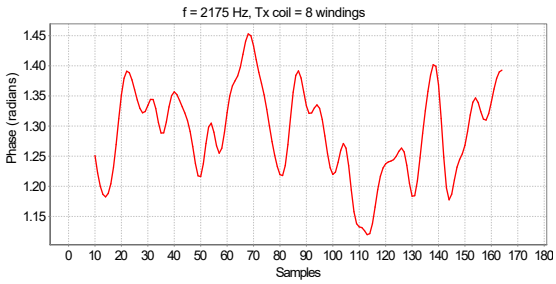

(c) Phase plot of line 1.

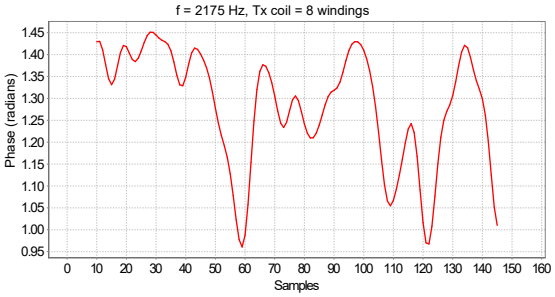

(d) Phase plot of line 4.

Figure 5-8: Amplitude and Phase measurement plots of the SkyDowser POC at f = 2175 Hz and Tx coil of 8 windings.

(a) Amplitude plot of line 1.

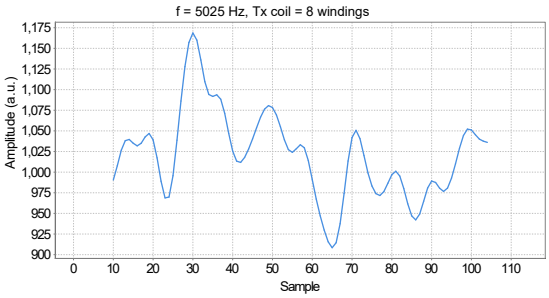

(b) Amplitude plot of line 4.

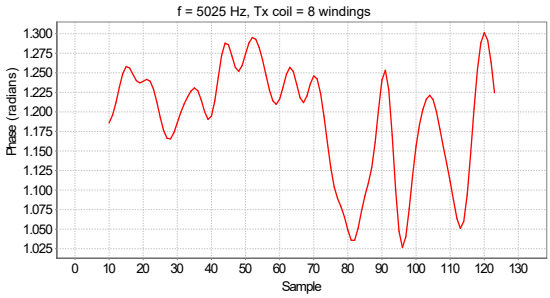

(c) Phase plot of line 1.

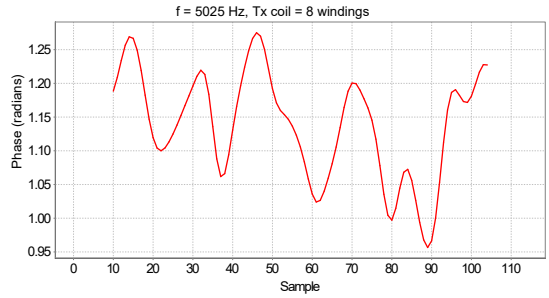

(d) Phase plot of line 4.

Figure 5-9: Amplitude and Phase measurement plots of the SkyDowser POC at f = 5025 Hz and Tx coil of 8 windings.

5-2-1 Data Analysis

GEM-2A Data Figure 5-3 shows the magnitude plots of the GEM-2A measurements. It can be observed from these plots that the magnitude increases as the measurements were taken near the end of line 1 and shows a decreasing trend at the beginning of line 4. This behavior is expected as the conductivity of sea water is higher than that of sand, thus it results in an increasing trend towards sea water and a decreasing trend away from seawater.
Measurements at all frequencies indicate a similar trend, which also accounts for the phase plots of Figure 5-4a and Figure 5-4. Therefore, it can be concluded from the GEM-2A plots that there is a close agreement between the measurement data at each frequency and that the GEM-2A shows an expected behavior in the plots.

SkyDowser Proof-of-Concept With the SkyDowser Proof-of-Concept a total of nine measurements were carried out and five measurements were analyzed:

- The measurement at 2175 Hz with a transmitter coil of 45 windings was performed twice and the first measurements data found to be the best for the data analysis.
- Unfortunately the measurements data at frequency of 925 Hz with transmitter coil of 45 windings was lost during the data transfer from the Proof-of-Concept to the laptop and could therefore not be analyzed.
- A quick analyses of the measurement results at frequency of 400 Hz indicated that there was no agreement between the measurements with 8 windings and 45 windings. Furthermore, there were no reference data from the GEM-2A at that frequency and for that reason, the results were not analyzed any further.

From careful analysis of the Proof-of-Concept plots it was found:

- There is no noticeable trend to be found in each plot. Neither at Tx = 45 windings or Tx = 8 windings.
- No correlation with the plots of GEM-2A could be observed.

The measured data of the SkyDowser Proof-of-Concept was therefore found to be inadequate. This can be attributed to the following possible contributors:

(a) **Low transmitter current** - The maximum current through the transmitter coil was measured and was found to be around 1 A. The GEM-2A has a transmitter current of around 3 A at 330 Hz. The current is inversely proportional to frequency, therefore the primary magnetic field could have been too weak to generate a measurable secondary field in the conductor.

(b) **Parasitic capacitance** - The transmitter and receiver coil were wound manually. The receiver coil comprises 1000 windings over several layers. The separation between layers forms a parasitic capacitance. The impedance of a capacitor is inversely proportional to the frequency and given as $Z_C = \frac{1}{j\omega C}$; the inductor impedance is proportional to the

frequency and given as $Z_L = j\omega L$. A possible effect that could have occurred is that the total impedance of the parasitic capacitance is lower than the inductor impedance, as the frequency increases. Thus, the parasitic capacitance of the coils could have effected the generated magnetic fields.

(c) **Coil coupling** - During the measurements the PVC tube had severe vibrations that hampers the coupling (given in Section 3-2) between the coils and conductor. Ideally, the coils need to be in a steady position for maximum coupling between the coils and conductor. With reduced coupling, the magnetic flux in the conductor and receiver coil reduces and as a results the generated voltage can be too weak to be detected.

(d) **Transmitter coils** - Both transmitter coils (8 and 45 windings) were wound around the same tube. This could lead to coupling between both transmitter coils and the receiver coil, consequently corrupting the measurement data.

(e) **Insufficient bucking of primary magnetic field** - The placement of the bucking coil was around the receiver coil. The GEM-2A has the bucking coil separated from the receiver coil. It could be the case that the bucking coil did not buck out the primary signal at the receiver coil. Hence, the secondary field that is typically several magnitudes lower, could not be detected at all by the receiver coil.

It should, however, be noted that the list above gives possible causes for the inadequate data and these were not investigated in this work to verify their contribution. Future work should therefore focus on determining which contributor had a critical impact on degrading the measurement instrument.

5-3 Summary

Measurements of the GEM-2A and SkyDowser Proof-of-Concept are discussed in this chapter. The GEM-2A measurement was used as a reference to verify the performance of the Proof-of-Concept. A direct comparison between the measurement results was not possible, because the measurement units of the GEM-2A and SkyDowser Proof-of-Concept were not identical. In an attempt to find an agreement between the measurement results, the measurement plots were analyzed for a common trend. A clear trend was found in the measurement plots of the GEM-2A. However, the SkyDowser Proof-of-Concept measurements did not show the same trend. Also, there was no correlation between the various measurement plots. Possible contributors that could have caused the deteriorated measurement results have been identified and their actual effect on the measurement performance needs to be further investigated in future work.

Chapter 6

Conclusion

6-1 Problem Definition

Clean drinking water is a primary need for humanity, yet 1 in 9 people in the world lack to meet daily needs of clean water. Groundwater is a water supply source that provides a good solution, as this requires minor water treatment. EM exploration is a commonly used survey method to find groundwater. In order to cover a wider survey area in less time, FDEM instruments are used in conjunction with aerial vehicles, also known as AEM. However, the majority of commercially available AEM systems are rather expensive, time consuming and not portable. To provide a portable, inexpensive alternative, SkyDowser wants to develop a FDEM-survey instrument that will be mounted on a UAV. Hence, this thesis focused on a Proof-of-Concept based on the FDEM method.

6-2 Thesis Contribution

This thesis explores a novel method for an airborne frequency domain electromagnetic survey instrument that is targeted towards groundwater detection and expand prior work presented in [5]. The previous system architecture has been revised by top level system selection considerations that are determined by core specifications given by SkyDowser. Following that, the system architecture determines the design specifications of each system block. A complete implementation of the system was demonstrated with a Proof-of-Concept and experimental measurements were carried out. These measurements have been compared with GEM-2A measurements, from which it was concluded that the measurements of the GEM-2A and the proposed Proof-of-Concept were not in line with each other. To summarize, the key contributions of this work are as follows:

- In Chapter 2, a literature review of electromagnetic theory and EM survey was given as background for the EM survey method of this work. The necessary components and constitutive relations that describe an EM field were discussed. This was followed by

a discussion of the Maxwell equations. From the constitutive relations and Maxwell's equations, the diffusion of EM fields was given. The chapter concluded with an overview of Time Domain Electromagnetic and a comprehensive review of Frequency Domain Electromagnetic.

- In Chapter 3, the proposed FDEM system architecture was presented. It utilizes three coils to provide the system with a transmitter, receiver and compensation coil. The coupling relation between the coils and conductor were described. A Single-board Computer was chosen as the main operator of the system, it provides a user interface to the system and takes care of signal processing. To transmit a proper signal through the transmitter coil, a Power Amplifier is employed. Several PA classes have been reviewed and after a comparison, it became apparent that a Class-D PA was a good choice. An A/D converter is employed to transfer the receiver coil signal from the analog domain to the digital domain of the SBC. The important definitions of the A/D converter specifications were described. Further, a brief study of the SAR architecture and $\Sigma\Delta$ architecture was given and both architectures can be employed for the proposed system. A Low-noise amplifier is added to ensure that the receiver coil signal is within the input range of the A/D converter. The fundamental performance parameters of the LNA were reviewed to set up design specifications. Further signal processing is done by a Lock-in Amplifier. In order to understand its function in the system, the operating principle and different architectures were reviewed. It was decided that a dual phase digital LIA was the best choice for this system. Lastly, the system architecture employs a GPS to provide the measurements with location data.
- Chapter 4 describes the main part of this thesis. In this chapter, the system architecture of Chapter 3 was implemented as a Proof-of-Concept. The following system blocks were designed:
  (a) It was found that the receiver coil provided by SkyDowser could not generate an appreciable signal. To surpass this limitation, a new receiver coil was designed and implemented. It was predicted that a voltage of around 25 μV could be generated if a coil with 1000 windings and a diameter of 0.2 m would be used. In order to balance the weight and the noise contribution of the copper wire, a wire diameter of 0.4 mm was chosen to implement the coil.
  (b) The voltage generated in the receiver coil is a weak signal that cannot be detected by the input of an A/D converter. In order to overcome this issue, a three-stage LNA circuit was designed. The LNA was implemented by Texas Instrument OPA209 IC. The operating bandwidth of the circuit is between 100 - 18.000 Hz and it achieves a total gain of about ~74 dB. Additionally, the noise contribution of the circuit was identified and optimized, such that the receiver coil signal does not get altered significantly. The noise calculations were verified by simulating the designed circuit.
  (c) A digital dual phase LIA application was designed in Simulink and implemented on a Raspberry Pi 3B. To interface the RPi 3B with the LNA, a Sweex SC016 USB Sound Card is employed as the data converter block of the system. The LIA also provides the compensation coil and the transmitter coil with a signal. Due to limitations of Simulink, the LIA could only store the measured data in MAT file on a SD-card that is connected to the RPi.

(d) A simple User Interface has been implemented on the RPi 3B to operate the Proof-of-Concept. The RPi is turned on with a push button. Once the system is on, the system can start a survey by pressing another push button that will start the LIA application and logs GPS data. If that same button is pressed again, the system will stop the survey and saves the GPS log and LIA data.

- The measurements of the Proof-of-Concept and GEM-2A instrument were presented in Chapter 5. The GEM-2A measurements were carried out with an operating frequency of: 925, 2175, 5025, 9825 and 20025 Hz and the Proof-of-Concept measurements were carried out with an operating frequency: 400, 925, 2175 and 5025 Hz. The GEM-2A measurements were used as a reference to validate the performance of the Proof-of-Concept. From the GEM-2A measurements, expected results were obtained and a good agreement was shown between the different frequencies. No agreement could be found between the GEM-2A and Proof-of-Concept. Moreover, there was no correlation between the measurements from the Proof-of-Concept at each operating frequency. A list of possible contributors that could have caused this performance problem was given.

6-3 Future Work

The system architecture that was proposed in Chapter 3 and implemented as a Proof-of-Concept in 4 can serve as a starting point for the FDEM measurement instrument that SkyDowser wants to develop. However, the experimental measurements with the Proof-of-Concept gave results that were inconclusive, therefore future work is required to develop a mature prototype. Building on this work, the following directions could be explored to improve the performance of the Proof-of-Concept:

- **Coil sensors and magnetic field analysis:** During the measurements of this work, two transmitter coils (45 windings coil and 8 windings coil) were employed. It would be of great interest to determine specifications (diameter, number of windings, weight) for just one transmitter coil. Moreover, the coils were wound by hand, which leaves room for error and makes the specifications less accurate. Thus, means of accurately winding the coils is recommended. A next step would be to analyze the coupling relation between the coils and the subsurface of the chosen test site. Electromagnetic survey simulation software is recommended to give a better coil relation model and insight. Additionally, actual measurement of the magnetic field strength of each coil should verify the simulations/calculations. It would also be interesting to find out what the magnetic field strength of the GEM-2A instrument is and use that as a reference. By exploring these recommendations, the examination of the potential contributors listed in Section 5-2-1 is also covered.

- **Dedicated circuits and DSP:** The data converter block of the system was implemented by the Sweex SC016 USB Sound card that has a sample rate of 48.000 Hz. Therefore, the operating bandwidth of the Proof-of-Concept was limited and measurements at operating frequencies of 9825 Hz and 20025 Hz could not be carried out. Replacing the USB sound card with an A/D circuit with a higher sample rate would deal with this limitation. This would require to review the LNA circuit again to see

if the circuit is able to drive the A/D converter. Also, it would be recommended to implement the LNA circuit on a PCB instead of a perfboard.
Simulink allowed rapid prototyping of the LIA, but it also had some limitations that hampered the performance of the Proof-of-Concept and several workarounds had to be created. Thus, the next step would be to implement the digital dual phase LIA on a dedicated DSP outside the Simulink environment. From the microcontroller it is expected to read in the GPS data and store the measured data as CSV file. Finally, the PA development board can be replaced by a custom designed circuit, to provide the current to the transmitter coil that is needed to generate the required magnetic field strength that was given in the previous recommendation.

- **Lab test:** In this work, the Proof-of-Concept was only tested in the field. It would be highly desirable to test a next version in a lab, before carrying out measurements in the field. Individual tests of each system block should also indicate whether the expected performance of each block is achieved. By testing the complete system and individual blocks of the system in a lab, occurring issues can be narrowed down and identified faster.

- **Measurement analysis software:** The GEM-2A and the Proof-of-Concept did not have the same measurement units, which made it hard to do a side-by-side comparison. Hence, a way of converting the LIA measurement data into the same data format as the GEM-2A should be investigated. This can be done directly on the DSP or by conversion software application on a computer.

Appendix A

Python Code

A-1 Shutdown Script

```
#!/usr/bin/python
import RPi.GPIO as GPIO
import time
import subprocess

GPIO.setmode(GPIO.BOARD)

GPIO.setup(5, GPIO.IN, pull_up_down = GPIO.PUD_UP)
#Button connected to board pin 5
button_state2 = True

while True:
#check current button state
button_state1 = GPIO.input(5)

#See if the button is pressed
if button_state1 != button_state2 and button_state1 == False:
subprocess.call("shutdown -h now", shell=True,
stdout=subprocess.PIPE, stderr=subprocess.PIPE)
oldButtonState1 = buttonState1

time.sleep(.1)
```

A-2 Start Survey Script

```
  #!/usr/bin/python
  import RPi.GPIO as GPIO
  import time, os
  from time import sleep
  import subprocess
```

```
6
7   #Use GPIO pin numbers
8   GPIO.setmode(GPIO.BOARD)
9   GPIO.setwarnings(False)
10
11  switch_pin = 37 #Button to start and stop a survey
12  led_pin = 31 #Drives the LED to indicate whether a survey is in
        progress
13
14  GPIO.setup(switch_pin, GPIO.IN, pull_up_down=GPIO.PUD_UP)
15  GPIO.setup(led_pin, GPIO.OUT)
16  state = 0
17
18  while True:
19  input = GPIO.input(switch_pin)
20  if (input == False): #Press the button to start the if-else loop.
21  if (state == 1):  #If state equals 1 then the Survey will stop.
22  print("Survey has stopped")
23  subprocess.Popen("killall lockinFinal.elf", shell=True) #Use the shell
        command killall to stop the Lockin Amplifier.
24  state = 0 #Change the state back to 0. So that the system can start a
        new survey when the button is pressed again.
25  elif (state == 0):  #Start survey begins here
26  print("start survey")
27  subprocess.Popen(r"/home/pi/lockinFinal.elf", cwd=r"/home/pi/") #Start
        the Simulink Lockin Amplifier application. Change the working
        directory to /home/pi. To retrieve the data.
28  state = 1
29  sleep(0.5) #sleep 0.5 seconds.
```

Bibliography

[1] R. Kirsch, *Groundwater Geophysics: A Tool for Hydrogeology*. Springer.

[2] L. Marescot. (2013) Electromagnetic surveying. [Online]. Available: http://www.tomoquest.com/attachments/File/EEG_Electromagnetic_surveying.pdf

[3] Raspberry pi 3b. Raspberry Pi Foundation. [Online]. Available: https://www.raspberrypi.org/products/raspberry-pi-3-model-b/

[4] W. Telford, *Applied Geophysic*. Cambridge University Press, 2004.

[5] R. J. Tharian, "A light-weight electromagnetic based embedded sensing system for groundwater exploration," Master's thesis, Delft University of Technology, 2017.

[6] H. B. M.D. Verweij, P.M. van den Berg, *Electromagnetic Waves: An Introductory Course*, 2nd ed. Delft University Press, 2001.

[7] S. H. Ward, G. W. Hohmann, and M. Nabighian, "Electromagnetic theory for geophysical applications," in *Electromagnetic methods in applied geophysics*, vol. 1, no. 3, 1988, pp. 131–311.

[8] G. West and J. Macnae, "Electromagnetic methods in applied geophysics," *SEG. Chapter physics of the electromagnetic induction exploration method*, 1991.

[9] T. B. H. P.S Klinkert, P.B. Leggatt, "The spectrem airborne eletromagnetic system latest developments and field examples," *Proceedings of Exploration 97: Fourth Decennial International Conference on Mineral Exploration*, 1997.

[10] U. M. Bernhard Siemon, "Helicopter-borne geophysics and remote sensing at bgr," March 2015.

[11] K. Knödel, G. Lange, and H.-J. Voigt, *Environmental geology: handbook of field methods and case studies*. Springer Science & Business Media, 2007.

[12] F. W. Grover, *Inductance Calculations*. Dover Publications inc., 2009.

[13] G. A. Newman and D. L. Alumbaugh, "Frequency-domain modelling of airborne electromagnetic responses using staggered finite differences," *Geophysical Prospecting*, vol. 43, no. 8, pp. 1021–1042, 1995.

[14] D. B. Avdeev, A. V. Kuvshinov, O. V. Pankratov, and G. A. Newman, "Three-dimensional frequency-domain modeling of airborne electromagnetic responses," *Exploration Geophysics*, vol. 29, no. 1/2, pp. 111–119, 1998.

[15] P. R. Gray, P. Hurst, R. G. Meyer, and S. Lewis, *Analysis and design of analog integrated circuits*, 5th ed. Wiley, 2009.

[16] K. Bult, *Basic Analog CMOS design an intuitive approach*, 2010.

[17] B. Razavi, *Design of analog CMOS integrated circuits*. New York, NY: McGraw-Hill Education, 2017.

[18] S. Franco, *Design with operational amplifiers and analog integrated circuits*, 3rd ed. McGraw-Hill, 2002.

[19] W. Jung, *Op Amp applications handbook*, 1st ed. Newnes, 2005.

[20] F. Maloberti, *Data converters*. Springer Science & Business Media, 2007.

[21] M. Pelgrom, *Analog-to-digital conversion*. Cham: Springer International Publishing, 2017.

[22] T. Instruments, "Choose the right a/d converter for your application." [Online]. Available: https://www.ti.com/europe/downloads/Choose%20the%20right%20data%20converter%20for%20your%20application.pdf

[23] D. Wenn, "Implementing digital lock-in amplifiers using the dspic® dsc," *Application Note*, 2007.

[24] C. Qi, Y. Huang, W. Zhang, D. Zhou, Y. Wang, and M. Zhu, "Design of dual-phase lock-in amplifier used for weak signal detection," in *IECON 2016 - 42nd Annual Conference of the IEEE Industrial Electronics Society*, Oct 2016, pp. 883–888.

[25] I. Won, D. A. Keiswetter, G. R. Fields, and L. C. Sutton, "Gem-2: A new multifrequency electromagnetic sensor," *Journal of Environmental and Engineering Geophysics*, vol. 1, no. 2, pp. 129–137, 1996.

[26] A. Das and T. Yaswanth, "A low-cost, portable alternative for a digital lock-in amplifier using tms320c5535 dsp," in *2015 Annual IEEE India Conference (INDICON)*, Dec 2015, pp. 1–4.

[27] A. S. Sedra and K. C. Smith, *Microelectronic Circuits*, 7th ed. Oxford University Press, 2015.

[28] T. H. Lee, *The design of CMOS Radio-Frequency Integrated Circuits*, 2nd ed. Cambridge university press, 2003.

[29] B. Razavi, *RF Microelectronics*, 2nd ed. Prentice Hall New Jersey, 2011.

[30] T. Johansson and J. Fritzin, "A review of watt-level cmos rf power amplifiers," *IEEE Transactions on Microwave Theory and Techniques*, vol. 62, no. 1, pp. 111–124, 2014.

[31] X. Jiang, "Fundamentals of audio class d amplifier design: A review of schemes and architectures," *IEEE Solid-State Circuits Magazine*, vol. 9, no. 3, pp. 14–25, 2017.

[32] H. S. Ruiz and R. B. Pérez, *Linear CMOS RF power amplifiers*. Springer, 2013.

[33] M. L. Meade, *Lock-in amplifiers: principles and applications*. Mike Meade, 1983, no. 1.

[34] "About lock-in amplifiers," *Stanford Research Systems, Scientific and Engineering Instruments*, vol. 1993, p. 129, 1992.

[35] Plugable usb audio adapter. Plugable. [Online]. Available: https://plugable.com/products/usb-audio

[36] Sc016 sweex 7.1 external usb sound card. Sweex. [Online]. Available: http://attachments.content4us.com/datasheets/MANUAL_SC016_ENG.PDF

[37] J. Proakis, *Digital signal processing*. Upper Saddle River, N.J: Pearson Prentice Hall, 2007.

[38] V. Ingle, *Digital signal processing using MATLAB*. Stamford, Conn: Cengage Learning, 2012.

[39] Epoch batch conversion tool. EpochConverter. [Online]. Available: https://www.epochconverter.com/batch

[40] Opax22x high precision, low noise operational amplifiers datasheet (rev. b). Texas Instruments. [Online]. Available: http://www.ti.com/lit/ds/symlink/opa228.pdf

[41] Opa827 low-noise, high-precision, jfet-input operational amplifier datasheet (rev. i). Texas Instruments. [Online]. Available: http://www.ti.com/product/OPA827/datasheet

[42] Opax209 2.2-nv/âĹŽhz, low-power, 36-v operational amplifier datasheet. Texas Instruments. [Online]. Available: http://www.ti.com/product/opa209/datasheet

[43] Low-noise, high-speed,16-bit accurate, cmos operational amplifier datasheet (rev. d). Texas Instruments. [Online]. Available: http://www.ti.com/lit/ds/symlink/opa2300.pdf

[44] U. Tietze, *Electronic circuits : handbook for design and application*, 2nd ed. New York: Springer-Verlag Berlin Heidelberg, 2008.

[45] Max98400a evaluation kit datasheet. Maxim Integrated. [Online]. Available: https://datasheets.maximintegrated.com/en/ds/MAX98400AEVKIT.pdf

[46] Max98400a/max98400b datasheet. Maxim Integrated. [Online]. Available: https://datasheets.maximintegrated.com/en/ds/MAX98400A-MAX98400B.pdf

[47] Adafruit ultimate gps. Adafruit. [Online]. Available: https://cdn-learn.adafruit.com/downloads/pdf/adafruit-ultimate-gps.pdf

[48] Gpsd - a gps service daemon. GPSd. [Online]. Available: http://catb.org/gpsd/

[49] Gps visualizer: Do-it-yourself mapping. GPS Visualizer. [Online]. Available: http://www.gpsvisualizer.com/

Glossary

List of Acronyms

A/D	analog-to-digital
AEM	Airborne Electromagnetic
D/A	digital-to-analog
EM	Electromagnetic
emf	Electromotive force
ENOB	Effective number of bits
EMI	Electromagnetic interference
FDEM	Frequency Domain Electromagnetic
GM	Gain Margin
GBWP	Gain-Bandwidth Product
GPS	Global Positioning System
LIA	Lock-in Amplifier
LPF	Low-pass filter
LNA	Low-noise amplifier
NTP	Network Time Protocol
OSR	Oversampling Ratio
PA	Power Amplifier
PPS	Pulse-per-second
PSD	Phase Sensitive Detector

PWM Pulse Width Modulator

RPi Raspberry Pi

SAR Successive approximation register

SBC Single-board Computer

SNDR Signal-to-Noise-and-Distortion-Ratio

TDEM Time Domain Electromagnetic

UAV Unmanned Aerial Vehicle